ON THE USE OF SOLITARY WAVES FOR ENERGY HARVESTING

by

Kaiyuan Li

B.S., Electrical Engineering, Nanjing University, China, 2010

Submitted to the Graduate Faculty of

the Swanson School of Engineering in partial fulfillment

of the requirements for the degree of

Doctor of Philosophy

University of Pittsburgh

2016

UNIVERSITY OF PITTSBURGH

SWANSON SCHOOL OF ENGINEERING

This dissertation was presented

by

Kaiyuan Li

It was defended on

March 7, 2016

and approved by

Piervincenzo Rizzo, Ph.D., Associate Professor,

Department of Civil and Environmental Engineering, University of Pittsburgh

Melissa M. Bilec, Ph.D., Associate Professor,

Department of Civil and Environmental Engineering, University of Pittsburgh

Julie M. Vandenbossche, Ph.D., Associate Professor,

Department of Civil and Environmental Engineering, University of Pittsburgh

Jeffrey S. Vipperman, Ph.D., Professor,

Department of Mechanical Engineering and Material Science, University of Pittsburgh

Dissertation Director: Piervincenzo Rizzo, Ph.D., Associate Professor,

Department of Civil and Environmental Engineering, University of Pittsburgh

ii

ON THE USE OF SOLITARY WAVES FOR ENERGY HARVESTING

Kaiyuan Li, PhD

University of Pittsburgh, 2016

In the last decade there has been an increasing attention on the use of highly- and weakly-nonlinear solitary waves in engineering and physics, such as shock mitigation, acoustic imaging and nondestructive evaluation. These waves can form and travel in nonlinear systems such as one-dimensional chains of particles. One engineering application of solitary waves is the fabrication of acoustic lenses. In this dissertation, an acoustic lens based on the propagation of highly nonlinear solitary waves is proposed. The lens is part of a novel energy harvester able to focus mechanical vibrations into a single point where a piezoelectric element converts the mechanical energy into electricity.

The first step of this research was to investigate numerically and experimentally a novel acoustic lens composed by one-dimensional chains of spherical particles arranged to form a circle array in contact with a linear medium. The second step of the research was to incorporate the acoustic lens into an energy harvesting that includes a wafer-type lead zirconate titanate (PZT) transducer and an object tapping the array. The PZT transducer located at the designed focal point converts the mechanical energy carried by the stress waves into electricity to power a load resistor.

The performance of the designed harvester was compared to a conventional non-optimized cantilever beam, and the results showed that the power generated with the nonlinear lens has the same order of magnitude of the beam. Moreover, the performance of the proposed harvester was compared to a similar system where the chains of particles were replaced by solid rods. The results demonstrated that the granular system generates more electricity. Moreover, some parametric studies were conducted to improve the harvesting performance

of the proposed system. The materials and the geometry of the harvester were considered to enhance the power output of the harvester. Numerical models were built to predict the power output from harvesters designed with different materials and geometries. The design that produces the highest power output was selected as the best design. The best design was tested experimentally to validate the enhancement in energy harvesting capability as predicted in the previous numerical model.

TABLE OF CONTENTS

LIST OF TABLES

LIST OF FIGURES

xiii

xiv

PREFACE

First, I would like to thank Professor P. Rizzo for providing me the opportunity to perform this research. I couldn't finish this dissertation without his guidance and continuous support through the process of my research.

I am thankful to Mr. C. Hager for his help in preparing some of the experiments. The help from Dr. X. Ni and Dr. A. Bagheri in MatLab programming is acknowledged.

I am thankful to my parents, my girlfriend Qian Li and my friends for their encouragement and support.

1.0 INTRODUCTION

1.1 MOTIVATION AND OBJECTIVES

An increasing number of micro-powered electronic devices is used in a wide variety of applications that span from wireless communication node networks [41] and sensors for structural health monitoring [33] to traffic and habitat monitoring [10, 77], and even biomedical implants [33, 77, 13, 25, 65, 75]. All these devices are mainly powered by electrochemical cells (batteries). The need for constant battery replacement can be detrimental as the replacement may be tedious and expensive. Also, environmental problems can arise if the used batteries are not disposed properly or recycled. Thus, the demand for efficient methods to harvest energy from the environment is on the rise.

Human beings have been using windmills and waterwheels ever since the ancient time for energy harvesting. With the development of modern science and technology, more resources are discovered and applied to harvest energy. To date, photovoltaic, piezoelectric, and thermoelectric effects can be used to harvest energy from sunlight, structure vibration, and waste heat, respectively. However, each of these resources has advantages and limitations.

Outdoor solar energy has the capability of providing the largest amount of power density which is about two orders of magnitudes higher than other sources. However, solar energy is not an attractive for indoor environments as the power density drops significantly. Mechanical vibrations are among the most attractive alternatives [5, 31] due to the ubiquitous presence of low and high frequency oscillations across engineering and biological systems [8]. For example, energy can be harvested from the vibration of a bridge [65, 34], vehicle suspensions [83], wind [76], pavement under traffic load [81], human body motion [24, 37] and even from the motions of the heart, lung, and diaphragm [13]. Other sources for ultra-low-

power energy harvesting include electromagnetic energy [55], thermal energy [12], pressure gradients [11], and bio sources [56].

In the last ten years the research and development of vibration-based energy harvesting systems has focused on three elements. The first one is finding a suitable source able to generate the largest amount of vibrations [68, 32]. The second is designing the electromechanical element capable of efficiently converting vibration into electricity [3, 23]. In this case, smart materials have been extensively incorporated in vibrating structures to convert mechanical energy into usable electrical signals [8]. Usually, these materials achieve optimal performance when they operate close to their resonance frequency. However, ambient vibrations often have multiple frequencies or are broadband. Some researchers focused on increasing the harvester working bandwidth [21, 2, 7]. The third way to maximize the amount of energy harvested is by optimizing the interface circuit to extract the energy from the smart material. The simplest circuit typically consists of a full-bridge rectifier and a smoothing capacitor. However, the performance of this classical interface circuit is largely dependent on the load impedance [67, 1].

The research topic of this dissertation falls under the umbrella of vibration-based energy harvesting. In particular, the main objective of the studies presented in this dissertation is the development of a smart element able to convey distributed and global vibration into an electromechanical element that converts the vibration into electricity. The envisioned energy harvesting system is schematized in Fig. 1.1 and it consists of three components: a vibrating structure, an acoustic lens capable of focusing the acoustic vibration, and a wafer-type lead zirconate titantate transducer (PZT) connected to a circuit. The idea is that a structure subjected to mechanical vibrations taps the acoustic lens, which consists of a set of an ordered array of granular particles in contact with a linear homogeneous material. The particles are designed to convert the impact into nonlinear solitary waves, which then coalesce in the homogeneous material into a focal point. The PZT located at the focus converts the mechanical energy into electricity. The uniqueness of the proposed system is that the acoustic lens may serve as a powerless amplifier that conveys distributed (and weak) vibrations into high amplitude pulses.

In this research, the performance of the proposed harvester is compared to a counterpart where the chains of beads are replaced by steel rods. This is done to prove the advantage of using the nonlinear acoustic lens. Furthermore, some parametric studies are conducted numerically and experimentally to enhance the power density of the system.
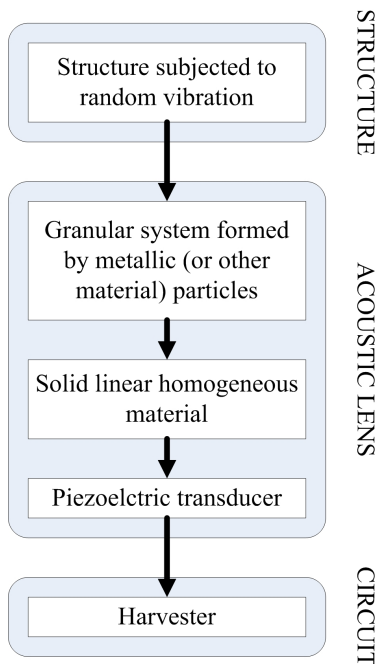
Figure 1.1: Scheme of the energy harvesting system envisioned in this study. Figure from Ref. [42].

1.2 OUTLINE

The outline of the study presented in this dissertation is illustrated in Fig. 1.2, which shows the flow chart of the six steps taken in this research. The outcome of each step was reported in a journal article cited in the square bracket. The ultimate goal of the research was to develop an energy harvester with an acoustic lens made of chains of spherical particles.

A prototype of the harvester was first designed (steps 1-3) and then was improved by a parametric analysis (steps 4-6).

An acoustic lens is a device that is capable of focusing acoustic energy. Figure 1.3 shows a typical acoustic lens [49] where plane waves enter from the left side and focus in
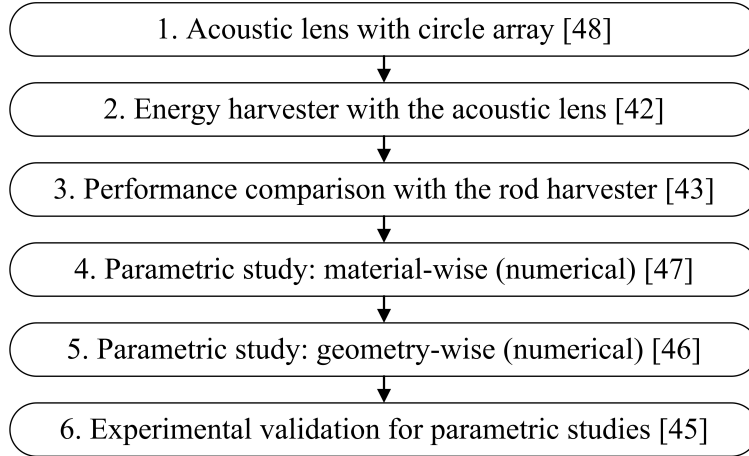
Figure 1.2: Flow chart of the research on the use of solitary waves for energy harvesting.
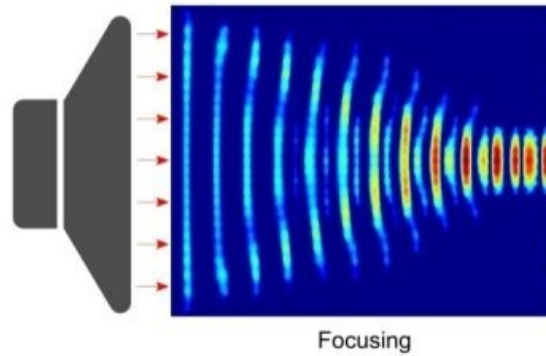
Figure 1.3: An example of acoustic lens in the literature [49].

the blue area which indicates a novel acoustic beam aperture modifier using butt-jointed gradient-index phononic crystals (GRIN PCs) consisting of steel cylinders embedded in a homogeneous epoxy background. In literature [74], the prototype of an acoustic lens with a line array of chains of spherical particles was proposed. However, the focusing effect of this line array based lens requires tuning the precompression in the chains which is a complicated procedure.

In step 1, the acoustic lens was improved by replacing the line array with a circle array to avoid tuning the precompression, and its focusing effect was verified in both solid and fluid media using numerical simulation and experiments. The work in this step is presented in Chapter 3 and has been published in the *ASME Journal of Applied Mechanics* [48].

In step 2, a novel energy harvester was built by attaching a piezoelectric element to the focal point of the acoustic lens where the mechanical energy was concentrated. Experiments were conducted to evaluate the electrical power ouput from the energy harvester and the results were compared with a traditional cantilever beam harvester where the same type of piezoelectric element was deployed and the same mechanical force input was applied. The work in this step is presented in Chapter 4 and has been published in the *ASME Journal of Vibration and Acoustics* [42].

In step 3, the functionality of the chains of particles was tested by replacing the chains with steel rods. With the first three steps, a novel energy harvester with acoustic lens functionality was prototyped, tested and compared with traditional methods. The work in this step is presented in Chapter 5 and has been published in the *Journal of Applied Physics* [43].

In step 4, a material-wise parametric study was done by selecting different materials to compose the acoustic lens. The selected materials span a wide range in their properties and the harvester performance was tested with numerical simulations. The work in this step is presented in Chapter 6 and has been published in the *Smart Materials and Structures* [47].

The best material configuration was picked up and another parametric study from geometry perspective was done in step 5. Different dimensions were selected for the acoustic lens components. Numerical simulations were done for different cases to find out the best geometry configuration. The work in this step is presented in Chapter 6 and has been submitted to the *ASME Journal of Vibration and Acoustics* [46].

In step 6, a series of experiments were conducted to verify the conclusions made in steps 4 and 5, which were based on numerical results. In particular, it was validated that the power ouput of the energy harvester can be enhanced by fixing the bottom side of the piezoelectric element, reducing the circle array size of the acoustic lens and changing the material of the linear medium block of the acoustic lens from polycarbonate into steel. The work in this step is presented in Chapter 7 and has been submitted to the *Journal of Intelligent Material Systems and Structures* [45].

Finally, Chapter 8 ends the dissertation with some conclusive remarks and suggestions for future works. It is acknowledged here that the works presented in this dissertation have been either published as journal articles or submitted to journals for review.

2.0 BACKGROUND

This chapter presents the background on the topics discussed in this dissertation. In particular, Section 2.1 describes the highly nonlinear solitary waves. Section 2.2 describes the numerical model to predict the propagation of the solitary waves along the chain of particles. Section 2.3 presents the interface circuit integrated into the energy harvester used to evaluate the power generation capability, as well as the validation of the underlying assumption that the PZT utilized in this study can be approximated as a pure capacitor. Section 2.4 presents the analysis of power output a function of vibration frequency. This section also explains the reason why different load resistors in the interface circuit generates different power output. This section guides the readers with numerical and experimental power output curves shown in later sections.

2.1 HIGHLY NONLINEAR SOLITARY WAVES AND ACOUSTIC LENS

HNSWs are mechanical waves that can form and travel in highly nonlinear media such as a compact chain of spherical particles. In 1983, Nesterenko studied the wave propagation in a chain of identical spheres analytically and numerically [57]. The Hertz contact law [26] was utilized to model the sphere-sphere interaction. Following Kunin's analytical methods [36], Nesterenko obtained the analytical expressions for wave propagation in a chain with different levels of precompression. In particular, Nesterenko discovered that when the precompression is negligible, the wave has the shape of a single hump, *i.e.* a soliton. Nesterenko called this wave the highly nonlinear solitary wave. The nonlinearity arises from the power law relationship, *i.e.* the Hertz law, between the contact force and the approach between two

spheres. When two generic spheres are in contact (Fig. 2.1) or a sphere is in contact with a flat surface, the contact force F is described by the Hertz law [26]:

$$F = A\delta^{3/2} \tag{2.1}$$
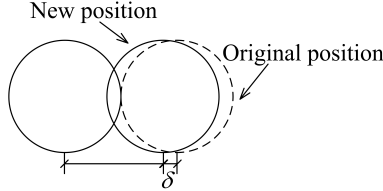
Figure 2.1: Definition of approach in sphere-sphere contact.

where A is the stiffness constant that is dependent on the geometry and the mechanical properties of the materials in contact, and δ is the approach of the centers of the two particles as indicated in Fig. 2.1. For different contact scenarios, the stiffness constant can be represented as A_c for contact between two identical spheres and A_w for a sphere-wall contact:

$$A = \begin{cases} A_c = \frac{E\sqrt{2r}}{3(1-\nu^2)} \\ A_w = \frac{4\sqrt{r}}{3}\left(\frac{1-\nu^2}{E} + \frac{1-\nu_w^2}{E_w}\right)^{-1} \end{cases} \tag{2.2}$$

In Eq. 2.2 r is the radius of the sphere, E and ν are the Young's modulus and the Poisson's ratio of the sphere material, respectively. The subscript $'w'$ indicates the parameters associated with the wall material.

The HNSW was then observed in the experiment of Lazaridi *et al.* [39] and its unique properties were studied extensively by many researchers [6, 14, 15, 20, 28, 29, 53, 54, 60, 61, 62, 63, 64, 71, 74, 79, 80]. Falcon *et al.*. [20] studied the fragmentation of a chain of particles when impacting a fixed wall. Sen *et al.* [71] studied numerically the backscattering of the solitonlike pulse with the presence of a light mass impurity in the chain. Manciu *et al.* [54] investigated the crossing of identical solitary waves in a chain of elastic beads. Manciu *et al.* [53] investigated the wave reflections from rigid wall boundaries. Job *et al.* [28] evaluated the collision of a single solitary wave with elastic walls with various stiffness. Daraio *et al.* [14] demonstrated experimentally that chains of composite particles with a hard core and a soft

interacting layer support the Hertzian type of interaction and the formation of the HNSW. Daraio *et al.* [15] validated experimentally the effect of precompression upon the wave speed of the HNSW. Spadoni *et al.* [74] utilized the tunability of the HNSW speed to achieve wave focusing and generated a sound bullet. Yang *et al.* [79] investigated the interaction of the HNSW with linear elastic media and found the relationship between the stiffness of the linear media and the secondary solitary wave. Ni *et al.* [63] devised a compact HNSW actuator with an electromagnet lifting and dropping the striker sphere. This novel actuator was applied to monitor the hydration process of cement paste [64]. Cai *et al.* [6] observed the interaction of HNSWs with slender beams.

2.2 DISCRETE PARTICLE MODEL

In this study, a discrete particle model (DPM) [79, 6, 59] is used as a numerical method to predict the propagation of the HNSW in a chain of spherical particles. The DPM is deployed in this research when a numerical model is utilized to predict or evaluate the performance of an acoustic lens or an energy harvester. Specifically, the DPM calculates the interaction force between the chain of particles and the linear medium block. The equation of motion for each particle in a vertically aligned chain of N particles can be derived with the Newton's second law:

$$
\begin{aligned}
m\ddot{u}_0 &= -A_c(\delta_2 - u_2 + u_1)^{3/2} + mg \\
m\ddot{u}_i &= A_c(\delta_i - u_i + u_{i-1})^{3/2} - A_c(\delta_{i+1} - u_{i+1} + u_i)^{3/2} + mg \\
m\ddot{u}_N &= A_c(\delta_N - u_N + u_{N-1})^{3/2} - A_w(\delta_{N+1} - u_{N+1} + u_N)^{3/2} + mg
\end{aligned}
\tag{2.3}
$$

where m is the mass for the particle, u_i is the displacement for the ith particle. In this model, we assume that the solitary wave is invoked by the impact of a striker, which is a particle identical to the particles in the chain. Specifically: u_0 is the displacement of the striker; u_N is the displacement of the last particle; $u_{N+1} = 0$ is the displacement of the fixed ending wall; δ_i is the approach between two adjacent particles introduced by gravitational

precompression; mg is the gravity force. This means that without gravity, the two particles have no deformation and their center to center distance is L, shown in Fig. 2.2a. When the gravity force is introduced, the two particles are deformed and their center to center distance is changed to L', shown in Fig. 2.2b, the gravity introduced approach is defined as the difference between original and deformed center to center distances, *i.e.* $\delta_i = L - L'$.

(a) Original positions without gravity   (b) New position with gravity
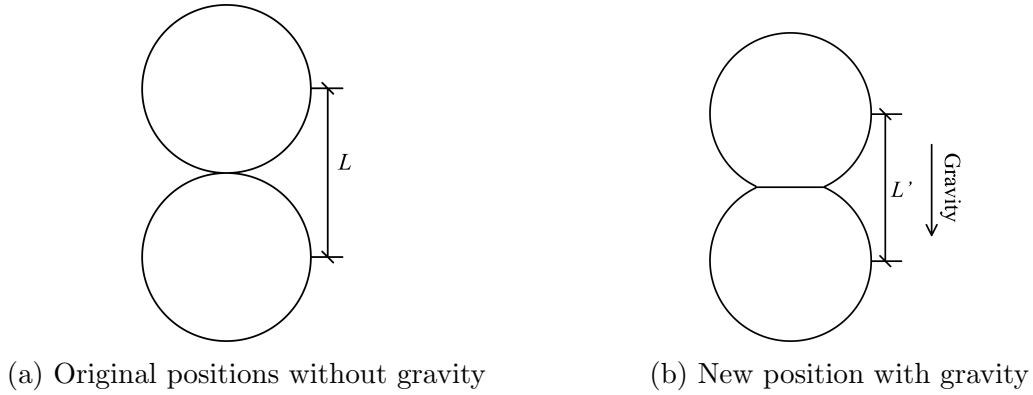
Figure 2.2: Approach introduced by gravity.

The effect of a striker is modeled as a particle in contact with the chain and having the initial velocity v_0. It is known that a condition for the observation of a single solitary wave is that the duration of the striker collision is shorter or equal to the duration of the transmitted wave, which is approximately twice the ratio $(r\sqrt{10})/V_S$ [29]. Here V_S is the speed of the solitary pulse. The MATLAB differential equation solver *ode45()* [59] was utilized to solve Eq. 2.3 and to determine the dynamic contact force at the interface between the chains and the ending wall.

Figure 2.3 presents a graphical user interface coded with the Matlab graphical user interface design environment (GUIDE) to demonstrate and predict the propagation of a solitary pulse in a user-defined chain of spherical particles. The interface demonstrates the result from the DPM in an intuitive way. The bottom left panel customizes the parameters of the chain such as the number of beads, the material and geometric properties of the spheres, the velocity of the striker, *etc.* It is noted that the chain ends with a fixed wall. The bottom center panel presents the colormap of the wave propagation. The colormap shows the normalized force inside the beads as a function of time. As shown in this panel, the solitary wave travels along the chain and reflects at the ending wall. It is interesting
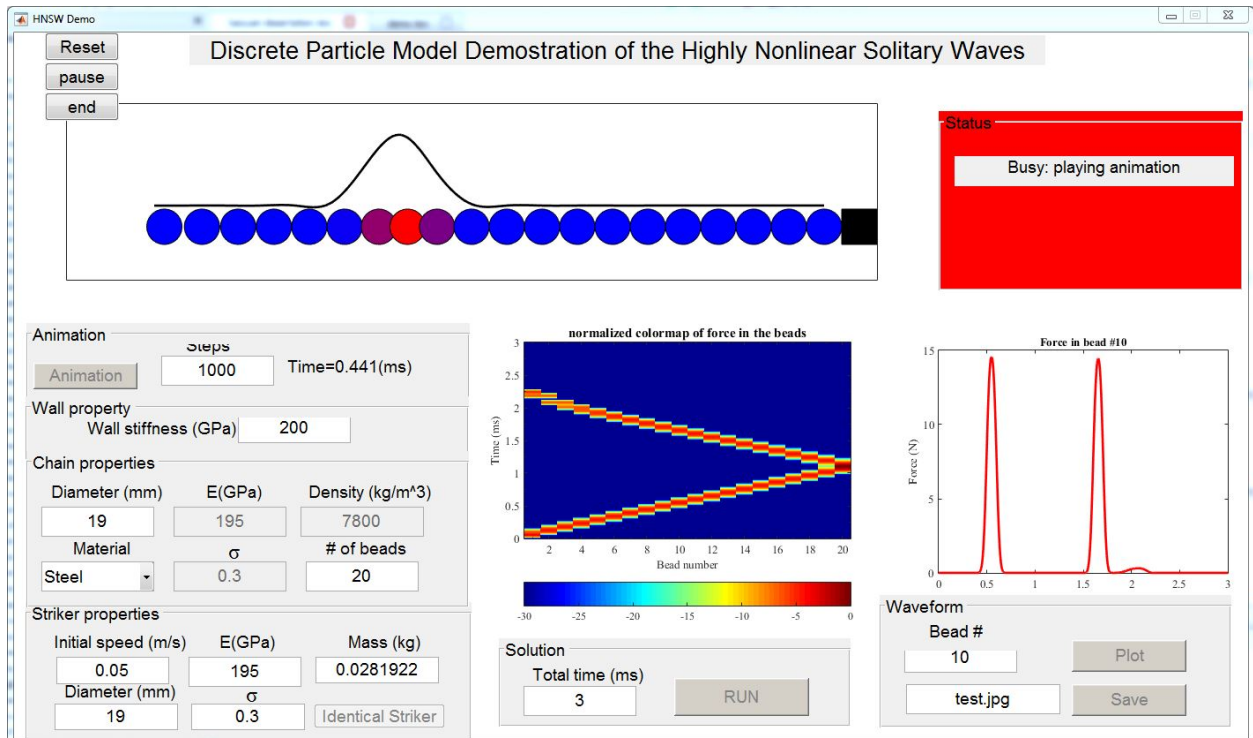
Figure 2.3: Graphical user interface by Matlab GUIDE to demonstrate the propagation of HNSW in a customized chain of beads.

to note that the shape of the solitary wave maintains the same all through the propagation and reflection process. The bottom right panel shows the force profile inside a specific bead. An animation of the HNSW propagation along the chain is demonstrated in the top left panel, where the displacement of each bead is amplified and force inside each bead can be inferred from the bead color. It is noted here that the overlapping of two beads is the effect of amplified bead displacement. The animation also demonstrates that the wave length is always equal to five particle diameters [58].

2.3 INTERFACE CIRCUIT FOR THE ENERGY HARVESTER

As is said in Chapter 1, the objective of this Ph.D. research is to fabricate an energy harvester which transfers mechanical vibration into electricity effectively. The performance of the proposed harvester is quantified by computing the electrical power output from the PZT. To

measure the amount of power that can be harvested using a PZT, an interface circuit such as the one schematized in Fig. 2.4 [23, 18, 51, 78, 1] is typically implemented by connecting an output load resistor R to the PZT. Here $v(t)$ is the instantaneous voltage generated by the transducer in the time domain, $v_o(t)$ is the output voltage across the resistor R, and Z_{PZT} is the electrical impedance of the PZT given by $Z_{PZT}(\omega) = R_{PZT}(\omega) + iX_{PZT}(\omega)$, where $R_{PZT}(\omega)$ and $X_{PZT}(\omega)$ are the resistance and reactance, respectively, and ω is the angular frequency.
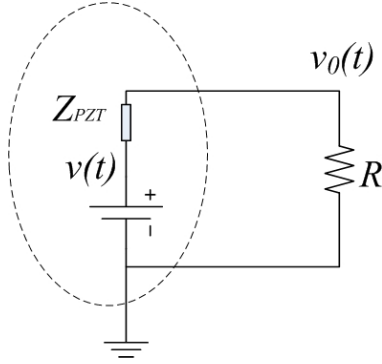
Figure 2.4: Interface circuit of the energy harvester. Figure from Ref. [42].

According to the Parseval's theorem [73], the energy absorbed by the load resistor is

$$E = \int_{-\infty}^{\infty} \frac{|v_o^2(t)|}{R} dt = \frac{1}{2\pi} \int_{-\infty}^{\infty} \frac{|V_o^2(\omega)|}{R} d\omega \tag{2.4}$$

where $V_o(\omega)$ is the voltage across the resistor in the frequency domain and it is given by

$$V_0(\omega) = V(\omega) \cdot \frac{R}{R + Z_{PZT}} = V(\omega) \frac{R}{R + R_{PZT}(\omega) + iX_{PZT}(\omega)} \tag{2.5}$$

By replacing Eq. 2.5 into Eq. 2.4, the energy E can be written as a function of R, i.e.,

$$E(R) = \frac{1}{2\pi} \int_{-\infty}^{\infty} \frac{|V_o^2(\omega)| \, R}{|R + R_{PZT}(\omega) + iX_{PZT}(\omega)|^2} d\omega \tag{2.6}$$

If a time window of length T is considered, the average power output over this time interval is

$$P(R) = \frac{E(R)}{T} \tag{2.7}$$

In order to maximize the amount of energy that can be harvested, the load resistance R that maximizes Eq. 2.7 must be found. At a given frequency ω_0, the maximum power value can be found when [82]

$$\frac{dP(R)}{dR} = \frac{1}{T}\frac{dE(R)}{dR} = \frac{1}{2\pi T}\int_{-\infty}^{\infty}\left|V^2(\omega)\right|d\omega \times \frac{d}{dR}\left(\frac{R}{|R + R_{PZT}(\omega) + iX_{PZT}(\omega)|^2}\right) = 0 \tag{2.8}$$

After a few algebraic manipulations [35], Eq. 2.8 is satisfied when:

$$R = \sqrt{R_{PZT}^2(\omega_0) + X_{PZT}^2(\omega_0)} = R_{opt} \tag{2.9}$$

That provides the value of the optimal resistor at a certain frequency ω_0. Equation 2.9 suggests that the optimal power output is attained when the value of the load resistor is identical to the electrical impedance of the PZT. Thus, it is necessary to know the characteristics of the transducer impedance with respect to the frequency to maximize the power output, *i.e.* Eq. 2.8 necessitates an impedance matching condition between the driven load and the transducer.

It is noteworthy that any PZT behaves approximately as a pure capacitor at low frequencies far from resonance [68, 72]. In this case the electrical impedance of the PZT used in this study can be approximated as [67, 40]:

$$Z(\omega) = \frac{1}{i\omega C_{PZT}} \tag{2.10}$$

Here, $C_{PZT} = \epsilon_{33}^T bl/t$ is the capacitance of the free PZT, b, l, t are the breath, length, and thickness of the PZT, respectively, and ϵ_{33}^T is the dielectric constant at zero stress in the thickness direction. The properties of the PZT(PSI-5A4E) utilized in all the following studies are listed in Table 2.1.

In order to validate the estimation of Eq. 2.10 in this study, a finite element model with coupled physics full harmonic analysis was built using ANSYS13.0. A 20-node high order brick element SOLID226 was utilized. Each node had four degrees of freedom, the displacement in three spatial coordinates and the voltage potential. One electrode was modeled by coupling the voltage degree of freedom of the top nodes; the same method was

Table 2.1: PZT (PSI-5A4E) parameters. Table from Ref. [42].

Property(unit)	Symbol	Value
Size($mm \times mm \times mm$)	$b \times l \times t$	$10 \times 10 \times 2$
Density(kg/m^3)	ρ	7.8×10^3
Compliance($\times 10^{-12} m^2/N$)	s_{11}^E, s_{22}^E	15.2
	s_{33}^E	19.2
	s_{12}^E	-4.8
	s_{13}^E, s_{23}^E	-5.7
	s_{44}^E, s_{55}^E	47.8
	s_{66}^E	39.9
Piezoelectric coupling($\times 10^{-10} m/V$)	d_{31}, d_{32}	-1.9
	d_{33}	3.9
	d_{15}	5.9
Dielectric permittivity(nF/m)	ϵ_{11}^T, ϵ_{22}^T	15.5
	ϵ_{33}^T	16.3

applied to the bottom nodes to model the bottom electrode. In the harmonic analysis, the bottom electrode was constrained to $v(t) = 0$, where v is the voltage potential, while unit sinusoidal voltage displacement loads with different frequencies were applied to the top electrode. The reaction force of output charge Q on the top electrode was extracted and the electrical impedance Z was then calculated by voltage load over the current I:

$$Z = \frac{V}{I} = \frac{1}{i\omega Q} \tag{2.11}$$

Figure 2.5 shows the impedance as a function of the excitation frequency. The first resonance frequency is located at around $170kHz$. This suggests that Eq. 2.10 can be used; in fact, we will show later that the PZT operates below $20kHz$ which is much lower than the PZT's first resonance. A close up view of Fig. 2.5a is presented in Fig. 2.5b where the analytical results obtained from Eq. 2.10 are overlapped to the finite element model and the results match perfectly, confirming that the approximation of Eq. 2.10 is valid in this study.

2.4 POWER OUTPUT CALCULATION

In order to find the load resistor R_{opt} that maximizes the power output, Eq. 2.10 is replaced into Eq. 2.9, and the optimal load resistor R_{opt} can be expressed by the following relationships:

$$R_{opt} = |Z_{PZT}| = \left| \frac{1}{j\omega C_{PZT}} \right| = \frac{bl\epsilon_{33}^T}{\omega t} \tag{2.12}$$

From Eq. 2.12 we can calculate the maximum power output at a certain frequency. For instance, consider that the PZT is subject to a harmonic vibration with the open circuit voltage $v_o(t) = v_a sin(\omega t + \varphi)$, where v_a is the amplitude and φ is the phase. The maximum power output P_{max} on the load resistor can be written as:

$$P_{max} = \left| \frac{v_a^2}{2(R_{opt} + Z_{PZT})^2} R_{opt} \right| = \frac{v_a^2 \omega C_{PZT}}{4} \tag{2.13}$$

Equation 2.13 indicates that the power is proportional to the vibration frequency, provided the open circuit voltage amplitude is the same. At PZT resonance, Z_{PZT} is close to 0, and the optimal load $R_{opt} = |Z_{PZT}|$ is also close to zero. Notice for the P_{max} expression that the denominator is of second order and the numerator is of first order. When both the

(a) $0 - 300kHz$ (b) $0 - 20kHz$
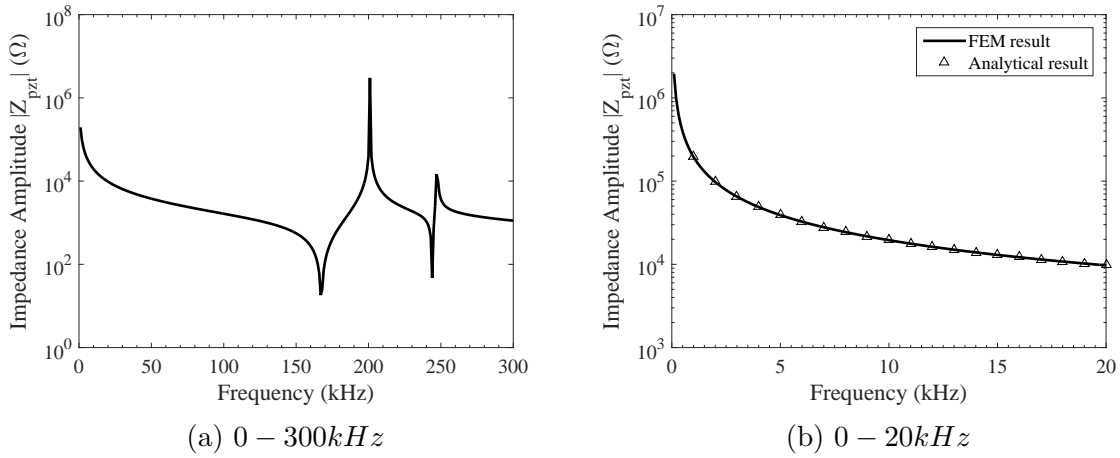
Figure 2.5: FEM of the PZT(PSI-5A4E). Impedance as a function of the excitation frequency. In (b) the results are overlapped to the analytical results obtained using Eq. 2.10. Figure from Ref. [42].

denominator and numerator are approaching 0, P_{max} will be extremely large. Therefore, the power output would be maximized when the frequency of the stress waves approaches or match the resonant frequency of the transducer.

The power output of the PZT across a pure resistor R in the time interval $[0, T]$ can be evaluated either in the time domain, or in the frequency domain, according to the Parseval's theorem [73]:

$$P(R) = \frac{1}{T} \int_0^T \frac{v_0^2(t)}{R} dt = \frac{1}{2\pi T} \int_{-\infty}^{\infty} \frac{V_0^2(\omega)}{R} d\omega = \frac{1}{2\pi T} \int_{-\infty}^{\infty} \frac{V_{open}^2(\omega)}{|R + Z_{PZT}|} R d\omega \qquad (2.14)$$

In Eq. 2.14, $v_0(t)$ and $V_0(\omega)$ are the voltage across the resistor in the time and frequency domain, respectively, $V_{open}(\omega)$ is the open circuit voltage in the frequency domain, R is the value of the resistor and Z_{PZT} is the impedance of the transducer given by Eq. 2.12.

3.0   ACOUSTIC LENS DESIGN

3.1   INTRODUCTION

The work presented in this chapter is based upon Spadoni and Daraio's pioneering work [74] in acoustic energy focusing using HNSWs. In Ref. [74], a mechanical system was designed for the generation of compact acoustic pulses, called sound bullets, in solids and fluids. The scheme of this mechanical system is shown in Fig. 3.1, where n chains are located on top of a linear medium block and the chains are vertically aligned in paralel. The individual chains in the array were precompressed differentially such that an acoustic signal with fixed phase incident on the top of the chains results in transmitted waves with phase delays. The precompression and phase delays were chosen so that the individual waves transmitted by each chain coalesce at a focal point in the adjacent host medium. Theory, numerical simulations, and experiments demonstrated the focusing effect and therefore this mechanical system was named the *acoustic lens*.

To achieve focusing, Spadoni and Daraio [74] applied a different static precompression on each chain of particles that composes the lens. To calculate the necessary time delay distribution for the signals emanating from the individual chains, the chains of spheres were assumed to transmit mechanical disturbances to the host medium as radiative point sources. This is possible due to the small contact area between a sphere and an adjacent planar surface. Such point sources produce spherical acoustic waves in the host medium, which is linear and isotropic.

17
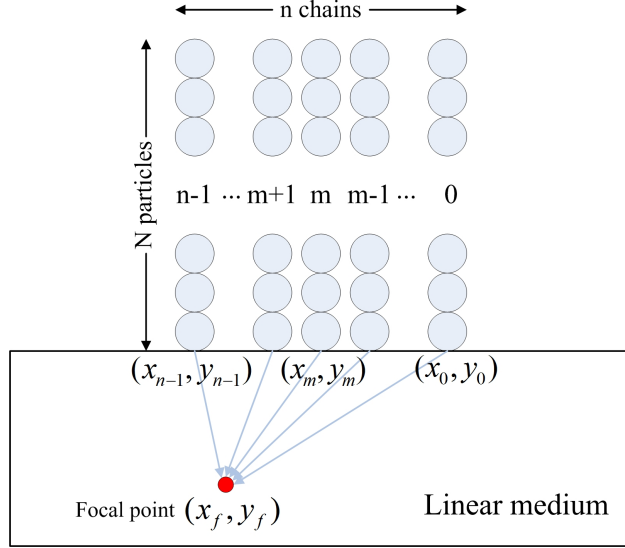
Figure 3.1: Schematics of the wave field generated in a linear medium by a line array made of n chains made of spherical particles.

Geometric or ray acoustics can thus be utilized to estimate the delay between chain 0 and chain i, *i.e.* Δt_i distribution necessary to focus energy at a desired location (x_f, y_f). The delays satisfy:

$$c^2(t_0 - \Delta t_i)^2 = (x_f - x_i)^2 + (y_f - y_i)^2 \tag{3.1}$$

where (x_i, y_i) is the location of the ith source, c is the speed of sound in the linear medium, and t_0 is the travel time between the farthest source and the focal point. Since the HNSWs in all the chains are initiated simultaneously with striker beads of the same speed. The time delay Δt_i can be converted to a precompression distribution on the chains of particles based on the dependence of the solitary wave velocity V_S on the ratio $F_r = F_m/F_0$ of the maximum dynamic force F_m to the static force F_0,

$$V_S = \frac{c_0}{F_r - 1} \left\{ \frac{1}{15} \left[3 + 2F_r^{5/3} - 5F_r^{2/3} \right] \right\}^{1/2} \tag{3.2}$$

Here, c_0 is the characteristic speed of sound in each chain of particles [58].

The advantage of this lens is that the position, amplitude, and frequency content of the focused acoustic wave in the linear medium are dynamically controllable. Moreover, when compared to the focusing of acoustic waves by means of electromechanical transducers, the

18

use of HNSWs allows for the generation of compact, nonoscillatory, and high-amplitude signals. However, this lens requires the various precompressions on different chains, which can be a complicated process.

In this chapter, we propose the design of a nonlinear acoustic lens made of elastic spheres arranged into a circle array. The circle array overcomes some of the shortcomings associated with the line arrays proposed by Spadoni and Daraio [74]. To carry out a comprehensive study that can ascertain the advantages and limitations of the line array proposed in Ref. [74] and the circle array proposed here, a numerical study was conducted. The DPM presented in Chapter 2.2 was used to derive the shape and amplitude of the force function at the chains-host medium interface. Then, a commercial finite element software was used to model the propagation of the acoustic fields in the host medium to predict the location and amplitude of the focused sound. A total of two arrays and two host media, namely polycarbonate and water, were simulated. Moreover, the numerical results relative to the circle array were validated experimentally.

The chapter is organized as follows. Section 3.2 describes the principles and the design of the arrays. Section 3.3 describes the results associated with a finite element simulation adopted to compare the acoustic focusing attained by the line array and the circle array. Section 3.4 illustrates the setup and the results of an experiment, whereas section 3.5 ends the chapter with some concluding remarks.

The work reported in this chapter is published in the *ASME Journal of Applied Mechanics* [48] and most of this chapter is excerpted from that paper.

3.2 CIRCLE ARRAY DESIGN

The line array requires tuning the precompression of the chains of particles. Therefore, its practical implementation might be cumbersome. To circumvent this problem we propose a lens where the n chains are assembled in a circle (Fig. 3.2) and focusing is attained along the axis (hereafter indicated as the focal axis) passing through the center of the circle and orthogonal to the interface. Here the delay of the waves radiating from the interface is null,

19

i.e. the nonlinear characteristics of the transducers are uniform. The diameter D of the array is strictly dependent upon the center-to-center distance d between two adjacent particles and the number n of the array, *i.e.*:

$$D \cong \frac{n \cdot d}{\pi} \tag{3.3}$$

Owing to the geometric attenuation of the bulk waves in the linear medium, the amplitude of the sound at the focal axis is a function of the Euclidean distance between the radiating point and the position along the focal axis and of the constructive interference (superposition) of the linear waves propagating at the speed of sound in the host medium.
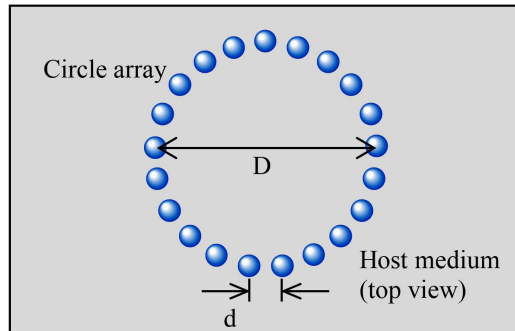
Figure 3.2: Schematics of a circle array made of 21 chains of $9.5mm$ diameter particles. In order to carry a direct comparison between this array and the line arrays described earlier, $D = 64.5mm$ and $d = 9.65mm$. Drawing not to scale. Figure from Ref. [48].

3.3 NUMERICAL STUDY

3.3.1 Numerical setup

To portray, quantify, and compare the focusing effect between the line and the circle arrays, we coupled the discrete particle model used to predict the time of arrival of the solitary wave pulses, to a finite element analysis. The initial speed of the striker was set to $4m/s$, which is the value considered in Ref. [74]. Two host media were considered: polycarbonate and water. The finite element models were built using the commercial software ANSYS v13.0. For polycarbonate, the 3D 8-node SOLID185 element with three degrees of freedom per

node was used. The material's properties of the polycarbonate were density $= 1230 kg/m^3$; Young's modulus $= 3.45 GPa$; Poisson's ratio $= 0.35$. For the water, the 3D 8-node FLUID30 element with pressure as the only degree of freedom was used. The material's properties were: density $= 1000 kg/m^3$; sound speed $= 1460 m/s$. To guarantee the accuracy of the numerical result, the element size was chosen as $2mm$ which is $1/80$ of the impact wavelength, and the implicit integral time step was chosen as $2\mu s$ which is $1/50$ of the impact time duration. A convergence test was conducted by doubling the spatial and the time resolution of the model. Same numerical result was obtained to prove the convergence of the finite element model.

3.3.2 Numerical results

First, our analysis considered a line array (Fig. 3.3a) made of chains subjected to different precompression and in contact with a polycarbonate block, as well as a circle array composed of the same number of chains with no precompression (Fig. 3.3b). It is important to note here that for the line array, the precompression was calculated according to the designed focal point located $100mm$ underneath the center chain. This simulation reproduced the work in [74] and it compares the performance of the line array in the literature and the new circle array via finite element analysis.

Figures 3.4a and 3.4b present the stress distribution inside the polycarbonate block when focusing is achieved. It is interesting to note that in Fig. 3.4a, the energy center is not at the focal point when focusing is achieved. This is due to beam spreading when the wave is propagating in the polycarbonate block, *i.e.* waves have higher energy density when they are closer to the source. To quantify the acoustic energy localized at the vertical middle axis of the polycarbonate, Fig. 3.4c is presented. It shows the values of the maximum Von Mises stress occurred at the axis as a function of the depth. Deeper than $32mm$, the circular arrangement provides larger stress than the line arrangement. At $(x = 0mm; y = 100mm)$ the stress is $464kPa$ and $780kPa$ for the line and the circle array, respectively.

The same analysis was conducted by replacing the polycarbonate with water. In the finite element model the profile of the solitary wave input source at the fluid structure interface
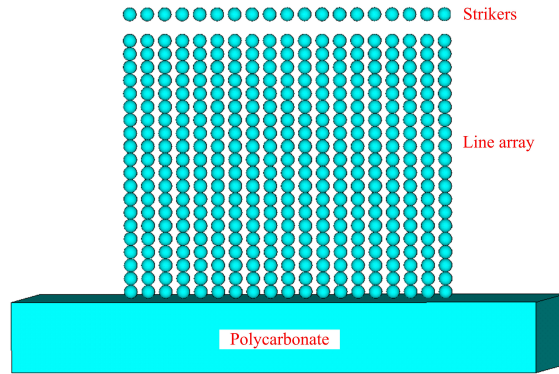
(a) Line array
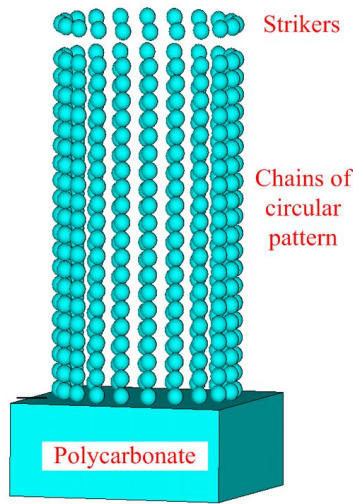
(b) Circle array

Figure 3.3: Schematics of (a) a line array and (b) a circle array. Figure from Ref. [42].

(FSI) represented the pressure. Thus, the wave propagating in water was omnidirectional. Figures 3.5a and 3.5b shows the pressure field in water overlapped with instantaneous pressure amplitude along the symmetry axis at the instants when focusing is achieved for both arrays. To compare the maximum pressure attained at each point of the axis of symmetry by both arrays, Fig. 3.5c is presented to show the pressure as a function of the depth associated with both arrays. A monotonic decrease is observed for both, but overall the circle array provides higher amplitude than the line array. Interestingly, the profile of the maximum pressure associated with the water medium is different than the solid medium (Fig. 3.4c).
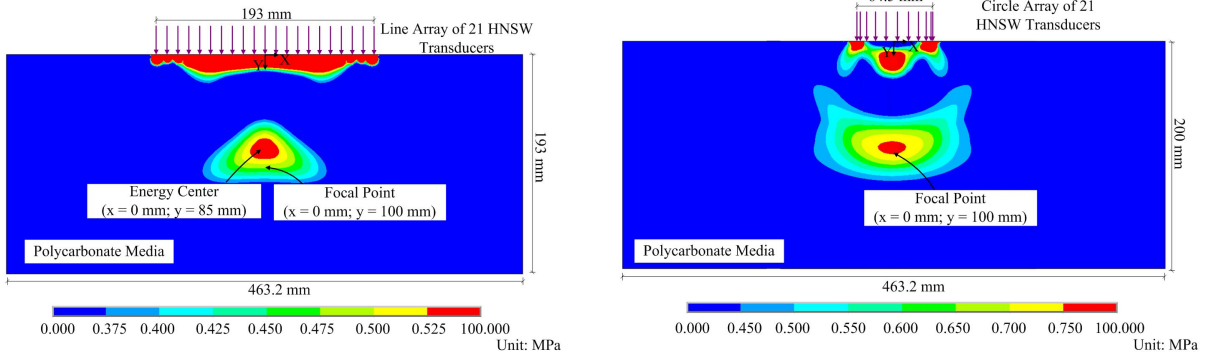
(a) Line array

(b) Circle array
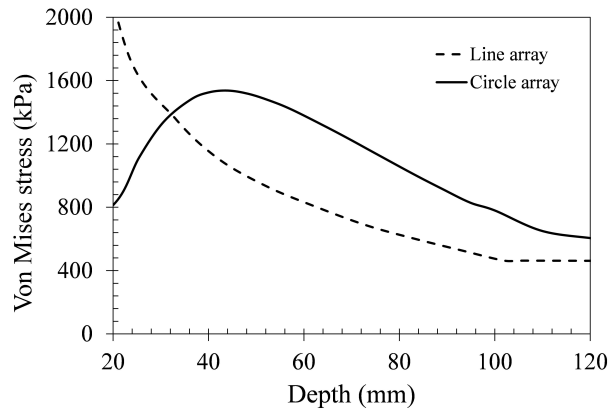
(c) Maximum stress comparison

Figure 3.4: Designs of a line array and a circle array made of 21 chains of particles. Von Mises stress in polycarbonate with (a) line array lens and (b) circle array lens when focusing is achieved. (c) Maximum von Mises stress as a function of the depths in the polycarbonate block. Figure from Ref. [48].

The difference is related to the omnidirectionality of the wave propagation in water and direciontal propagation in the polycarbonate. In the case of polycarbonate with a circle array, stress in the center axis near the top surface of the polycarbonate block is low, since only a small portion of acoustic energy from the source travels in this direction. As a matter of fact, most acoustic energy propagates downward.

23

(a) Line array

(b) Circle array

(c) Maximum pressure comparison
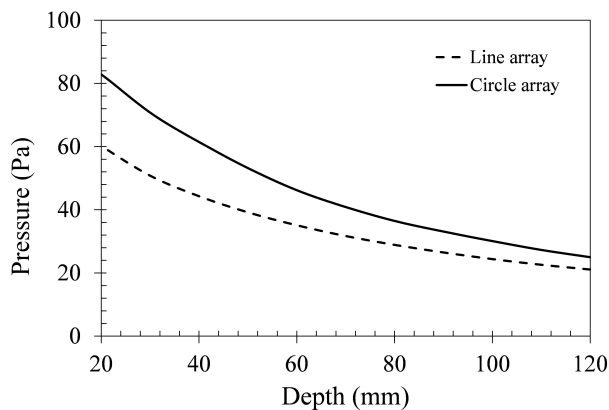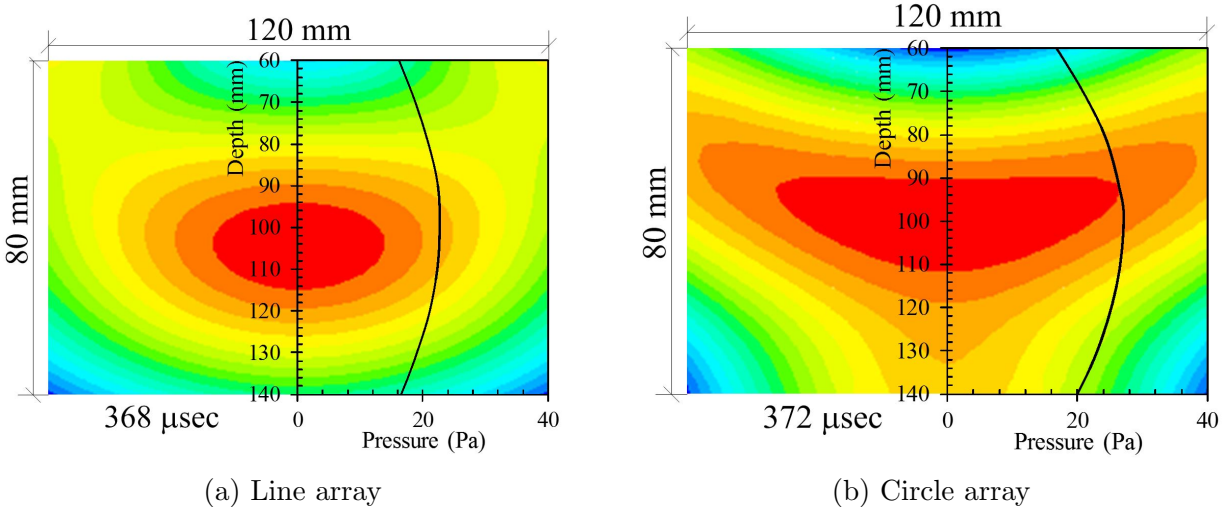
Figure 3.5: Designs of a line array and circle array made of 21 chains of particles. Pressure in water with (a) line array lens and (b) circle array lens when focusing is achieved. (c) Maximum pressure as a function of the depths in water. Figure from Ref. [48].

3.4 EXPERIMENTAL STUDY

3.4.1 Experimental setup

To investigate the feasibility of the circle array an experiment was conducted and its results are presented here. The acoustic lens consisted of an ultra-high-molecular-weight polyethylene (UHMW) block containing 20 through-thickness holes, $9.6mm$ in diameter. The holes were filled with 21 general purpose stainless steel beads, $9.5mm$ ($3/8inches$) in diameter. The chains were distributed along a circle of $101.6mm$ ($4inches$) in diameter. This was a

24

good trade-off between the objective of validating experimentally the numerical setup and the need of machining through-thickness holes without shrinking the adjacent holes. To prevent the free fall of the particles, a 2.5mm thick aluminum sheet was bonded at the bottom of the acoustic lens. An aluminum plate 6.4mm thick was placed on top of the chains. Two photos of the lens are presented in Fig. 3.6.
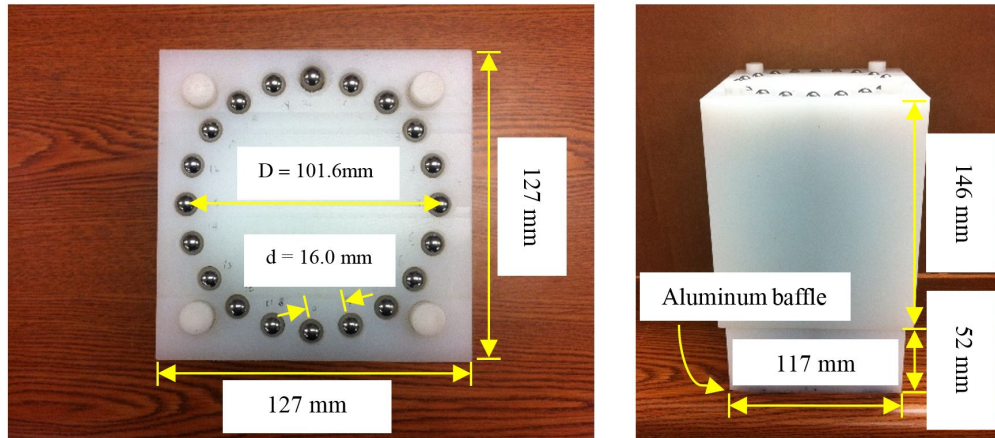
Figure 3.6: Top and elevation view of the experimental lens. Figure from Ref. [48].

The solitary waves on the chains were generated by means of the impact of an iron rod on the plate remotely controlled using an electromagnet. The rod was set such to impact the centroid of the aluminum plate on top of the chains 10 times for each testing point. The host linear medium was water. The acoustic pressure field in water generated by the solitary waves reaching the fluid structure interface (FSI) was measured by means of a commercial hydrophone (RESON TC4013-1). The overall experimental setup is shown in Fig. 3.7. The pressure field was measured along the symmetric axis of the lens (vertical scanning line in Fig. 3.7a), and moving the hydrophone along a line path parallel to the interface 50mm below (horizontal scanning line in Fig. 3.7a). For each scanning point, ten measurements were taken to improve the statistical significance of the experiment.

3.4.2 Experimental results

To estimate the focusing effect and to evaluate how the pressure field is distributed along the two directions measured here, the amplitude of the negative time waveform peak was
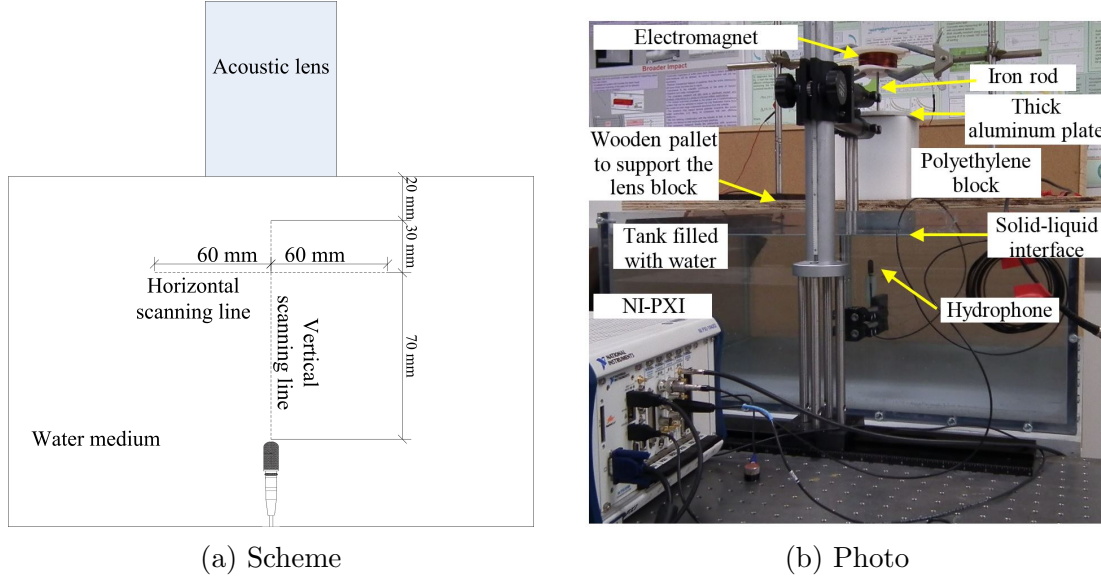
Figure 3.7: The experimental setup. (a) Scheme of the horizontal and vertical scanning lines and (b) photo of the entire setup. Figure from Ref. [48].

considered. Figure 3.8a shows the normalized water pressure recorded by the hydrophone along thehorizontal scanning line schematized in Fig. 3.7a. The vertical bars represent the standard deviation associated with the ten measurements per scanning point. The experimental data are overlapped with the results of a finite element analysis. For simplicity the analysis did not include the presence of the thin and the thick plates at the bottom and top, respectively, of the lens. The agreement between the numerical and the experimental results is remarkable. It can be seen from Fig. 3.8a that as the observation point is moved from the periphery ($x = \pm 60mm$) to the symmetric axis, the value of the pressure field doubles. Owing to the different amplitude of the solitary waves generated experimentally and numerically, a quantitative comparison between the two investigations cannot be carried. Figure 3.8b presents the experimental normalized values of the pressure amplitude as a function of the hydrophone position below the FSI along the symmetric axis (vertical scanning line in Fig. 3.7a). Here, we also compare the experiment with the finite element analysis. Interestingly, Fig. 3.8b suggests that the numerical model underestimate the amplitude decay of the acoustic pressure.

26

(a) Horizontal scan (b) Vertical scan
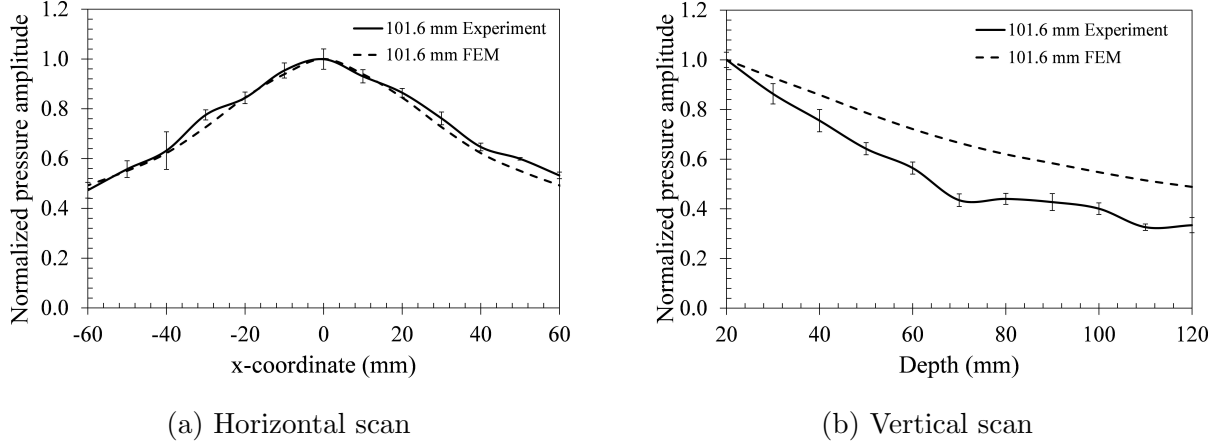
Figure 3.8: Normalized maximum pressure amplitude of both experimental and FEM results along the scanning lines (a) H and (b) V. Figure from Ref. [48].

3.5 DISCUSSION AND CONCLUSIONS

In this chapter we presented the design of a novel array to achieve acoustic focusing on a linear medium. The array consisted of one-dimensional chains of spherical particles arranged to form a circle. The granular material forming each chain supports the propagation of highly nonlinear solitary waves, which are non-dispersive and compact stress waves. The focusing properties of the acoustic lens were compared to the focusing properties achieved by a line array recently proposed [74] and based on one-dimensional chains of spherical particles subjected to differential pre-compression. Overall we found that the circle array is more practical as it does not require differential pre-compression. Besides the fact that the circular arrangement does not require any particles' tuning, we found by a quantitative comparison between the line array and the circle array, that the latter array enables larger pressure and comparable focusing area.

One interesting characteristics of the proposed system is that focusing is not achieved by deflecting the wave incident at the nonlinear-linear medium interface at a certain angle (refraction angle) or by delaying the signal emitted at each element of a phased-array controlled by a function generator. Indeed, focusing was achieved by the constructive interference of waveforms departing from the interface with a certain delay (line array designs) or simultaneously (circle array design). Time delay distribution is necessary to obtain a focal point in

27

air, liquid, or solid when a line array is adopted. For both designs, the wave field at the focal point is the result of acoustic energy coalescence and the resulting sound field is composed of a symmetric pressure maximum and minimum. As such, the proposed lens is different than the method used in most of the optic and acoustic lens where focusing is achieved by tuning the propagation direction with inhomogeneous refraction index.

4.0 ENERGY HARVESTING WITH A PIEZOELECTRIC ELEMENT

4.1 INTRODUCTION

In this study we implemented the energy harvester envisioned in Fig. 1.1 by inserting a piezoelectric element with an interface circuit to the acoustic lens designed in Chapter 3. Moreover, we improved the striker component which impacts the top particle of each chain and injects the mechanical energy into the harvester. Specifically, a plate connected to a shaker was used to tap the array in order to convert the periodic vibration provided by a shaker into solitary waves. In order to study the performance of the proposed harvester, three different nonlinear acoustic lens setups were investigated, namely arrays with four, ten and twenty chains. Then the particles were removed from the block which was then subjected to the same vibration. Finally, a cantilever beam with the same kind of PZT glued at one end of the beam was tested by shaking the other end with the identical vibration pattern used for the nonlinear harvester test and the plate test.

This chapter is organized as follows. Section 4.2 describes the proposed nonlinear energy harvester configuration and the experimental setup adopted. Section 4.3 presents the result of the experiment and of a parametric study that quantifies the power output as a function of load resistors. Section 4.3 compares the proposed system with the harvesting performance of a cantilever beam, as well as with a system similar to what was proposed here. Section 4.4 ends the chapter with some conclusive remarks.

The study reported in this chapter is published in the *ASME Journal of Vibration and Acoustics* [42] and most of the content in this chapter is excerpted from that paper.

4.2   EXPERIMENTAL SETUP

The nonlinear acoustic lens was composed of chains made of twenty stainless steel beads. The chains formed the circle array as shown in Fig. 4.1a. Three configurations were considered, namely with 4, 10, and 20 chains. An ultra-high-molecular-weight polyethylene (UHMW)
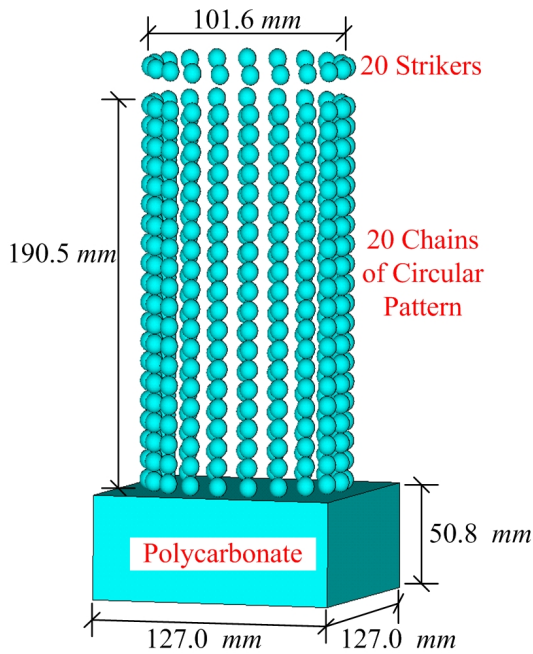
(a) Chain harvester scheme
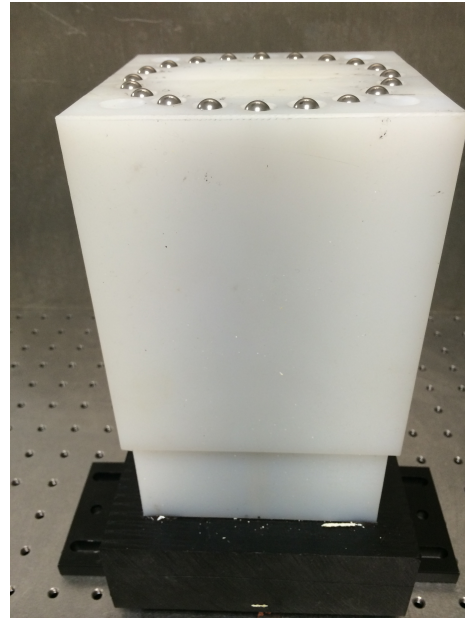
(b) Photo of the acoustic lens

(c) Front view of the striker

(d) Back view of the striker

Figure 4.1: (a) Scheme of the acoustic lens composed of 20 chains of steel beads above a polycarbonate block. (b) Photo of the acoustic lens above the linear medium block. c) Front and d) back view of the striker setup. Figure from Ref. [42].

block hosted the chains by means of twenty holes evenly distributed along a circle of $101.6mm$ in diameter. Each hole had a diameter of $9.65mm$, *i.e.* $0.13mm$ wider than the steel bead diameter ($9.52mm$). The inner wall of the holes was polished to minimize friction. The chains were tapped by means of identical stainless steel beads, glued to a thin aluminum plate as shown in Fig. 4.1c. The plate was $114.3mm$ in diameter and $1.27mm$ thick. Fresh adhesive was added to the bottom face of the plate to glue the 20 strikers and extreme care was taken to guarantee the simultaneous impact across the array.

The depth of each hole was chosen to be $2.54mm$ shorter than the total length of the 20+1 particles diameter such that the striker protruded outside the top surface of polyethylene block. Once the adhesive cured, a connection bolt was added to the plate as shown in Fig. 4.1d. The total mass of the bolt, the adhesive, the aluminum plate and all the twenty strikers was $114gr$.

The UHMW material was glued to a polycarbonate block that represented the linear medium of the system; this material was chosen since the wave speed and therefore wavelength of the stress wave was small. This led to a better performance in acoustic wave focusing [74]. The thickness of the block was equal to $50.8mm$ according to the finite element analysis (FEA) conducted earlier in Chapter 3. Figure 4.2 shows the bottom view
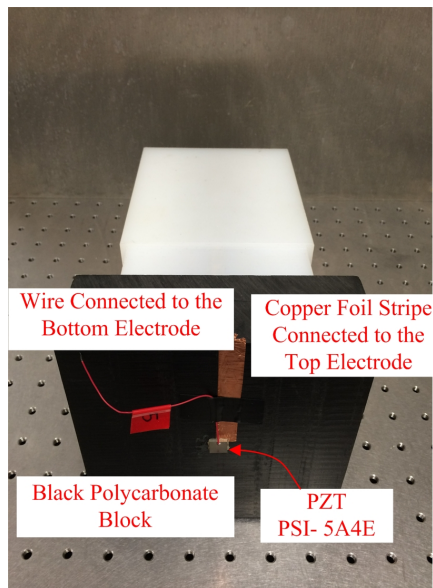
Figure 4.2: Bottom view of the nonlinear energy harvester. Figure from Ref. [42].

of the block. The figure also shows the presence of a PSI-5A4E piezoelement (PZT) from Piezo Systems, Inc. attached at the center of the polycarbonate block. The PZT was poled in the thickness direction and therefore generated electric energy from the 33 mode vibration. According to the specification provided by the manufacturer and the piezoelectric properties available in literature, such as Kim *et al.* [31], the PSI 5A4E has the product of the piezoelectric strain constant d_{33} and the piezoelectric voltage constant g_{33}, given as $d_{33} \cdot g_{33} = 9,360 \times 10^{-15} m^2/N$ which is higher than other commercially available piezoelectric elements. The parameters of the PZT are listed in Table 2.1.
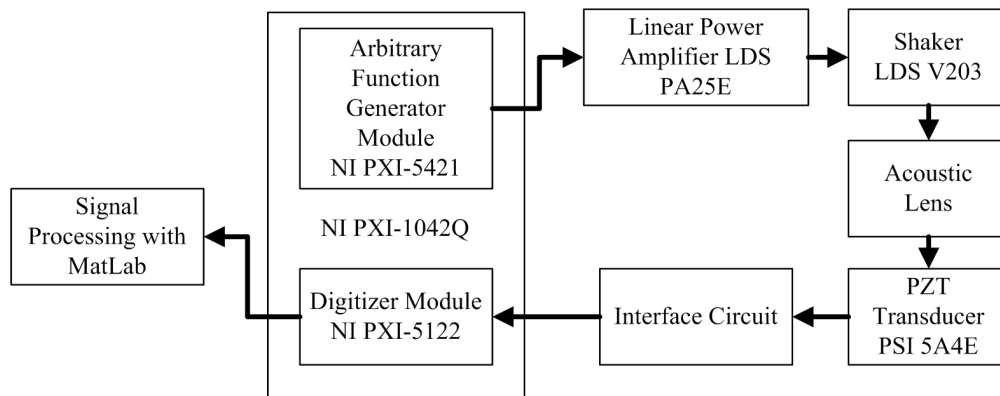
(a) Experiment workflow
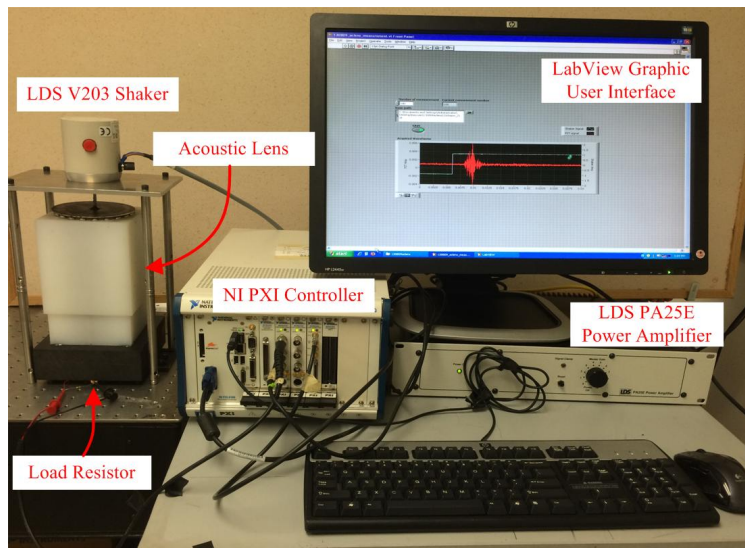
(b) Photo of the experiment setup

Figure 4.3: Experimental protocol and photo of the whole setup. Figure from Ref. [42].

The experiments were conducted following the workflow presented in Fig. 4.3a. A $1Hz$ square wave with 20% interval ratio was generated by an arbitrary function generator (NI PXI-5421). This ratio means that for one signal cycle, 20% of the period is positive voltage which drives the striker to move towards the chain while 80% of the period is negative voltage which lifts the striker. The wave was fed to a LDS V203 shaker through a LDS PA25E linear amplifier. The shaker was screwed to the connection bolt illustrated in Fig. 4.3b and drove the motion of the strikers to mimic the periodic vibration of a structure tapping the lens. When the HNSWs reached the chain-polycarbonate interface, a portion of the acoustic energy was transmitted into the linear medium where they coalesced at the position of the PZT, which converted the mechanical energy into the electrical energy in the form of a voltage output across the load resistor. The output was measured by the NI PXI-5122 digitizer and post processed in Matlab. The power across the resistive load of the integrated interface circuit was calculated as described in Section 2.3.

Several resistors were considered in order to test the harvesting performance of the system under different loads. To increase the statistical population of the experiment, 100 measurements were taken at each resistor load. Figure 4.3b displays the electronics and the experimental setup used in this study. Finally, the whole experiment was repeated twice at separate days in order to evaluate the repeatability of the whole methodology. To test this repeatability against the unfavorable conditions, the shaker and the lens were disassembled at the end of each experiment and re-assembled the day of the experiment.

4.3 EXPERIMENTAL RESULTS

4.3.1 Energy harvester with the acoustic lens

Figure 4.4 shows the interaction force between the last bead of the chain and the polycarbonate. The force profile was obtained from the discrete element model with the striker's velocity to be $0.15m/s$. It is noted here that the velocity $0.15m/s$ is an estimated value and the force profile demonstrates the shape qualitatively. The overall shape of the force is a
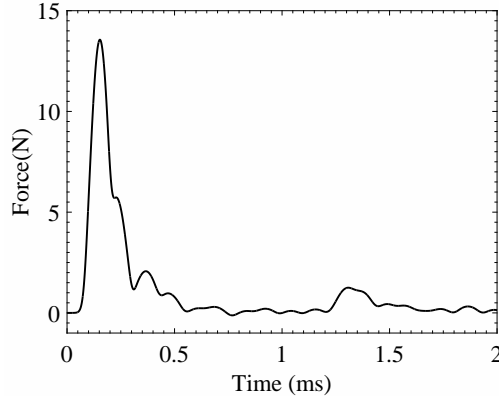
Figure 4.4: Interaction force between the chain and the polycarbonate block. Predicted qualitatively from the discrete particle model.

single pulse with an amplitude of $13.5N$ and duration of $0.3ms$. Some small pulses are visible at the time instances of $0.4ms$ and $1.4ms$. These pulses are generated since polycarbonate is softer than steel and secondary reflections are formed at the interface[79].

Figure 4.5a shows a typical time series recorded for the 20-chains setup using a $27k\Omega$ resistor. The main waveform is located in the time range $[2 - 5ms]$. The corresponding scalogram obtained by means of the Gabor wavelet transform (GWT) is presented in Fig. 4.5b and it shows the joint time-frequency content of the signal. The wavelet transform decomposes the original time-domain signal by computing its correlation with a short-duration wave called the mother wavelet that is flexible in time and in frequency. The transform determines the time of arrival and the frequency content of the propagating modes. We used the Gabor mother wavelet as it provides the best balance between time and frequency resolution, i.e., the smallest Heisenberg uncertainty box [52, 38, 70]. The acoustic energy spans mainly from 5 to $18kHz$. A low frequency component at $2kHz$ is also visible and its origin will be discussed in Section 4.3.2. Figures 4.5c and 4.5e show the time series measured when 10 chains and 4 chains were used, respectively, and the load resistor was $27k\Omega$. Figures 4.5d and 4.5f represent the corresponding wavelet scalograms. The comparison among the three waveforms denotes that the amplitudes are similar as well as the frequency content. However the duration of the signal seems to decrease when a smaller number of chains is used.

(a) Time waveform for 20 chains

(b) GWT for 20 chains

(c) Time waveform for 10 chains

(d) GWT for 10 chains

(e) Time waveform for 4 chains

(f) GWT for 4 chains
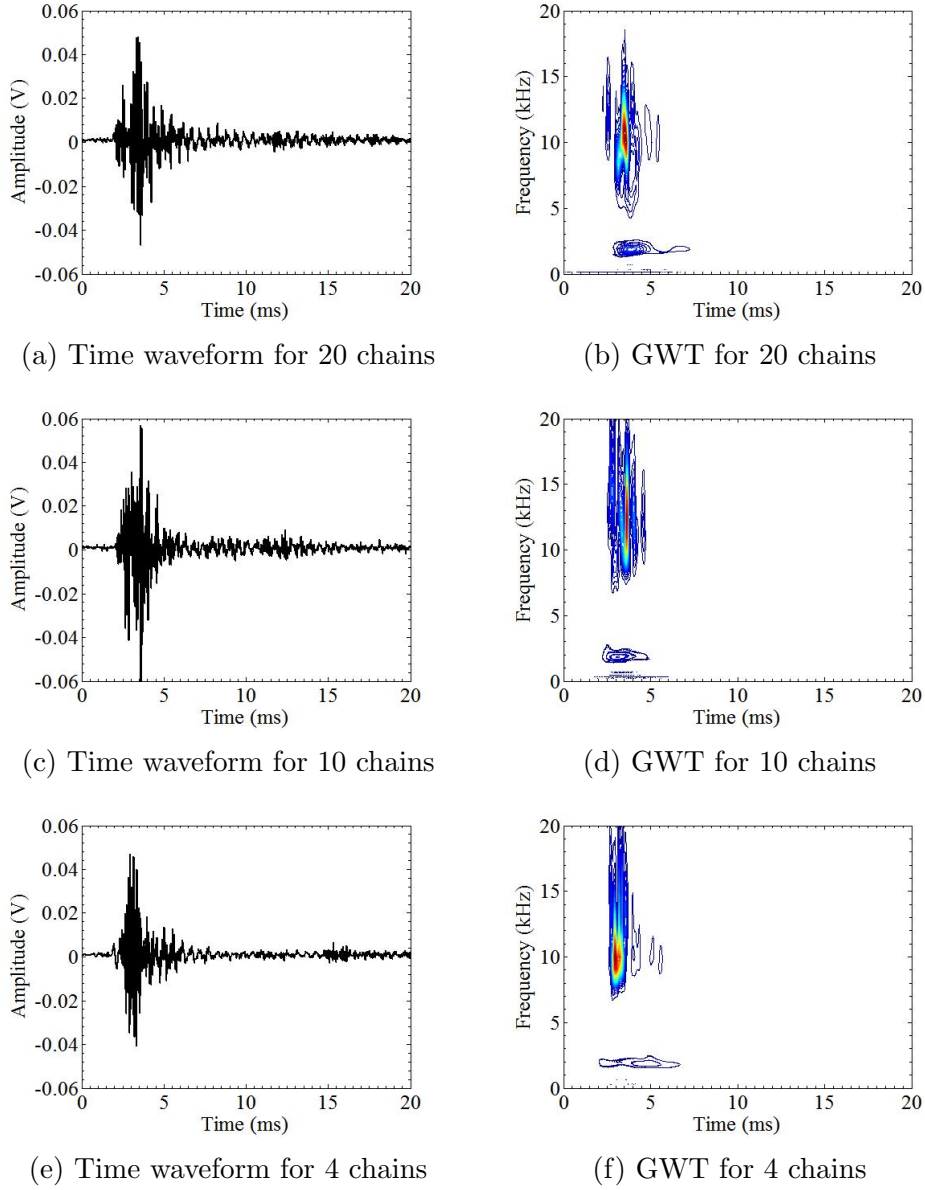
Figure 4.5: Output voltage time waveforms and corresponding Gabor wavelet scalograms of the piezoelectric element when 20, 10 and 4 chains were used and a $27k\Omega$ load resistor was connected. Figure from Ref. [42].

In order to characterize the harvesting performance among the different chain configurations, the averaged power output P from $t_1 = 2ms$ to $t_2 = 7ms$ was calculated using Eq. 2.14 in the time domain:

$$P = \frac{1}{t_2 - t_1} \int_{t_1}^{t_2} \frac{v^2(t)}{R} dt \qquad (4.1)$$

35

(a) Day 1

(b) Day 2

(c) Day 3
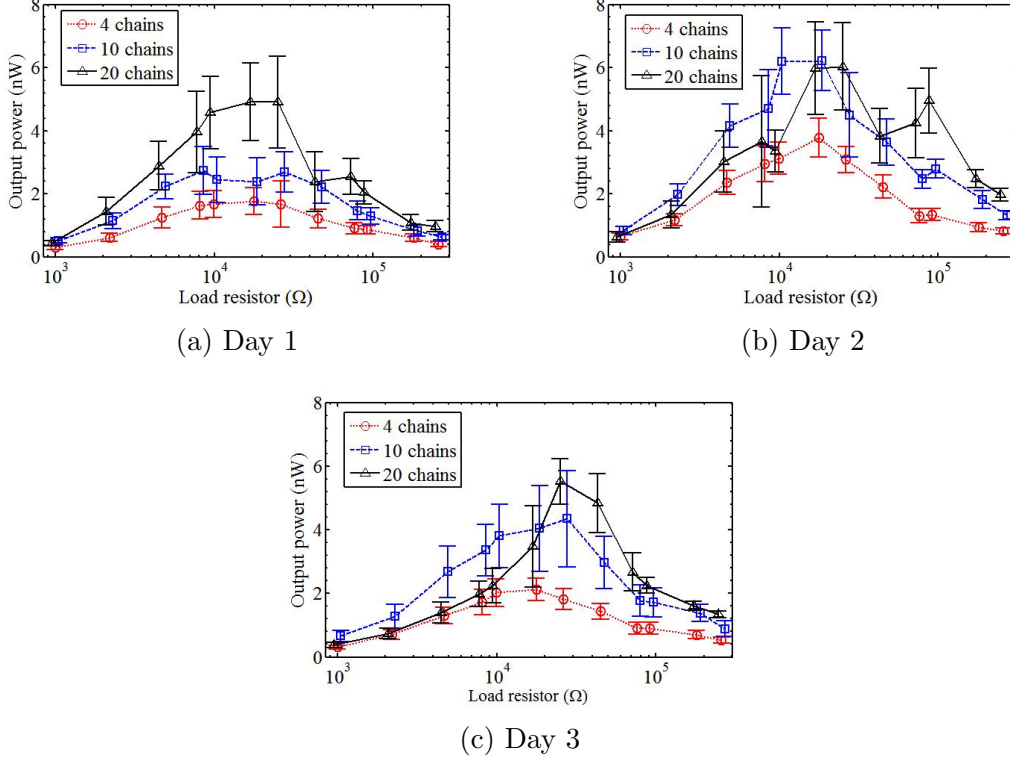
Figure 4.6: Average output power as a function of the load resistor for the three scenarios considered in this study. Figure from Ref. [42].

Figure 4.6 shows the power output P as a function of the resistor load for each day of test. Each panel presents the results associated with the 4, 10, and 20 chains. The average of the 100 strikes and the corresponding standard deviation are displayed. Figure 4.6a seems to suggest that the power across the whole spectrum of resistors is proportional to the number of chains in the lens. This evidence is not confirmed by Figs. 4.6b and 4.6c, where the 10-chains configuration provided higher power with respect to the 20-chains configuration for the load resistors below $17k\Omega$. Moreover, the error margin within the 100 measurements is relatively large and proportional to the average value of the power. This is due to the difficulty to impact all the chains simultaneously. In fact, even though extreme care was taken to guarantee that all the strikers impacted the array simultaneously, the ability to succeed is inversely proportional to the number of chains in the array. We hypothesize that the particles tolerance variation on their diameters are such that when the chains are re-assembled, the alignment achieved on day 1 was lost.

The energy harvesting performances for the three tests are summarized in Table 4.1. The numbers show the maximum power output of the test with standard deviation and the corresponding load resistor, recorded at each day of test.

Table 4.1: Summary of the three experimental results in Fig. 4.6. Table from Ref. [42].

| Day of test | Maximum power output (nW)/ standard deviation / load resistor$(k\Omega)$ | | |
	4 chains	10 chains	20 chains
Day 1	1.7/0.42/17	2.7/0.64/27	4.9/1.23/17
Day 2	3.7/0.62/17	6.2/0.96/17	6.0/1.45/27
Day 3	2.1/0.35/17	4.3/1.53/27	5.5/0.72/27

An analysis of variance (ANOVA) was conducted at the 0.05 significance level to analyze the differences among maximum power output for three configurations (20-, 10-, and 4- chains) at each day. Table 4.2 shows the ANOVA results. The F values, which indicate the ratios of the variance among configurations and the variance within configurations for three days all exceed the critical value. Therefore, for each day the null hypothesis that all the configurations generate the same maximum power output is rejected. Furthermore, a Turkey's honest significant difference (HSD) post-hoc test was performed with 95% confidence interval (CI) to compare the maximum power outputs from three configurations in each day. The Turkey test results are presented in Table 4.3. The test results show that except the 10-chain and 20-chain configurations in the second day generate similar amount of power output ($p > 0.05$), all other comparisons of means in each day indicate that the energy harvester with more chains is capable of generating higher power output.

4.3.2 Comparative analysis: plate vibration test

We compared the harvesting capabilities of the circle arrays with two other approaches, hereafter indicated as: plate vibration and cantilever. The former is described here, the

Table 4.2: ANOVA results at the 0.05 significance level.

Day	Source of variation	Sum of square	DoF	Variance	F	P
	Among groups	536	2	268.00	383.06	0.00
1	Within groups	207	297	0.700		
	Total	743	299			
	Among groups	386	2	193.00	169.87	0.00
2	Within groups	337	297	1.14		
	Total	723	299			
	Among groups	594	2	297.33	299.15	0.00
3	Within groups	295	297	0.99		
	Total	889	299			

Table 4.3: Turkey HSD post-hoc test result.

Day	Difference of chain numbers	Difference of means	95% CI	P ($\alpha = 0.05$)
	20-10	2.2	(1.92,2.48)	0.00
1	10-4	1.0	(2.92,3.48)	0.00
	20-4	3.2	(3.07,3.73)	0.00
	20-10	-0.2	(-0.56,0.16)	0.38
2	10-4	2.5	(2.15,2.86)	0.00
	20-4	2.3	(1.95,2.66)	0.00
	20-10	1.2	(0.87,1.53)	0.00
3	10-4	2.2	(1.87,2.53)	0.00
	20-4	3.4	(3.07,3.73)	0.00

latter is illustrated in Section 4.3.3. For the plate vibration test, we removed the chains from the UHMW block, and we tapped the block by means of a flat and thicker aluminum disc, as shown in Fig. 4.7. The weight of the plate was $117.5gr$. close to the weight ($114gr$) of the plate+beads system used in the previous experiment. The plate was lifted up by the same

distance of $0.82mm$. The same input was used to drive the shaker, and the same resistors were connected to the PZT. One hundred measurements were taken for each resistor. In this setup, the energy was harvested from the global vibration of the bulk materials, whereas in the acoustic lens setup the power was harvested from the energy conveyed through the solitary waves into the focal point.

Figure 4.7: Setup of the plate vibration test. Figure from Ref. [42].

Figure 4.8a shows one of the one hundred waveforms measured using the $27k\Omega$ load

(a) Time waveform

(b) GWT
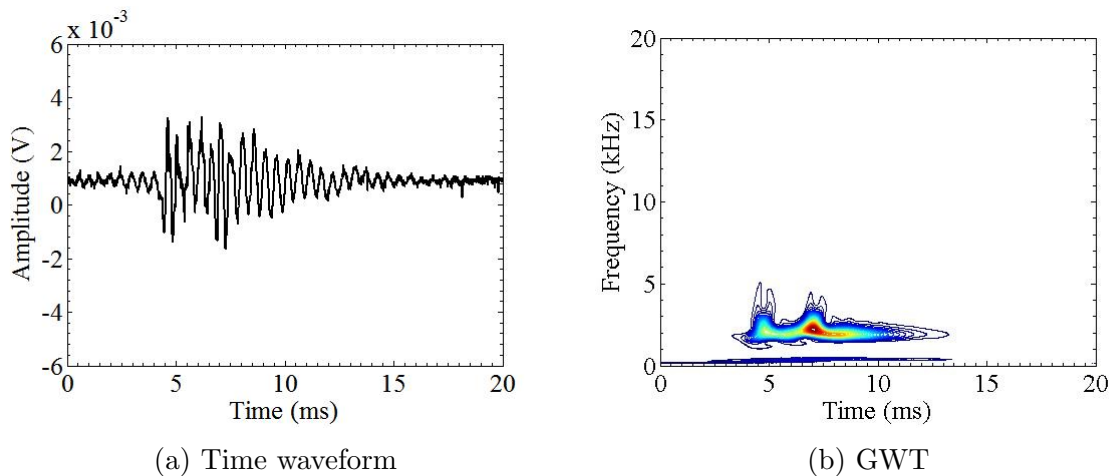
Figure 4.8: Plate vibration test. Output voltage time waveform and corresponding Gabor wavelet scalogram of the piezoelectric material under a $27k\Omega$ load resistor. Figure from Ref. [42].

resistor. The amplitude scale of the voltage time series is one order of magnitude smaller whereas the time duration is longer than the time series obtained from the acoustic lens setup presented in Fig. 4.5. Figure 4.8b shows the corresponding scalogram. Here the main frequency is located near $2kHz$ which explains the low frequency component observed in Fig. 4.5b.
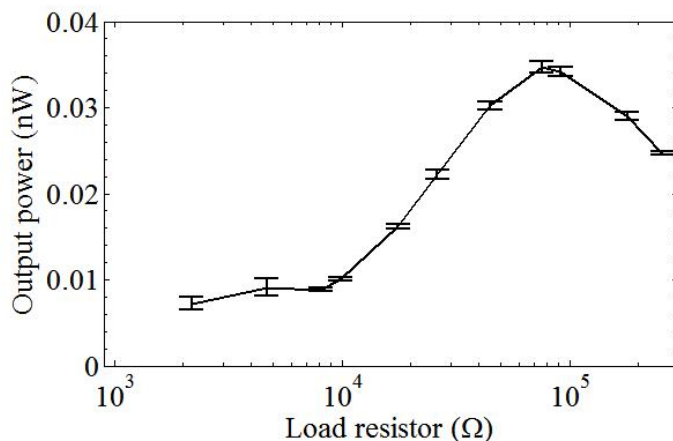
Figure 4.9: Plate vibration test. Average output power as a function of the load resistor. Figure from Ref. [42].

After removing the $1mV$ offset observed in the signals, Eq. 4.1 was utilized again to compute the power output across the load resistor within the time window $[0 - 15ms]$. The results are shown in Fig. 4.9 where the output power is plotted as a function of the load resistor. The average of the 100 strikes is presented together with the corresponding standard deviation. The datum relative to the $1k\Omega$ resistor was not computed as the signal was buried in noise. The maximum power was attained at $100k\Omega$ but it is about two orders of magnitude smaller than what attained with the acoustic lens. The difference in terms of the optimal load resistor is associated with the output impedance of the PZT. As shown in Eq. 2.12, the power is maximized when the load resistor matches the output impedance of the PZT. With respect to the acoustic lens setup, the output impedance $Z(\omega)$ was higher since the angular frequency ω of the vibration was lower; thus, the maximum power output is achievable with a larger load resistor. The results presented in Fig. 4.9 denote higher repeatability when compared to the acoustic lens test, but much smaller power output, as there is no energy focusing at the location of the PZT.

4.3.3 Comparative analysis: cantilever beam test

Another identical PSI-5A4E piezoelement was bonded to the tip of a cantilever beam as shown in Fig. 4.10. The beam was $200mm$ long, $60mm$ wide, and $0.4mm$ thick. One end of the beam was secured to the shaker, that was fed with the same signal used to tap the nonlinear acoustic lens. The same testing protocol illustrated in Section 4.2 was adopted here.

(a) Top view scheme   (b) Photo
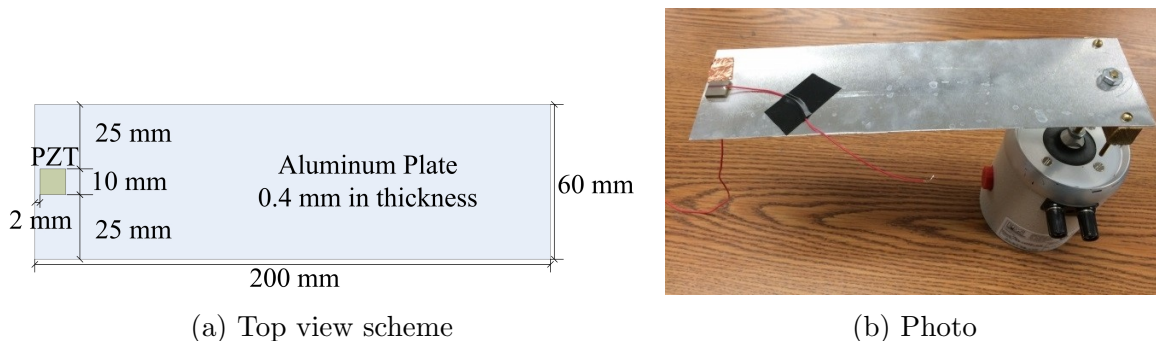
Figure 4.10: Cantilever beam test experimental setup, (a) top view scheme; (b) photograph. Figure from Ref. [42].

Figure 4.11 shows a typical time series and the corresponding scalogram measured when the $27k\Omega$ load resistor was used. When compared to the time waveforms measured in the other experiments, the duration of the signal is tenfold longer and the main frequency is lower. We applied a well-established analytical model described in Ref. [19] to compute the system's first resonance frequency. We found that this frequency is equal to $149Hz$ which is very close to the experimental value of $150Hz$.

The average power was calculated across the time window $[0 - 100ms]$ and the results are presented in Fig. 4.12 which shows the power as a function of the load resistor. As done in the previous experiments, 100 measurements were taken for each resistor. The graph shows that the experiment was highly repeatable. The monotonic increase of the power with respect to load resistor value above $10k\Omega$ is due to the fact that the PZT has high electric impedance when vibrating at low frequencies. Recalling Eq. 2.10 at a certain low frequency ω_L, the impedance of the PZT $Z_{PZT} = 1/(j\omega_L C_{PZT})$ is larger than the value R of the load resistor, and the power output is directly proportional to R when $R < |Z_{PZT}|$. The decreasing trend visible below $5k\Omega$ is due to the low signal noise ratio.

(a) Time waveform

(b) GWT
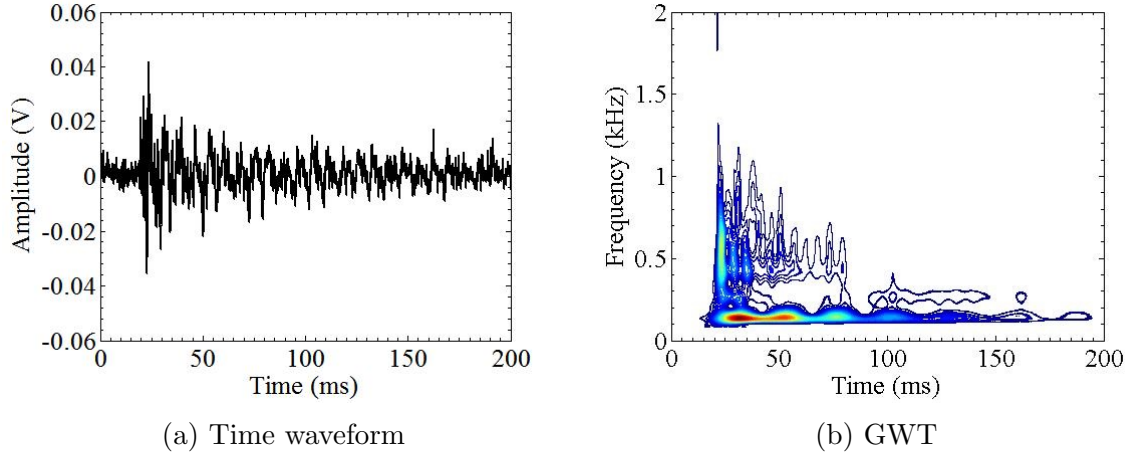
Figure 4.11: Cantilever beam test. Output voltage time waveform and corresponding Gabor wavelet scalogram of the piezoelectric element with a $27k\Omega$ load resistor. Figure from Ref. [42].
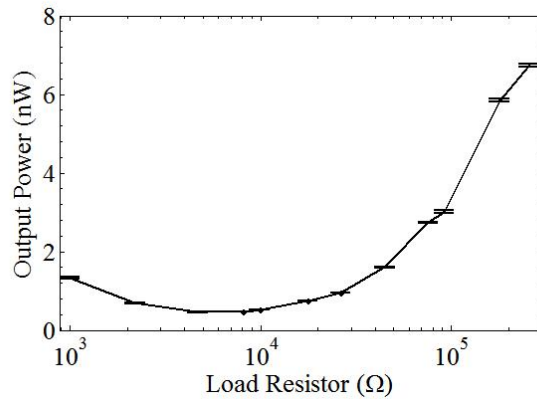
Figure 4.12: Cantilever beam test. Average output power as a function of the load resistor. Figure from Ref. [42].

To summarize and compare the harvesting performance of the systems presented in this paper, in Fig. 4.13 we averaged the results of the three days for each acoustic lens test, and compared the averaged results with the cantilever beam test result. We did not include the outcome of the plate test as the energy harvested was two orders of magnitude smaller. The setup with the 20 chains yielded to the largest output provided the load resistor was below $100k\Omega$. According to Eq. 2.8 and Eq. 2.9, the value of the optimal load resistor is determined only by the PZT vibration frequency. Table 4.4 predicts these optimal values using the center frequencies determined by means of the waveforms' scalograms, and compared the optimal values with experimental result. The optimal resistor for the cantilever beam is at $1300k\Omega$,

corresponding to a vibration of $150Hz$. The table demonstrates a good agreement between the experimental and the predicted values relative to the acoustic lens.

We remark here that the comparative analysis was carried out by maintaining the similarities between this novel harvester and the two other systems as close as possible. As such, we: 1) used the same kind of PZT; 2) considered the same resistors; 3) adopted the same tapping motion; and 4) used the same vibration source both in terms of amplitude and repetition rate. For example the selection of the mode 33 PZT allows the harvesting of the energy associated with the out-of-plane motion of the cantilever beam rather than the in-plane deformation. Not shown here, we instrumented the same beam with a second PZT, attached close to the beam's root. The same test protocol was adopted and the results show that the tip PZTs harvests more energy than the root PZT at any load resistor above $4k\Omega$.

4.4   DISCUSSION AND CONCLUSIONS

In this chapter we have presented an energy harvester based on the use of an acoustic lens in contact with a linear bulk medium. The lens consists of an array made of one-dimensional chains of spherical particles assembled to form a circle. The grains support the propagation of highly nonlinear solitary waves, which are non-dispersive and compact stress waves. The chain are arranged spatially to achieve acoustic focusing at the bottom surface of the linear
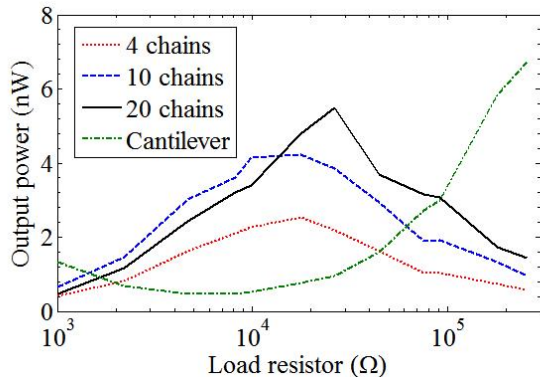
Figure 4.13: Comparison of the energy harvesting performance among the nonlinear harvester tests with 4/10/20 chains of beads and the cantilever beam test. Figure from Ref. [42].

Table 4.4: Comparison between the predicted optimal load resistor values and the actual optimal load resistor values. Table from Ref. [42].

Harvester type	Experimental dominant frequency(kHz)	Experimental optimal resistor ($k\Omega$)	Predicted optimal resistor ($k\Omega$)	Maximum power output (nW)
4 chains	10	17	20	2.5
10 chains	10	17	20	4.3
20 chains	10	27	20	5.5
Plate vibration	2	100	97	0.034
Cantilever beam	0.15	> 500	1300	> 6.7

medium where a wafer-type PZT is glued to convert the mechanical energy into electricity. To quantify the amount of power that can be harvested the PZT is connected to an interface circuit of a varying resistance load. The overarching hypothesis of this research is that a vibrating structure tapping the lens produces compact solitary waves that coalesce into the linear medium and focus at the location of the PZT. The lens thus conveys weak vibrations from a structure into focused pulses that are converted into electricity. The vibration is provided by a shaker that taps the lens at predefined speed and frequency. We tested the lens considering three different numbers of chains and we found that the power harvested is dependent on this number but it is not linearly proportional. The harvesting performance of our system was compared to a similar system where the granular particles were removed and vibration was transmitted to the PZT by means of the vibration of the material supporting the chain and the bulk linear medium. The power harvested by this latter system is found to be two orders of magnitude smaller. Finally, the proposed system was compared to a non-optimal short cantilever beam subjected to the same action of the shaker. A PZT of the same family was placed at the tip of the beam. The results demonstrated that the two systems generate comparable power output and the lens based harvester generates higher power than the cantilever beam when the load resistance is below $100k\Omega$ which is well above the value of the resistance of most electric devices. The proposed system is bulkier than the

cantilever system and it may not be feasible as is. Nonetheless, the grain-based harvester could be buried whereas the cantilever beam needs free space to oscillate.

5.0 ENERGY HARVESTING PERFORMANCE COMPARISON BETWEEN CHAINS AND RODS

5.1 INTRODUCTION

In Chapter 3, we compared the stress field generated in a linear medium by line and circle arrays made of 1D granular chains [48]. We demonstrated that the circle array overcomes some of the shortcomings associated with the line arrays. In Chapter 4, we applied the novel array for energy harvesting [42]. In the study presented in this chapter we expanded the work of Ref. [42] to compare experimentally the performance of the granular system with a similar array where the spheres were replaced by solid rods.

The chapter is organized as follows. Section 5.2 introduces the experimental setup. Section 5.3 presents the results of the experiments and of a parametric study that quantifies the power output as a function of load resistors. Section 5.4 ends the chapter with some concluding remarks and suggestions for future works.

The study reported in this chapter is published in the *Journal of Applied Physics* [43] and this chapter is excerpted from that paper.

5.2 EXPERIMENTAL SETUP

The experiment protocol was identical to the one described in Section 4.2 for the grain-based harvester. The only difference was that for the rod-based harvester, the grains were replaced by the steel rods shown in Fig. 5.1a. They were made of steel type 304, had the same diameter of the grains, and the same length of the chains, *i.e.* $20 \times 9.52 = 190.4mm$. The

surface of each rod was polished to minimize friction with the inner wall of the hole. One end of each rod was tapered as shown in Fig. 5.1b to allow the contact between the rod and the host medium. It is important to note here that 100 measurements were taken for each test case.

(a) Photo of the whole rod   (b) Photo of the rod end   (c) Scheme of the rod end
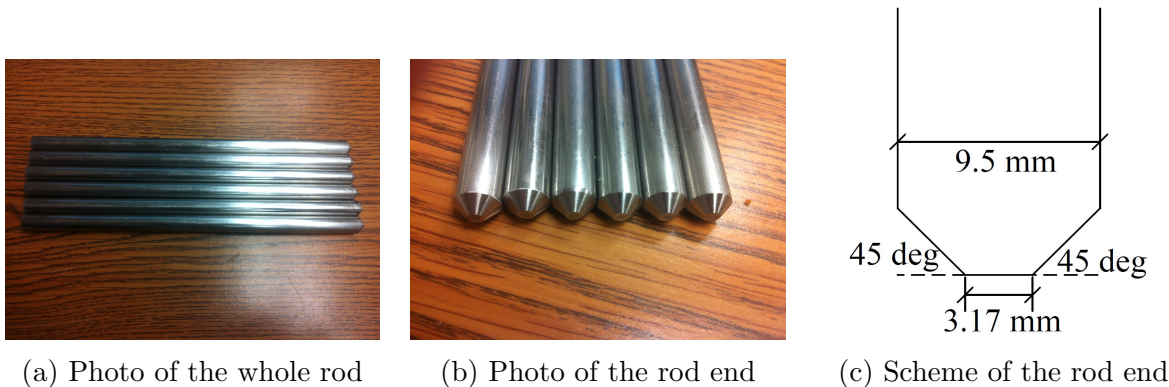
Figure 5.1: Configurations of the steel rods. Figure from Ref. [43].

5.3   EXPERIMENTAL RESULTS

Figure 5.2a shows one time series recorded when 20 rods were used and the $27k\Omega$ resistor was connected to the PZT. The main waveform was tailed by a few wave packets. The corresponding GWT scalogram is presented in Fig. 5.2b. The dominant frequency spans from $8kHz$ to $20kHz$. A $2kHz$ component is also visible and is associated with the global vibration of the system.

The comparison of power output between the rod- and grain- based harvesters is presented in Fig. 5.3 as a function of the load resistor. For each data point, 100 measurements were taken to obtain the power output and the vertical bars represent the standard deviation of the 100 samples at each data point. Figure 5.3b was obtained via Eq. 4.1 by considering the time interval $t_1 = 3ms$ and $t_2 = 20ms$. For comparison purpose, the power output from the chain harvester in Day 1 (Fig. 4.6a) is presented in Fig. 5.3a. To ease the comparison between the two panels in Fig. 5.3, the vertical scales for both figures were left the same. Fig. 5.3b shows that the power is proportional to the number of rods and it is much smaller

(a) Time waveform

(b) GWT
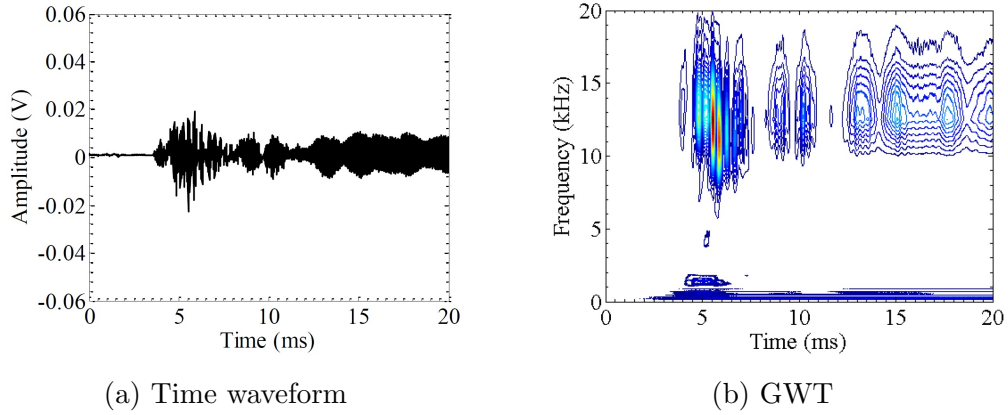
Figure 5.2: Time series and corresponding Gabor wavelet scalogram obtained from the PZT when 20 rods and a $27k\Omega$ load resistor were used. Figure from Ref. [43].
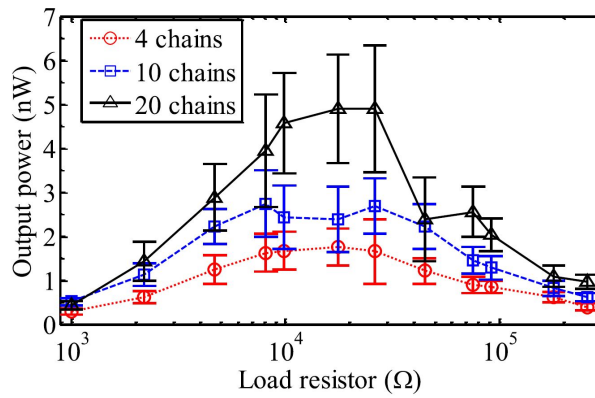
(a) Grain-based harvester
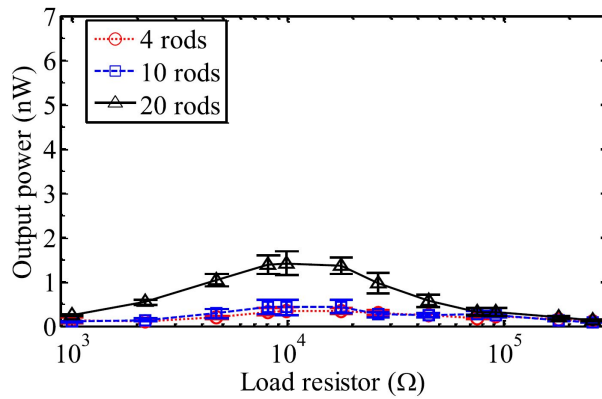
(b) Rod-based harvester

Figure 5.3: Average power output as a function of the load resistor for the rod- and grain- based harvesters. To ease the comparison, the ordinate axes are left the same. Figure from Ref. [43].

than the power generated by the granular carriers. We notice that the repeatability of the power output is better since the standard deviation of the experimental data is smaller.

5.4 DISCUSSION AND CONCLUSIONS

In the study presented in this chapter we compared the performance of a harvester made of chains of spherical particles with a harvester made of an array of rods. The chains and the rods were arranged in a circular pattern to allow the focusing of linear waves at the bottom of a polycarbonate block where a wafer-type PZT was glued to convert the mechanical energy into electricity. The amount of power that can be harvested was quantified by connecting the PZT to an interface circuit of varying resistance load. We found that the granular array is able to deliver a compact acoustic energy to the PZT whereas the array of rods transmits the vibration imparted by the tappet. We found that the harvester with more chains or more rods is able to produce higher power output because more carriers are used to deliver the acoustic energy to the PZT. However, the configuration with the largest number of carrier is challenging as the simultaneous impact across the whole array must be secured. We also found that the grain-based harvester produces voltage output with the higher amplitude and more compact profile. This is due to the unique properties of the nonlinear medium (the chain of beads) compared to the linear medium (the rods).

6.0   PARAMETRIC STUDY: NUMERICAL ANALYSIS

6.1   INTRODUCTION

To boost the energy density of our HNSW-based harvester, we investigated the effect of some of the harvester components on the electrical power output. In particular we examined the material and geometry of the particles and the linear medium, and the boundary conditions of the piezoelectric element. We conducted a numerical study based on the DPM and FEA to predict the electric power that can be harvested.

This chapter is organized as follows. Section 6.2 studies analytically the effect of the PZT boundary condition upon the energy harvesting performance. Sections 6.3 and 6.4 present the setup and results of the parametric study where different bead and block materials were considered. Sections 6.5 and 6.6 present the setup and results of the parametric study where the diameter of the particles and the diameter of the array were changed. Finally, Section 6.7 ends the chapter with some conclusive remarks.

Part of the study presented in this chapter was published in *Smart Materials and Structures* [47], and part was submitted to the *ASME Journal of Vibration and Acoustics* [46].

6.2   EFFECT OF PZT'S BOTTOM BOUNDARY CONDITIONS

The selected transducer is poled in the thickness direction, which is also the direction of vibration. The governing equation for the free PZT can be written as [22]:

$$S_3 = s_{33}^E + d_{33}E_3 \tag{6.1a}$$

$$D_3 = d_{33}T_3 + \epsilon_{33}^T E_3 \tag{6.1b}$$

where 3 denotes the thickness direction, S is the strain, T is the stress, E is the electric field, D is the electric displacement field, s^E is the mechanical compliance at zero electric field, ϵ^T is the dielectric constant at zero stress, d is the induced strain coefficient, *i.e.* the mechanical strain per unit electric field. In our study, for the sake of simplicity, we neglected the coupling effect between the thickness direction and the two in-plane directions [22]. Considering the Newton's second law, $T_3' = \rho\ddot{u}_3$ where ρ is the PZT density, u_3 is the displacement in the thickness direction, and the strain displacement relation, $S_3 = u_3'$, Eq. 6.1b yields the wave equation:

$$\ddot{u}_3 = c^2 u_3'' \tag{6.2}$$

where $c^2 = (\rho s_{33}^E)^{-1}$ is the wave speed squared [22]. In all the above the following notation is used: $()' = \partial/\partial x_3$, $\dot{()} = \partial/\partial t$.

When the PZT is attached to the block, its bottom face at $x_3 = l$ can be considered free, *i.e.* $\partial u_3/\partial x_3|_{x_3=l} = 0$ while its top face $x_3 = 0$ responds to the structural vibration and the linear waves. The boundary conditions can be written as [22]:

$$u_3(0,t) = U(t) = U_{a0}\cos\omega t \tag{6.3a}$$

$$u_3'(l,t) = 0 \tag{6.3b}$$

In Eq. 6.3, for simplicity, the structural vibration is considered harmonic with angular frequency ω and amplitude of U_{a0}. We used the subscript $a0$ to indicate the free PZT condition. The solution for the boundary condition problem is

$$u_3(x_3,t) = [U_{a0}\cos(kx_3) + U_{a0}\tan(kl)\sin(kx_3)]\cos(\omega t) \tag{6.4}$$

51

where $k = \omega/c$ is the wavenumber. The electric voltage generated across the PZT is [27]:

$$V_0(t) = g_{33}s_{33}^E \int_0^l S_3 dx_3 = g_{33}s_{33}^E u_3|_0^l = g_{33}s_{33}^E U_{a0}[\cos(kl) + \tan(kl)\sin(kl) - 1]\cos(\omega t) \quad (6.5)$$

where g_{33} is the piezoelectric voltage constant which defines the ratio of the electric field strength to the effective mechanical stress. When the bottom face of the PZT is fixed, the boundary conditions become:

$$u_3(0, t) = U(t) = U_{a1}\cos\omega t \quad (6.6a)$$

$$u_3(l, t) = 0 \quad (6.6b)$$

Here the subscript a1 denotes the boundary condition of the fixed PZT, and U_{a1} represents the top displacement amplitude and the voltage output is given by:

$$V_1(t) = g_{33}s_{33}^E \int_0^l S_3 dx_3 = g_{33}s_{33}^E u_3|_0^l = g_{33}s_{33}^E U_{a1}\cos(\omega t) \quad (6.7)$$

A comparison between Eq. 6.5 and Eq. 6.7 can be carried out by, for example, assuming $f = 10kHz$, $c = 2.58mm/\mu s$, and $l = 2mm$, and identical load displacements, i.e. $U_{a0} = U_{a1}$. The frequency of $10kHz$ was observed experimentally in [42] and it is confirmed by the numerical data presented later in Section 6.3. These values yield to $kl = 0.048$ while the voltage ratio of the fixed PZT case to the free PZT case is:

$$V_1/V_0 = 1/(\cos(kl) - 1 + \tan(kl)\sin(kl)) \approx 2/(kl)^2 \approx 800 \quad (6.8)$$

Eq. 6.8 shows that the restraint of the bottom surface of the PZT increases the energy that can be harvested. It is noted here that is a real case, $U_{a1} < U_{a0}$, and therefore, the ratio $V_1/V_0 < 800$.

6.3   MATERIAL-WISE PARAMETRIC STUDY: SETUP

To predict the PZT's power output more accurately and to investigate the effect of certain parameters of the harvester, a discrete particle model (DPM) and an FEA were formulated. The DPM was used to predict the force profile of the solitary wave at the chain's particle in contact with the solid. At the contact point the interaction of the sphere with the solid was modeled by imposing the equilibrium of the forces [74], the resultant force at the solid represents the input of an FEA model to predict the linear wave propagation in the block. Four materials were considered for the beads, namely aluminum, stainless steel, titanium, and tungsten. Four materials were also selected for the linear medium, namely aluminum, polycarbonate, stainless steel and copper. These materials were chosen because their mechanical properties, which are listed in Table 6.1, vary significantly and they are commercially available.

Table 6.1: Properties of the materials considered in this study. Table from Ref. [47].

Material	Density (kg/m^3)	Young's modulus (GPa)	Poisson's ratio	Mechanical loss factor
Tungsten	19250	411	0.28	N/A
Copper	8960	120	0.34	2×10^{-3}
Stainless steel 302	8100	196	0.33	2×10^{-3}
Titanium	4506	116	0.32	N/A
Aluminum	2700	70	0.35	2×10^{-3}
Polycarbonate	1230	3.45	0.35	0.056

The energy harvesting system we propose is schematized in Fig. 6.1. An array of twenty chains of particles is located above a $152.4mm \times 152.4mm \times 50.8mm$ solid. Each chain consists of twenty identical $9.5mm$ diameter spheres. The chains are arranged along a circle of $50.8mm$ radius, and they are subjected to the impact of a striker, which is a bead identical to the particles forming the array. The impact triggers the formation of the solitary waves.
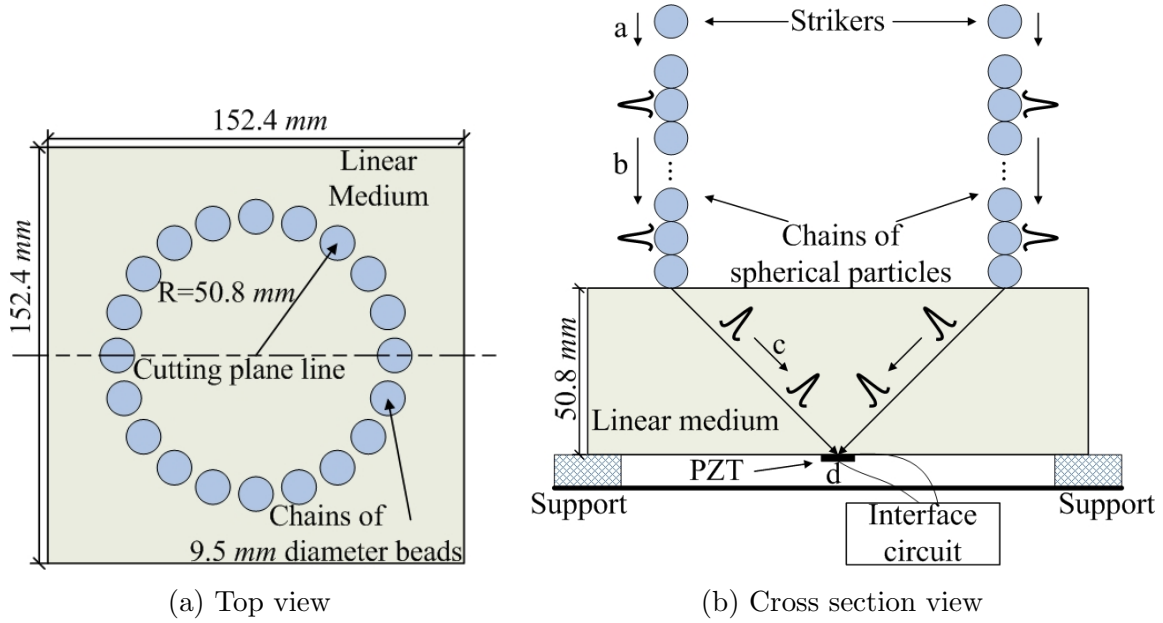
Figure 6.1: (a) Top view of the HNSW-based energy harvester. (b) Schematics of the cross section cut by the cutting plane line in (a). The letters indicate the overall process: a. the strikers impact the chains; b. HNSWs are generated and propagate along the chains; c. the HNSWs radiate inside the solid, become linear bulk waves, and coalesce at bottom's centroid; d. a PZT attached at the centroid converts the mechanical stress into electric potential. Figure from Ref. [47].

At the interface with the solid, part of the acoustic energy is reflected back to the chain and part is transmitted into the block where it propagates as a bulk wave. All the bulk waves irradiating from the contact point coalesce at the centroid of the bottom face of the block. Here, a $10mm \times 10mm \times 2mm$ PSI-5A4E transducer, schematized in Fig. 6.2, is glued to the block to convert the mechanical vibration into electrical potential. The PZT is connected to an interface circuit with a purely resistive load in order to evaluate the power output of the PZT.
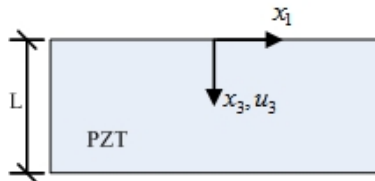
Figure 6.2: Cross section of the PZT. Figure from Ref. [47].

To simulate the wave propagation inside the solid and to predict the voltage output from the PZT, an FEM was built using ANSYS v13.0. Figure 6.3 shows the model. Owing to

the symmetry of the harvester, only a quarter of the system was modeled using symmetric boundary conditions applied to the two planes of symmetry and constraining the vertical displacement of the nodes at the bottom edges of the block. The block was modeled with the SOLID185 3D 8-node element with three degrees of freedom (DOFs) per node. The PZT was modeled using the SOLID226 3D 20-node coupled field solid with three displacement DOFs and one voltage DOF for each node. The top and the bottom electrodes were simulated by coupling the voltage DOF of the top and bottom nodes, respectively. The elements of the PZT were coupled to the linear medium elements by sharing the same nodal displacement at the interface. The bottom edges of the linear medium were constrained with fixed vertical displacement to avoid the rigid body motion and to simulate the presence of supported boundary conditions (see Fig. 6.1b).
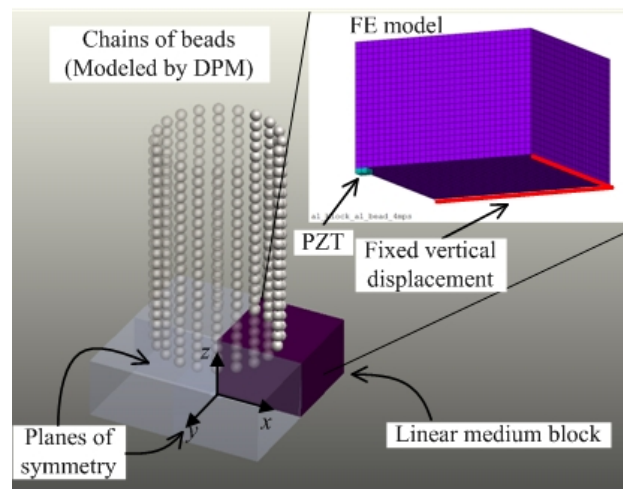
Figure 6.3: Schematics of the HNSW-based energy harvester and a close-up view of the FEM of the linear medium coupled with the PZT. Figure from Ref. [47].

Transient analysis was performed. The force profiles obtained from the DPM were applied at the contact point between the last particle of each chain and the linear material. To achieve good accuracy the dimension of each finite element was $2.5mm$ equal to $1/60$ of the shortest wavelength expected in the polycarbonate at the associated frequency of $10kHz$. The sampling frequency was equal to $500kHz$. The model also included Rayleigh damping [50] in the frequency range between $1 - 20kHz$ in order to account for dissipation in the bulk material.

6.4 MATERIAL-WISE PARAMETRIC STUDY: RESULTS

6.4.1 Energy harvester with different striker velocities

The first parameter we considered was the velocity of the striker. We ran two simulations in which the striker velocities were equal to $0.4m/s$ and $4m/s$, respectively. For both simulations, the beads were made of stainless steel, the linear material was polycarbonate, and the bottom face of the PZT was considered free. Figure 6.4 shows the open circuit voltage, *i.e.* the output when the PZT is connected to an infinite load resistor. For the sake of clarity the values associated with the slower strikers are represented in the right ordinate axis. The result indicates that the faster strikers generate an electric potential that is approximately twentyfold higher. It is known that the speed of the solitary wave is proportional to the maximum dynamic contact force which, in turn, is proportional to the speed of the striker [15]. Conversely, the speed of bulk waves in the linear medium is independent on the waves' amplitude. Figure 4 shows the voltage output generated by the PZTs with striker initial velocities of $0.4m/s$ and $4.0m/s$, and assuming that all the waves arrive at the location of the PZT simultaneously. In Fig. 6.4, $t = 0$ corresponds to the instant at which the solitary pulses irradiates from the chain-block interface.
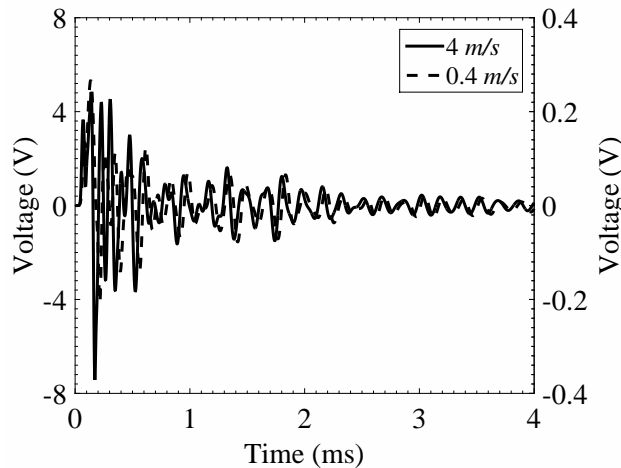
Figure 6.4: Open circuit voltage output of free PZT with two striker velocities. The left and right axes are associated with the $4m/s$ and $0.4m/s$ velocities, respectively. Figure from Ref. [47].
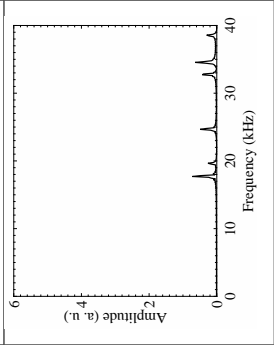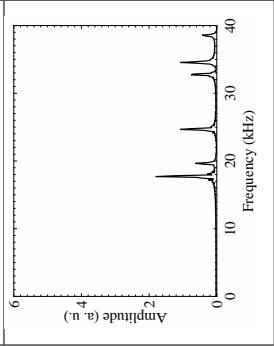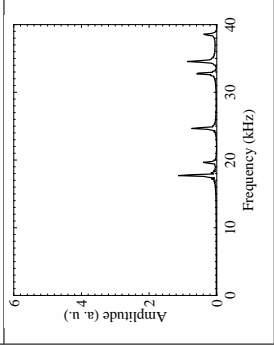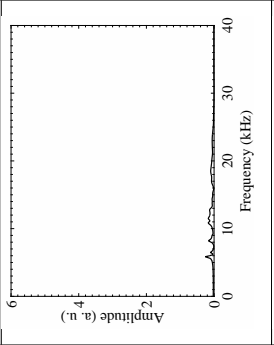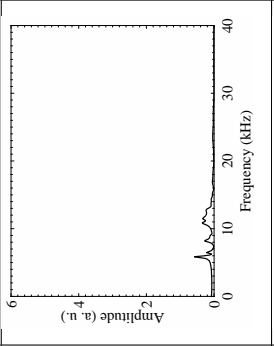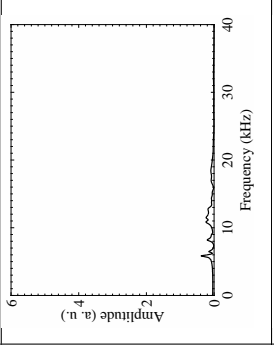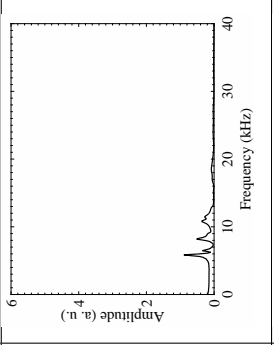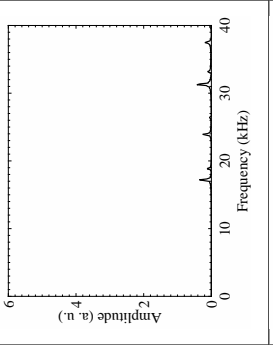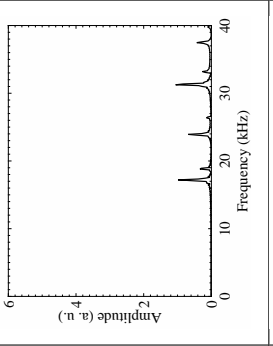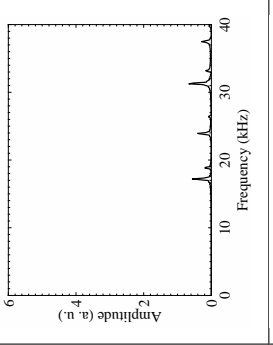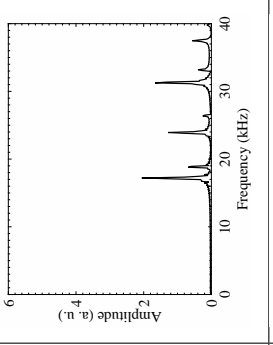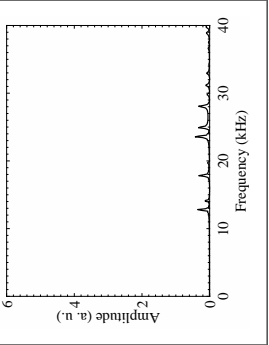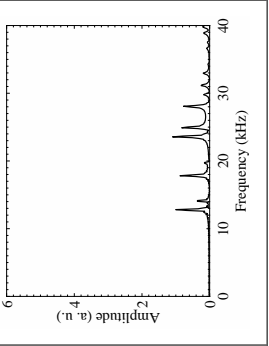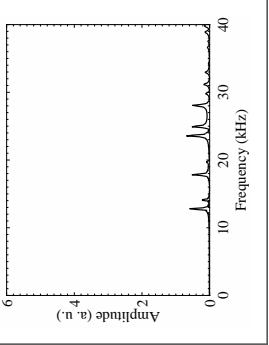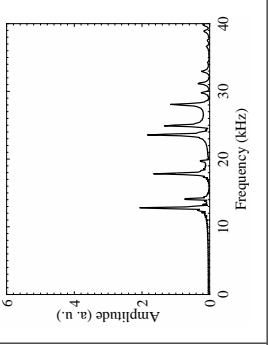
6.4.2 Energy harvester with a free PZT

Next, we examined the best combination of granules and solid materials. Hereinafter, the initial velocity of the strikers was considered equal to $4m/s$. Table 6.2 shows the open circuit voltage output under free PZT condition for the 16 possible combinations. To ease the comparison among the 16 cases the vertical scale is left the same. The table shows that the tungsten beads provide the highest potential irrespective of the block material. This is the effect of the largest momentum carried by the tungsten strikers. The panels also show that the waves propagating inside the polycarbonate decay faster than in any other solid as a result of the mechanical loss factor. By observing the 16 waveforms, we note that the tungsten beads in contact with the copper solid provide the highest potential and this is in principle the best setup to harvest energy. Any cost or fabrication consideration of such combination is beyond the scope of this study and it is therefore neglected. The waveforms presented in Table 6.2 also suggest that the frequency content of the signals depends on the materials being used. To quantify this aspect, Table 6.3 displays the corresponding fast Fourier transform (FFT). The frequency spectra depend mainly on the solid. The waves propagating through the polycarbonate have a frequency peak around $5kHz$ whereas the stress waves propagating through steel show a peak at around $18kHz$.

Table 6.2: Open circuit voltage output from the free PZT. Table from Ref. [47].

Bead / Block	Aluminum	Stainless steel	Titanium	Tungsten
Aluminum				
Polycarbonate				
Stainless steel				
Copper				

Table 6.3: FFT spectra of the time waveforms presented in Table 6.2. Table from Ref. [47].

Bead / Block	Aluminum	Stainless steel	Titanium	Tungsten
Aluminum				
Polycarbonate				
Stainless steel				
Copper				

(Each cell contains an FFT spectrum plot with axes: Amplitude (a. u.) on the vertical axis ranging 0 to 6, and Frequency (kHz) on the horizontal axis ranging 0 to 40.)
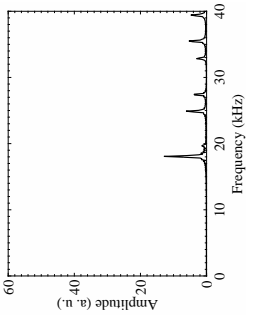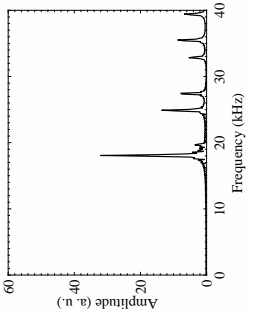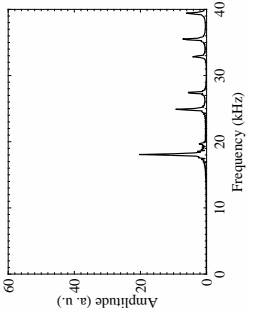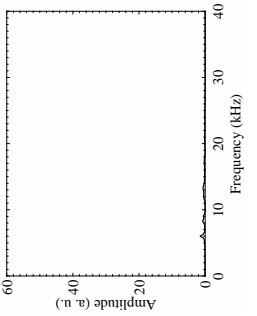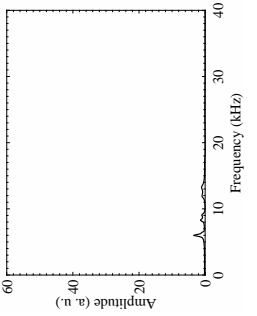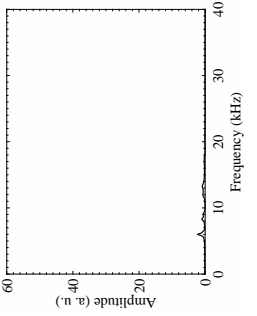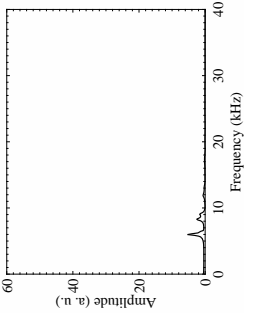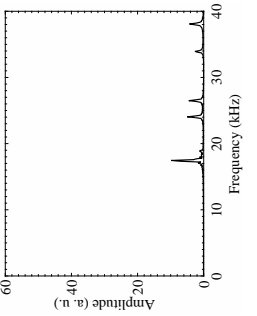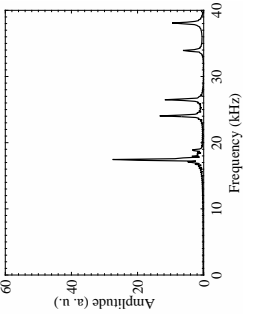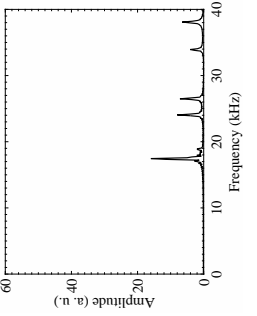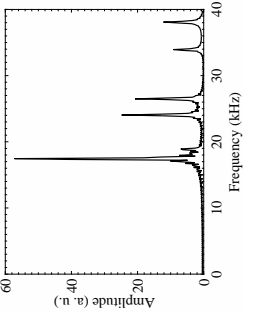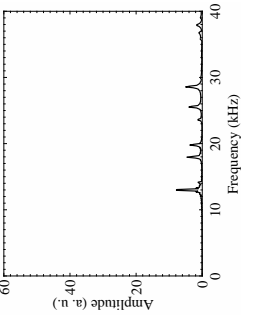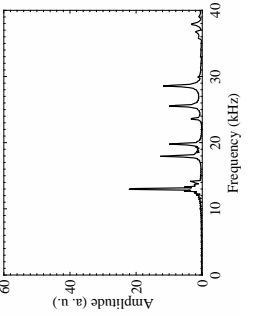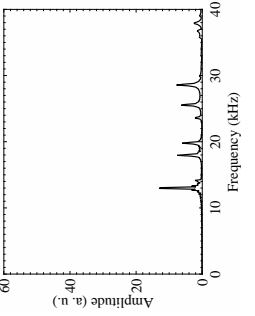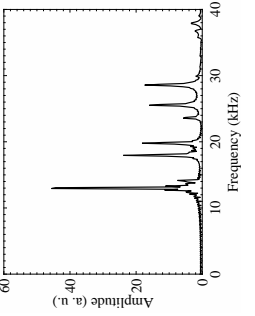
6.4.3 Energy harvester with a fixed PZT

To evaluate the effect of the transducer's boundary condition, we run the same FEM analysis and restrained the motion of the nodes at the bottom face of the PZT. The results are presented in Table 6.4 and they show that the voltage is at least one order of magnitude higher than the corresponding waveforms presented in Table 6.2. This agrees qualitatively with the analytical prediction discussed in Section 6.2. However, the voltage ratio is lower than the one estimated in Eq. 6.8, since the top displacement load for the fixed PZT case in Section 6.2 is much larger than the real case. In terms of the best materials combination, Table 6.2 suggests that the tungsten beads in contact with either steel or copper provide the highest output. For the sake of completeness, Table 6.5 displays the frequency spectra of the waveforms presented in Table 6.2. When compared to the spectra presented in Table 6.3, we observe that the frequency content is essentially the same, with very few exceptions. This implies that the boundary conditions of the PZT do not change the frequency characteristics of the voltage output but only its amplitude.

Table 6.4: Open circuit voltage output from the fixed PZT. Table from Ref. [47].

Block \ Bead	Aluminum	Stainless steel	Titanium	Tungsten
Aluminum				
Polycarbonate				
Stainless steel				
Copper				

Table 6.5: FFT spectra of the time waveforms presented in Table 6.4. Table from Ref. [47].

Bead \ Block	Aluminum	Stainless steel	Titanium	Tungsten
Aluminum				
Polycarbonate				
Stainless steel				
Copper				

6.4.4 Output power calculation

The power output was calculated by Eq. 2.14 in the frequency domain. It is noted that R represents the resistor variable, Z_{PZT} is a constant, and $V_{open}(\omega)$ is the spectra shown in Tables 6.3 and 6.5.

Figures 6.5 and 6.6 shows the power output for the cases of the free PZT and the fixed PZT, respectively. Each figure is represented with the same scale in order to ease the direct comparison among the four different solids. The value of the ordinate scale demonstrates that fixing the PZT dramatically boosts the power that can be harvested. Figure 6.6c shows that the tungsten chains in contact with the steel block and fixed PZT connected to a $10k\Omega$

(a) Aluminum block with free PZT (b) Polycarbonate block with free PZT

(c) Stainless steel block with free PZT (d) Copper block with free PZT
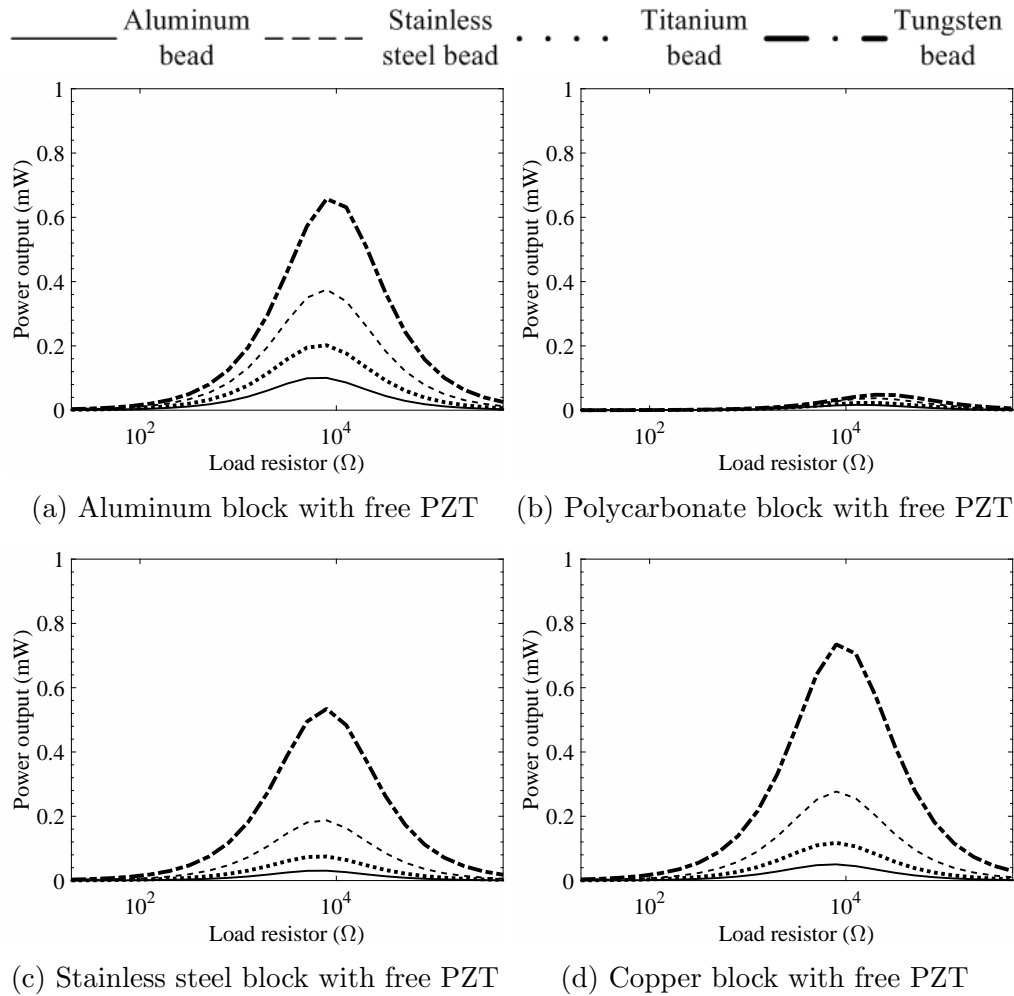
Figure 6.5: Power output of generated by HNSW-based energy harvester under different load resistors with free PZTs. Figure from Ref. [47].
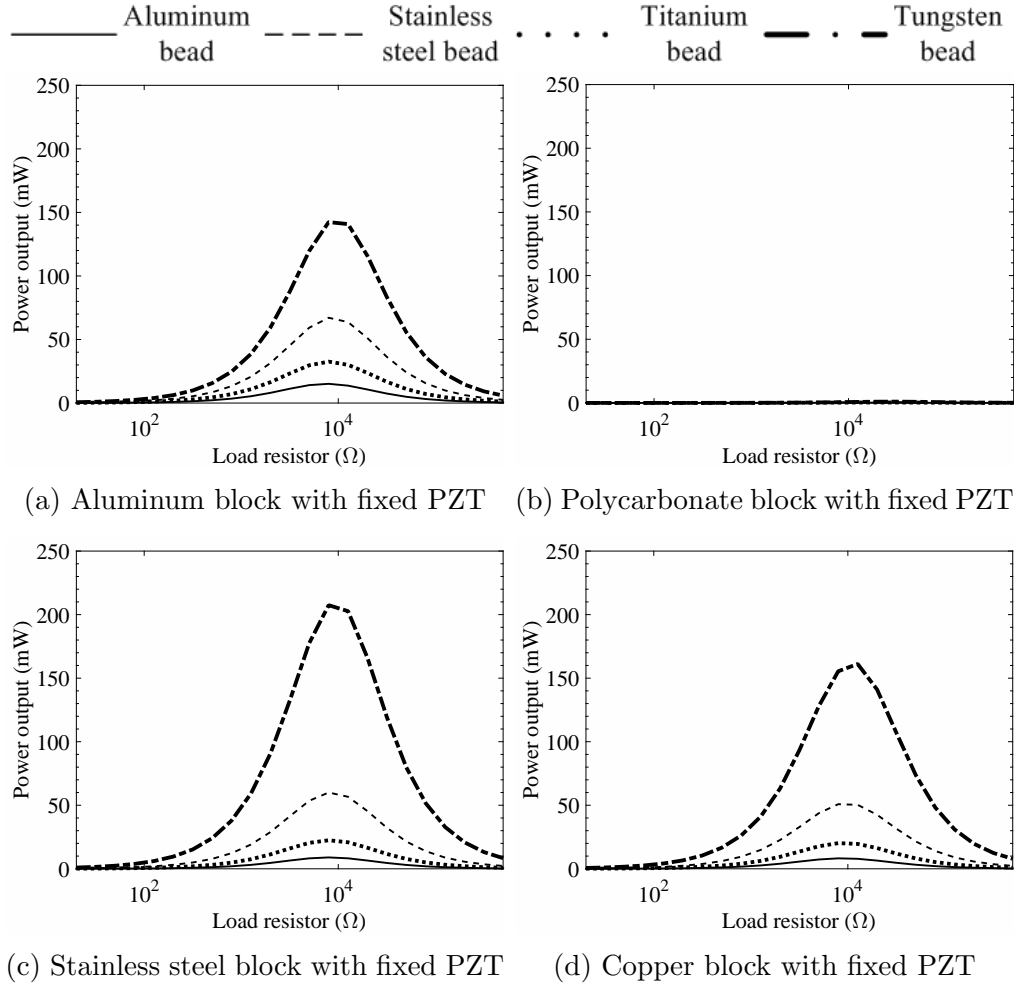
Figure 6.6: Power output of generated by HNSW-based energy harvester under different load resistors with fixed PZTs. Figure from Ref. [47].

resistor provides $220mW$ of power. This value is about 400 times larger than the same combination with a free PZT. Figures 6.5 and 6.6 also show that for a given solid, the power is proportional to the beads' density as a results of the large kinetic energy provided by the strikers. The metallic blocks generate higher power than the polycarbonate as a result of the frequency content of the stress waves reaching the PZT. As shown in Table 6.3 and Table 6.5, the polycarbonate block generates voltage waveform lower than $10kHz$ whereas other metallic blocks generate waveforms of $15kHz$ or higher. Therefore, according to Eq. 2.12 the load resistor value at peak power output for the polycarbonate block should be higher than other metallic block cases. This agrees with Figs. 6.5 and 6.6. Also, the peak

power amplitude for metallic blocks should be higher than the polycarbonate block since the voltage amplitude and vibration frequency of the metallic blocks are both higher than the polycarbonate block. This also agrees with the outcome in Figs. 6.5 and 6.6.

6.5   GEOMETRY-WISE PARAMETRIC STUDY: SETUP

In order to improve the energy harvester's performance from a geometric perspective, a parametric study was conducted. Four stainless steel blocks were considered, namely $304.8mm \times 304.8mm \times 101.6mm$, $304.8mm \times 304.8mm \times 50.8mm$, $152.4mm \times 152.4mm \times 50.8mm$, and $76.2mm \times 76.2mm \times 50.8mm$. Three sets of metamaterials were considered. Each set was composed of 20 chains evenly distributed on a circumference. The large set consisted of $19.1mm$ diameter particles arranged in a $203.2mm$ diameter circle. The medium metamaterial consisted of $9.5mm$ diameter particles arranged in a $101.6mm$ diameter circle. The small set consisted of $4.8mm$ diameter particles arranged in a $50.8mm$ diameter circle. Hereinafter these three sets are indicated as $19.1mm/203.2mm$, $9.5mm/101.6mm$, and $4.8mm/50.8mm$ bead/array diameters, respectively. The diameter of the array was proportional to the diameter of the bead to be able to allocate the chains along a circle. Table 6.6 summarizes the geometries investigated in this parametric study, and it clusters the nine simulations

Table 6.6: Geometric parameters of the harvester considered in this study. Clusters of the simulations. Table from Ref. [46].

Block size	Block thickness	Bead diameter (mm)/array diameter(mm)		
$(mm \times mm)$	(mm)	4.8/50	9.5/101.6	19.1/203.2
304.8×304.8	101.6	x	x	x
	50.8	x	x	x
152.4×152.4	50.8	x	x	
76.2×76.2	50.8	x		

conducted in this study. Group 1 and Group 2 studied the effect of the metamaterial size at two different block thickness. Group 3 and Group 4 studied the effect of the block's size, at a given bead/array size.

6.6 GEOMETRY-WISE PARAMETRIC STUDY: RESULTS

6.6.1 Single chain versus array of 20 chains

To demonstrate the advantage of the circular arrangement, we first compare the harvesting performance between a single chain and an array of 20 chains. The scope is to show that twenty harvesters made of a single chain are much less cost-effective than a single harvester with twenty chains. Figure 6.7 presents the two configurations to be compared. The size of the linear medium and of the beads was the same for both harvesters. For both cases, the loading force profiles were identical at the contact point between each chain and the block since we assumed the same striker's initial velocity.

(a) 20 chains   (b) 1 chain
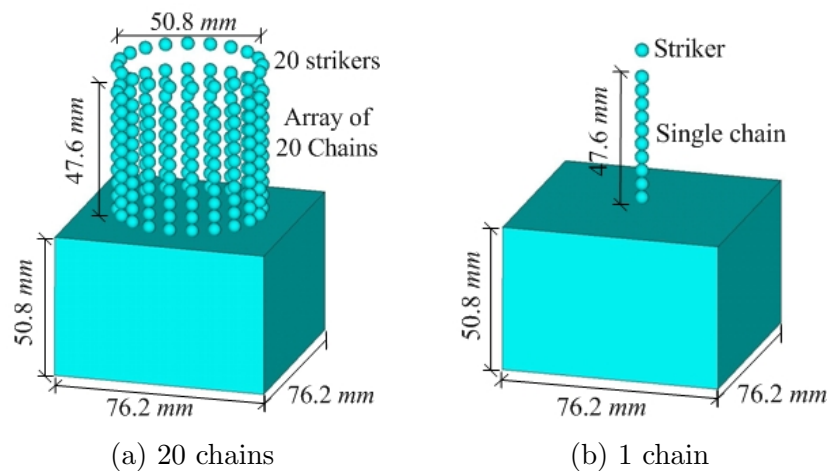
Figure 6.7: Schematics of the harvesters with an array of 20 chains and a single chain. The bead diameter is 4.8mm. Figure from Ref. [46].

Figures 6.8a and 6.8c present the time waveforms relative to the array and the single chain, respectively. To ease the immediate comparison between the two cases, the vertical scale of the figures is identical. The voltage amplitude provided by the array harvester is less than 20-fold the amplitude of the single chain due to beam spreading. Figures 6.8b and

6.8d show the FFT spectra corresponding to the time waveforms in Figs. 6.8a and 6.8c, respectively. The same dominant mode at $25kHz$ is visible.

(a) 20 chains

(b) 20 chains

(c) 1 chain

(d) 1 chain
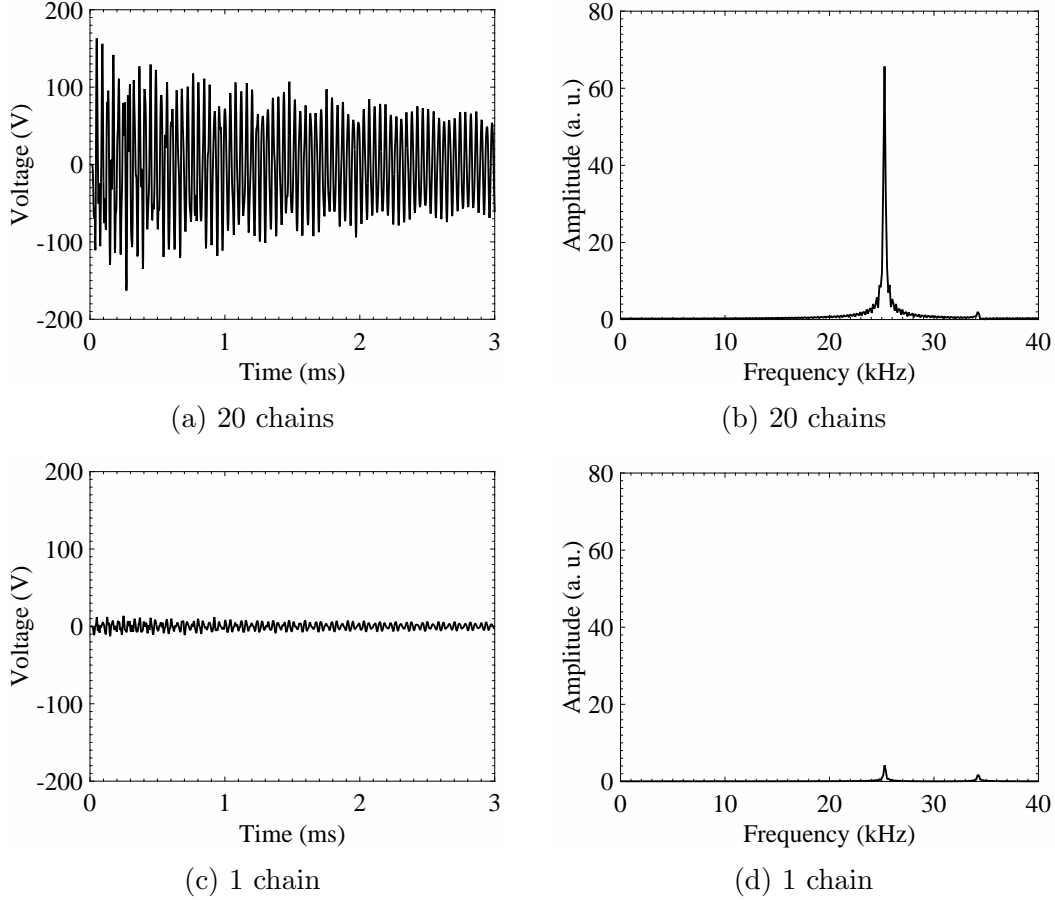
Figure 6.8: Simulation results for the same linear medium block size of $76.2mm \times 76.2mm \times 50.8mm$. (a) and (c) Time waveforms obtained from the PZT for 20 chains and a single chain, respectively. (b) and (d) FFT spectra of (a) and (c), respectively. Figure from Ref. [46].

Figure 6.9 shows the power output as a function of load resistors for both cases. Note that the vertical scale associated with the single chain is two orders of magnitude smaller than the vertical scale associated with the array. The single chain harvester provides a power of $1.5mW$ while the array-based harvester generates $281.4mW$, which is 180 times higher. In terms of power density, the single chain and the array provide $5nW/mm^3$ and $918nW/mm^3$, respectively. This demonstrate that the array design is more cost effective because it provides more power with less material and volume.
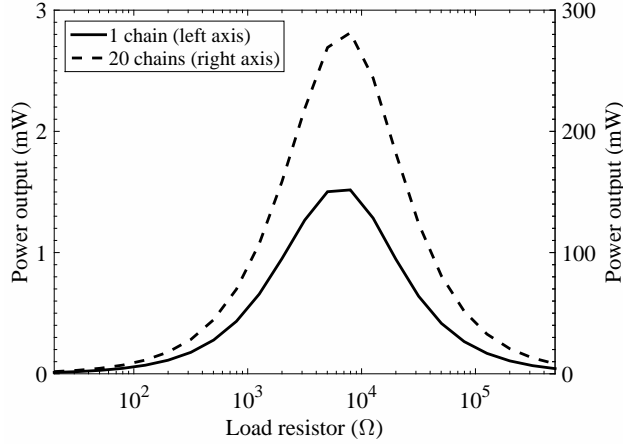
Figure 6.9: Power output as a function of load resistors for two cases with different number of chains. Figure from Ref. [46].

6.6.2 Energy harvester performance with different bead/array diameters

Figures 6.10 shows the results relative to the analysis of Group 1 in which the linear medium was $304.8mm \times 304.8mm \times 101.6mm$. The left panels of Fig. 6.10 displays the open circuit PZT voltage time waveforms associated with the three different particles and array diameters. The amplitude is proportional to the bead diameter because larger strikers convey more kinetic energy into the harvester and the whole system vibrates with a higher amplitude. The right panels of Fig. 6.10 shows the corresponding FFT spectra. The peaks' frequencies are inversely proportional to the bead diameter because the time duration of the input force at the chain block interface is shorter when smaller beads are considered. Therefore, the oscillating element tapping smaller beads tends to excite bulk waves with higher frequencies. Figure 6.11 presents the power output of the PZT as a function of the load resistors. The harvester with the largest bead size generates the highest power equal to $135.7mW$ at $20k\Omega$, while the harvester with the smallest beads generates the lowest power equal to $10.5mW$ at $10k\Omega$. The resistor at which the maximum is achieved is proportional to the bead size, because it is a function of the frequency, according to Eq. 2.13. The optimal load resistor, which equals the impedance of the PZT according to Eq. 2.9, should be smaller when higher frequencies are excited, *i.e.* in this case when smaller particles are used.
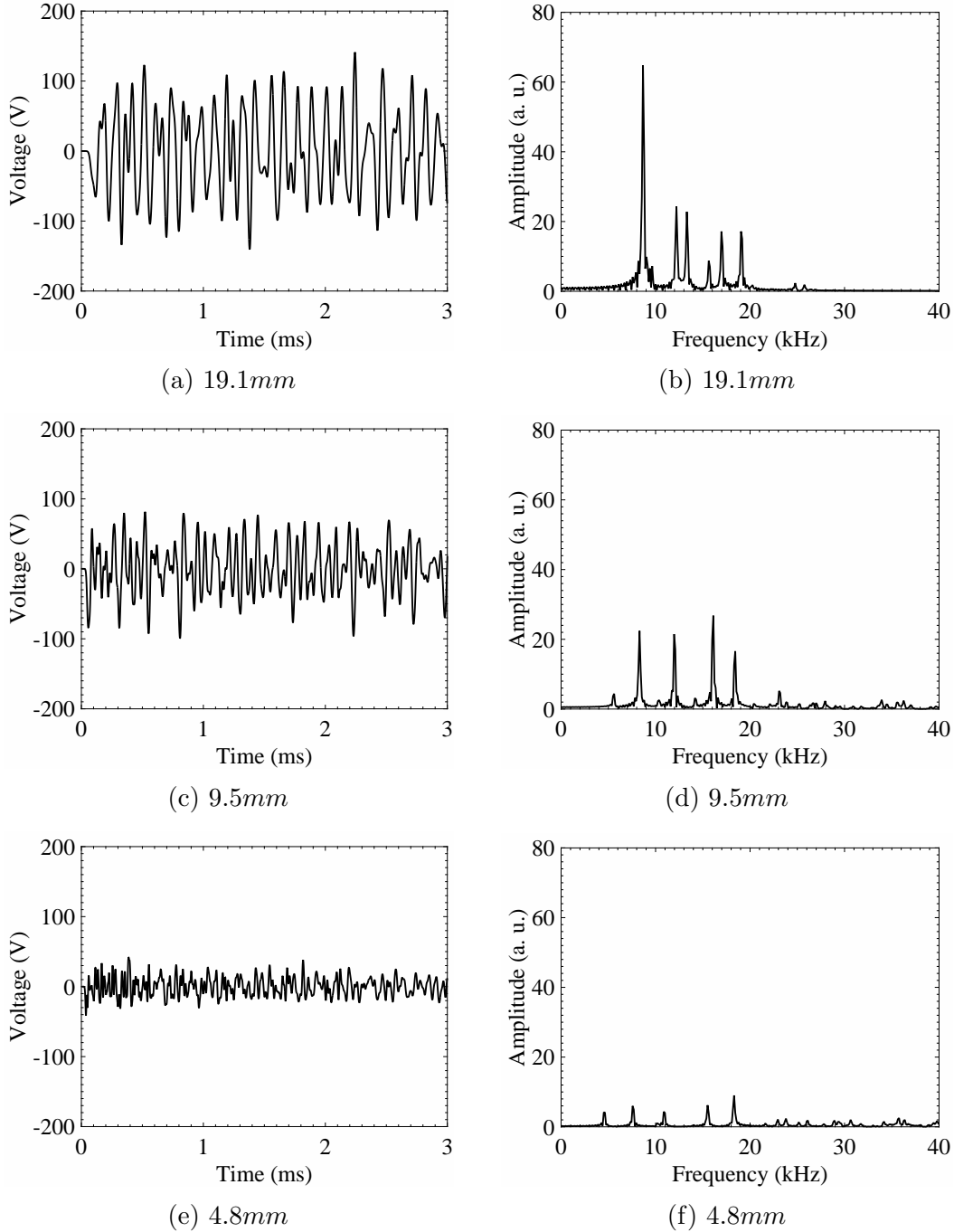
Figure 6.10: Simulation results for the same linear medium block size of $304.8mm \times 304.8mm \times 101.6mm$. (a), (c) and (e) Time waveforms obtained from the PZT when the bead diameters /array diameters are $19.1mm/203.2mm$, $9.5mm/101.6mm$ and $4.8mm/50.8mm$, respectively. (b), (d) and (f) FFT spectra of (a), (c) and (e), respectively. Figure from Ref. [46].

Figure 6.12 shows the results relative to Group 2, where the thickness of the solid was halved and the other parameters were identical to those considered in Group 1. Figures 6.12a,

69

Figure 6.11: Power output as a function of load resistors for three cases with different bead diameters in Fig. 6.10. Figure from Ref. [46].

6.12c and 6.12e displays the time waveforms associated with the three different particles and array diameters whereas Figures 6.12b, 6.12d and 6.12f show the corresponding FFTs. The plots reveal that the amplitude is not proportional to the bead diameter. In fact, the medium size array generates higher voltage than the large array made of $19.1mm$ beads. This result suggests that beam spreading must be taking into account for the design of the harvester. To validate our hypothesis, Fig. 6.13 schematizes the mechanism of the beam spreading. Since the chains are perpendicular to the solid, the force function is perpendicular to the chain/solid interface. This yields the largest longitudinal vibration in the vertical direction. Moreover, the line of sight between the contact point and the PZT is longer when larger array's diameter is considered. By comparing Fig. 6.13a with Fig. 6.13b, when the largest particles are used, the PZT is 63 deg off the vertical direction. Therefore, a small component of the longitudinal wave can reach the PZT, which operates in through-thickness. The frequency content of the three signals shows that smaller beads induce higher frequencies, similar to the cases discussed for Group 1. The frequency content in Fig. 6.12f for the smallest bead case is more spread comparing to the other cases with larger beads. This is due to the fact that the shorter time duration of the input force load results in a wider frequency spectrum, *i.e.* a more broadband excitation. Therefore, more vibration modes of the structure are excited. Finally, Fig. 6.14 displays the power output of the PZT as a function of the load resistor. As expected by examining the time waveforms, the highest
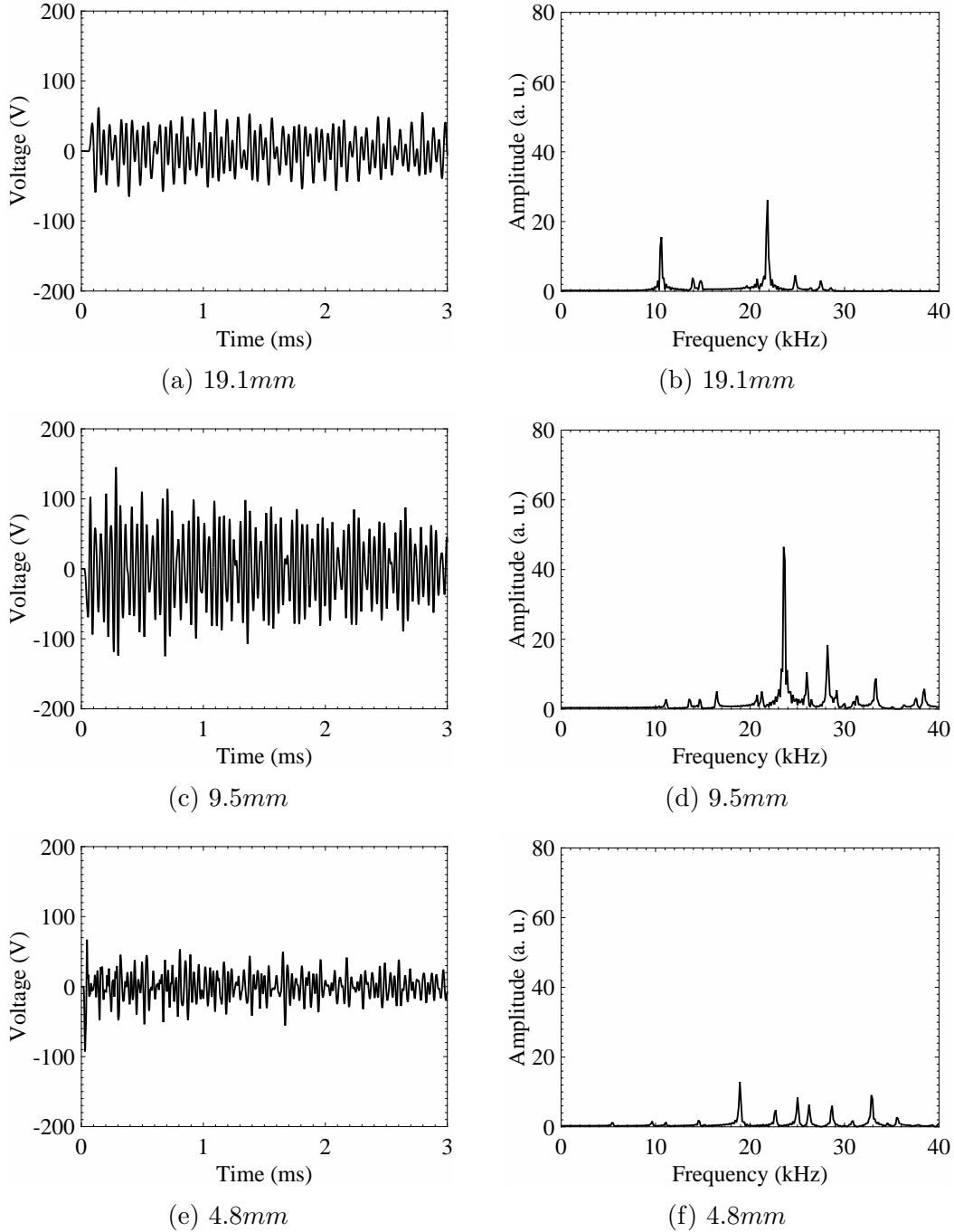
Figure 6.12: Simulation results for the same linear medium block size of $304.8mm \times 304.8mm \times 50.8mm$. (a), (c) and (e) Time waveforms obtained from the PZT when the bead diameters /array diameters are $19.1mm/203.2mm$, $9.5mm/50.8mm$ and $4.8mm/50.8mm$, respectively. (b), (d) and (f) FFT spectra of (a), (c) and (e), respectively. Figure from Ref. [46].

power was produced by the medium harvester and it was equal to $187.9mW$ when the load resistor was equal to $8k\Omega$.
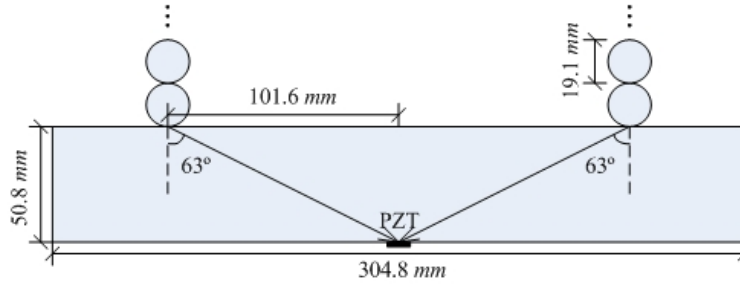
(a) large beam spreading
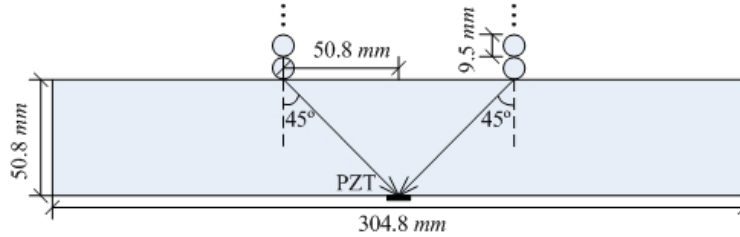
(b) small beam spreading

Figure 6.13: Comparison of beam spreading configurations. Cross section views of (a) the harvester with the array of 101.6mm diameter and (b) the harvester with the array of 50.8mm diameter. Figure from Ref. [46].
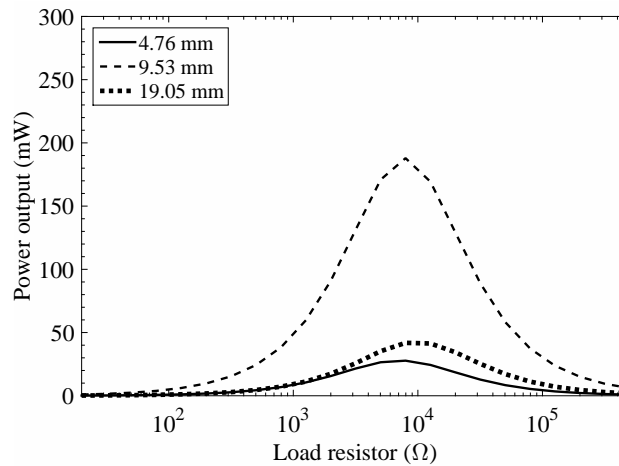
Figure 6.14: Power output as a function of load resistors for three cases with different bead diameters in Fig. 6.12. Figure from Ref. [46].

6.6.3 Energy harvester performance with different linear medium block dimensions

Figures 6.15 and 6.16 show the result relative to Group 3, where the smallest granular system was considered and the dimensions of the linear medium were progressively reduced. Similar

to Figs. 6.10 and 6.12, Fig. 6.15 displays the time waveforms whereas Fig. 6.16 shows the corresponding Fourier transforms. The wave amplitude is inversely proportional to the block size, *i.e.* the amplitude is higher when the medium's volume is smaller. Looking at the frequency content of the waveforms, the decrease of the block thickness causes a shift of the vibration modes toward higher frequencies. Figure 6.16d shows only one dominant mode because the other modes above $40kHz$ were excited. Figure 6.17 shows the power output of the PZT as a function of the load resistor. The highest power of $281.4mW$ was generated with the smallest block when the resistor load was equal to $8k\Omega$. The largest block produces no more than $10.5mW$. Therefore it is important to note that selecting smaller linear medium block is essential to improve the energy harvesting performance.

(a) $304.8mm \times 304.8mm \times 101.6mm$ (b) $304.8mm \times 304.8mm \times 50.8mm$

(c) $152.4mm \times 152.4mm \times 50.8mm$ (d) $76.2mm \times 76.2mm \times 50.8mm$
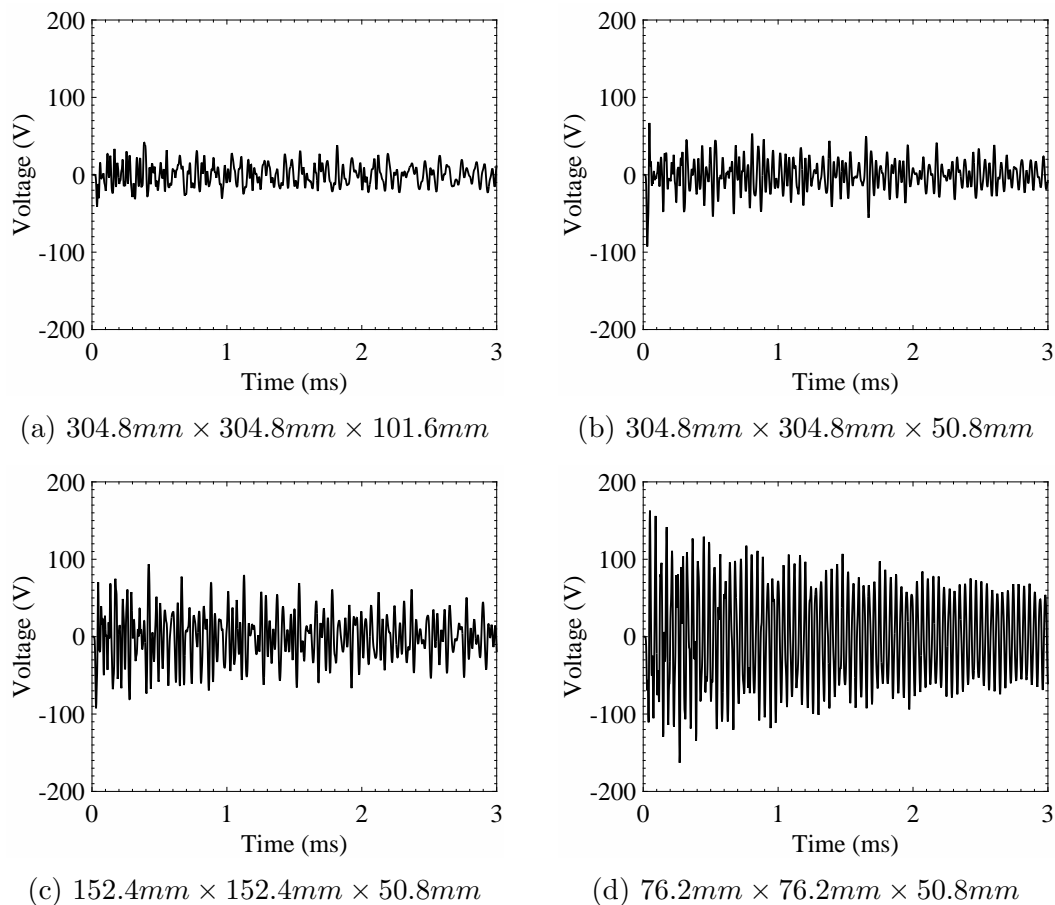
Figure 6.15: Simulation results for the same bead diameters/array diameters of $4.8mm/50.8mm$. Time waveforms obtained from the PZT with different linear medium block sizes indicated in the subcaption. Figure from Ref. [46].

(a) $304.8mm \times 304.8mm \times 101.6mm$

(b) $304.8mm \times 304.8mm \times 50.8mm$

(c) $152.4mm \times 152.4mm \times 50.8mm$

(d) $76.2mm \times 76.2mm \times 50.8mm$
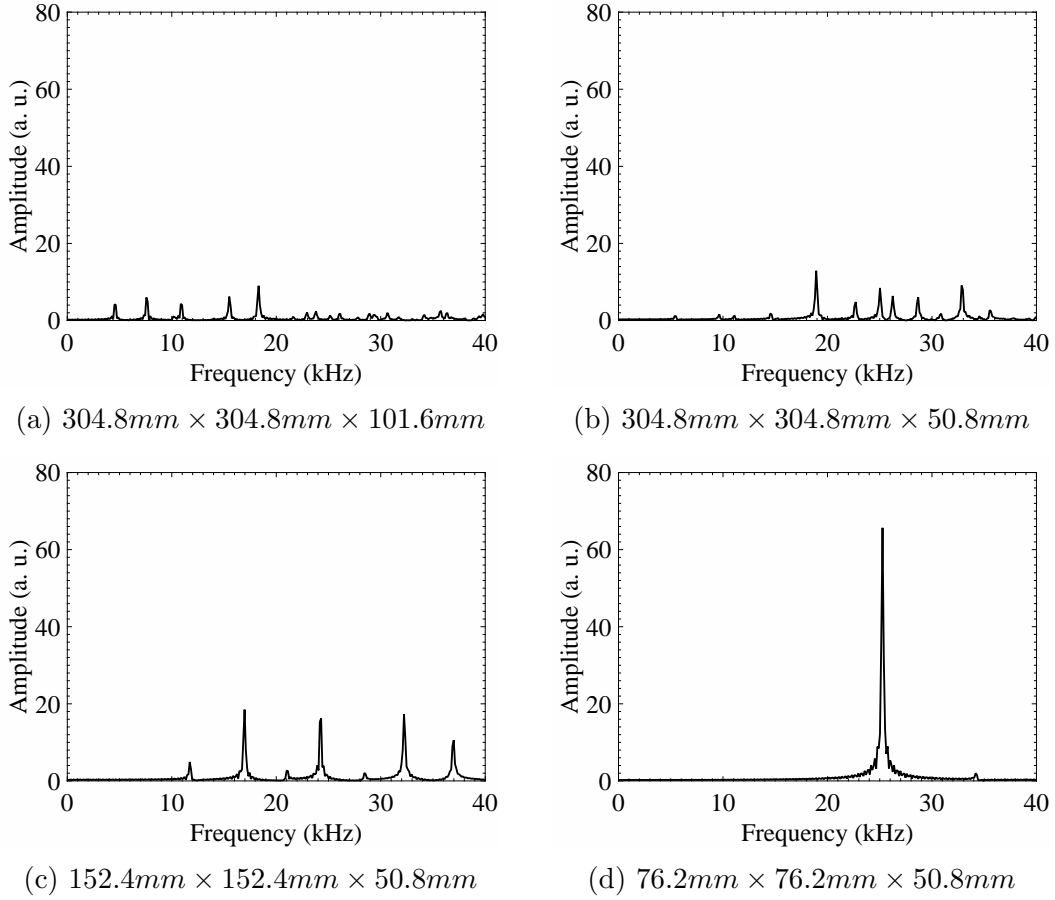
Figure 6.16: Simulation results for the same bead diameters/array diameters of $4.8mm/50.8mm$. FFTs of Fig. 6.15. Figure from Ref. [46].
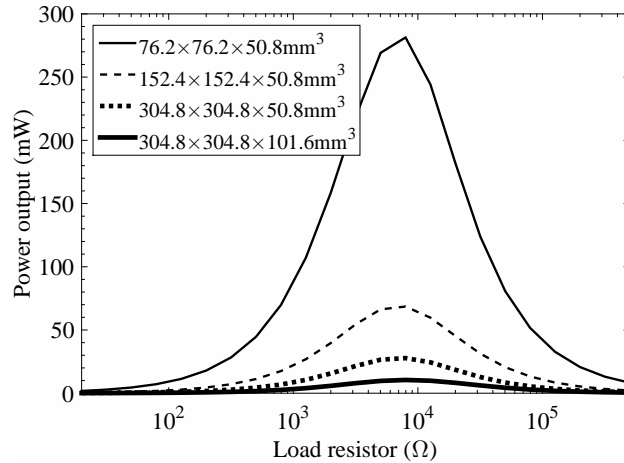
Figure 6.17: Power output as a function of load resistors for four cases with different block dimensions in Fig. 6.15. Figure from Ref. [46].
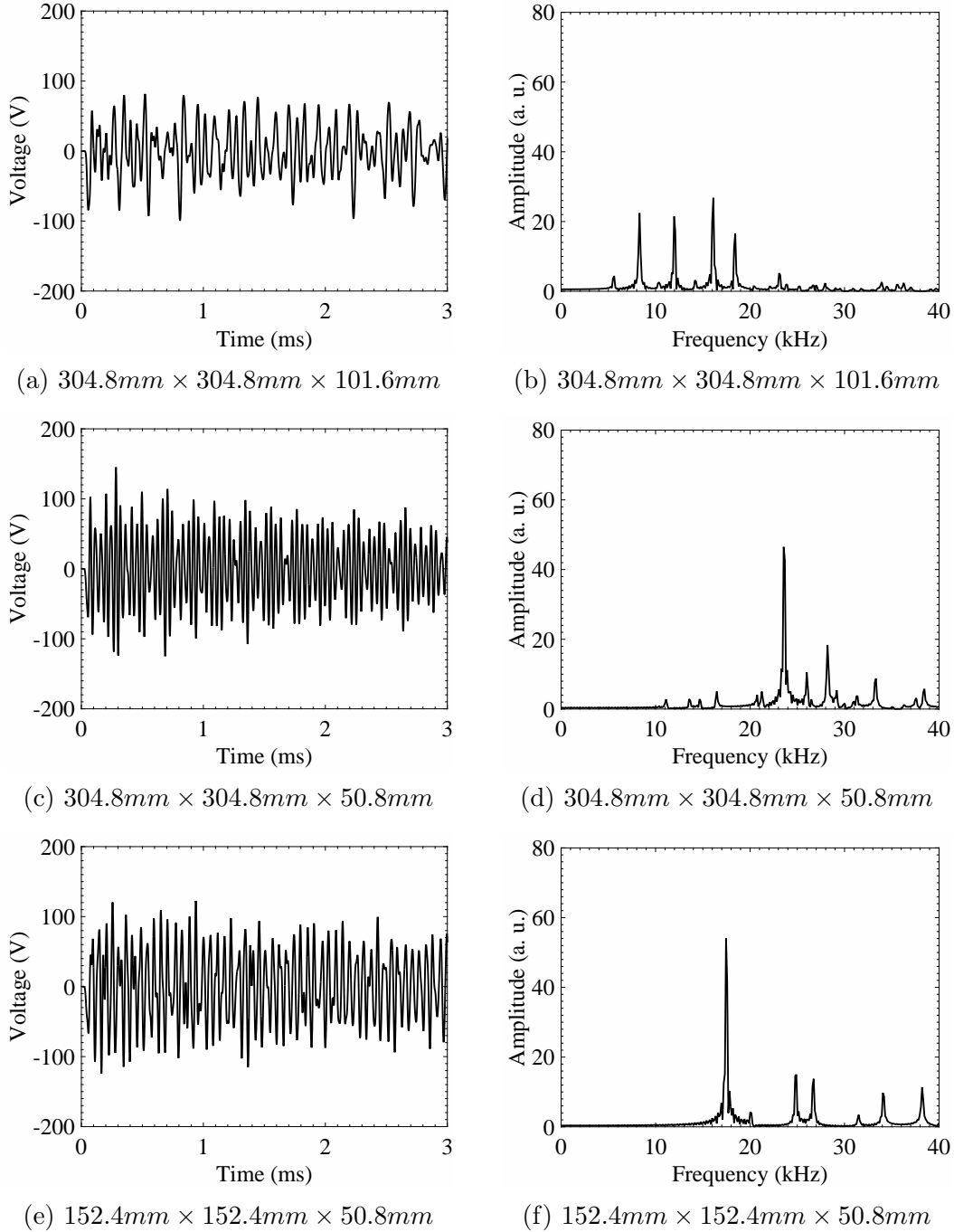
Figure 6.18: Simulation results for the same bead diameters/array diameters of $9.5mm/101.6mm$. (a), (c) and (e) Time waveforms obtained from the PZT for different linear medium block sizes. (b), (d) and (f) FFT spectra of (a), (c) and (e), respectively. Figure from Ref. [46].

Figure 6.18 shows the result from Group 4. Similar to Fig. 6.10, the panels on the left display the open circuit voltage time waveforms whereas the panels on the right display

the corresponding Fourier transforms. Unlike the time waveforms in Fig. 6.15, the voltage amplitude does not increase much as the block size decreases because the dimension of the array is large and comparable to the dimension of the block. Reducing the size of the solid from $304.8mm \times 304.8mm \times 101.6mm$ to $152.4mm \times 152.4mm \times 50.8mm$ did little change on the PZT voltage output. The analysis of the frequency spectra shows that the frequency content of the signal is strongly dependent on the geometric properties of the system. It is interesting to note that even though the natural modes for the $304.8mm \times 304.8mm \times 50.8mm$ block have lower frequency than the $152.4mm \times 152.4mm \times 50.8mm$ block, the low frequency modes are not excited in the former one. As a result, the former harvester works at higher frequency than the latter harvester. Figure 6.19 shows the power output as a function of load resistor. The highest power is equal to $187.9mW$ when an $8k\Omega$ resistor is used. It is important to note that the harvester with the smallest block does not generate the highest power as expected from the conclusion drawn in Group 3. This is due to two factors: the array dimension is comparable to the block therefore the output voltage has similar amplitudes for both cases; the force load excited higher frequency mode in the medium sized block, which results in more effective in energy harvesting according to Eq. 2.13.
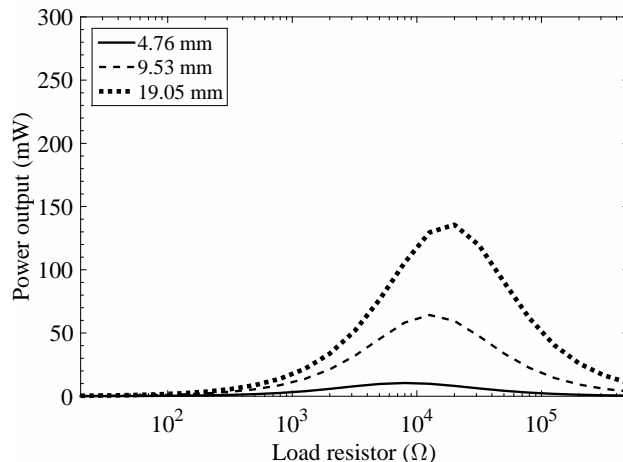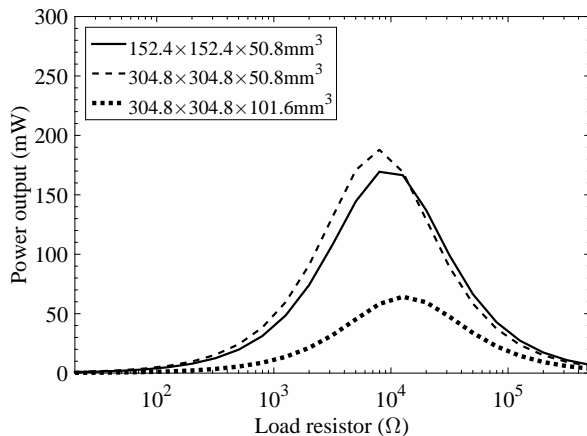

Figure 6.19: Power output as a function of load resistors for three cases with different bead diameters in Fig. 6.18. Figure from Ref. [46].

6.6.4 Energy harvester power density

In order to select the most cost-effective harvester among the nine systems, the power density was computed. As is said earlier, the power density is defined as the ratio of the electrical power to the volume of the harvester, which includes the volumes of the chains, the block and the PZT. Table 6.7 shows the results and it demonstrates that the smallest solid, *i.e.* the $76.2mm \times 76.2mm \times 50.8mm$ block, surmounted by a $50.8mm$ diameter array of 20 chains made of $4.8mm$ particles provides the highest power density equal to $918nW/mm^3$. The power density is comparable or even higher than the harvesters devised by other researchers. For example, Kim *et al.* [30] created a laser-machined piezoelectric cantilever with the power density of $301nW/mm^3$, Roundy *et al.* [69] prototyped the thin-film PZT structure with the power density of $80nW/mm^3$, duToit *et al.* designed and modeled a prototype low-level ambient MEMS harvester producing $30nW/mm^3$ [17].

Table 6.7: Test result, maximum power density (nW/mm^3). Table from Ref. [46].

Block size	Block thickness	Bead diameter (mm)/array diameter(mm)		
($mm \times mm$)	(mm)	4.8/50	9.5/101.6	19.1/203.2
304.8×304.8	101.6	1.1	6.7	13.4
	50.8	5.9	39.1	7.7
152.4×152.4	50.8	68.5	133.4	N/A
76.2×76.2	50.8	918.0	N/A	N/A

6.7 DISCUSSION AND CONCLUSIONS

Table 6.8 compares the power density obtained numerically for the best harvester configuration from the parametric study with typical values in the literature [9]. The result indicates that with parametric studies from both material and geometry perspectives, the improved energy harvester with acoustic lens is capable of generating power density that is three-fold of typical piezoelectric energy harvesters. It is emphasized here that Ref. [9] is from 2008

Table 6.8: Compare power density between the proposed harvester and typical values in Ref. [9].

Harvesting method	Power density (nW/mm^3)
Solar cells	15,000
Acoustic lens-based harvester	918
Piezoelectric	330
Vibration	116
Thermoelectric	40

and the values reported in Ref. [8] may not be representative of the current state-of-the-art. Moreover, the power density predicted in our study was achieved by assuming the initial striker velocity as $4m/s$, which is much higher than the experimental values considered and discussed in the next chapter.

In this chapter, we investigated some parameters of the harvester in order to enhance the electrical power that can be harnessed from an oscillating structure. An analytical model and a finite element analysis were used to predict the power output provided under varying conditions such as oscillation velocity, beads' material, solid's modulus, two transducer's boundary conditions, the particle size and the linear medium dimension. The results of this parametric study yield the following considerations/conclusions. The power output is proportional to the kinetic energy of the strikers. The use of heavy or fast oscillators however cannot be increased indefinitely in order to maintain the integrity of the harvester and to avoid the generation of trains of solitary waves that may hamper the ability to attain focus at the position of the transducer. At a given striker speed a heavier metamaterial delivers higher acoustic energy at the interface with the solid. In the solid, the amplitude and the frequency content of the acoustic energy arriving at the transducer are dependent on the mechanical characteristics of the solid itself. Metals are better than plastics because the mechanical loss factor is lower and therefore the acoustic attenuation is milder. Thus, although plastic materials are lighter than metals, they are not an ideal solution for our harvester. We also found that fixing the transducer's bottom surface increases the harvested energy by about two orders of magnitude as a result of larger through-thickness PZT deformation. The circuit

connected to the PZT is optimal when the value of the resistor matches the impedance of the transducer. The power output would be maximized when the frequency of the stress waves approaches or matches the resonant frequency of the transducer. For the transducer considered in this study the first natural frequency of vibration is about $170kHz$. From a geometric perspective, the metamaterials made of large particles conveyed more kinetic energy to the solid and thus to the PZT. However beam spreading effects and volume of the overall system warrant to avoid the use of large arrays and bulkier particles. In fact, it was observed that when the diameter of the array is much higher than the thickness of the solid, beam spreading and longer wave travel paths attenuate the amount of acoustic energy delivered to the piezoelectric element. The reduction of the block dimension effectively enhances the energy harvesting performance of the harvester because the bulk waves are confined. The results presented in this study demonstrate that the improved harvester is capable of generating a power output that is several orders of magnitude superior to what found experimentally in [42, 43].

7.0   PARAMETRIC STUDY: EXPERIMENT AND NUMERICAL MODELLING

7.1   INTRODUCTION

In the previous chapters, we progressively improved the performance of the harvester in order to extract more energy. The improvement was achieved by tuning the mechanical and geometric properties of the granular material and of the solid, as well as the boundary conditions of the piezoelectric element. The studies were both experimental and numerical. In the numerical investigations, a DPM was used to predict the propagation of the solitary wave along the metamaterial, and an FEA was implemented to portray the linear wave propagation in the solid and to quantify the output. The results demonstrated that the improved harvester is capable of generating a power output several orders of magnitude higher than what was found experimentally in the initial studies in Chapter 4 and Chapter 5.

In this chapter, the latest advancements are presented. In particular, we began by replicating one of the latest experiments of Chapter 4 [42] to test the repeatability the harvesting system, and then we considered the effect of one harvester components at the time. The objective of this study was two-fold: increase the energy density and verify the numerical predictions found in Ref. [47]. To achieve these objectives, we added a proof mass to the bottom of the piezoelectric element, we reduced the circle array size, and we considered two materials for the solid.

This chapter is organized as follows: Section 7.2 describes the experimental setup and the protocol for the tests. Section 7.3 describes the DPM and the FEA used to predict the experimental findings. Section 7.4 describes the results of this study whereas Section 7.5

80

ends the paper with some conclusive remarks. It is acknowledged that the study reported in this chapter is submitted to the *Journal of Intelligent Material Systems and Structures* [45].

7.2 EXPERIMENTAL SETUP

The harvester setup to be improved via a parametric study was identical to the one presented in Fig. 4.1. The experiments were conducted following the same protocol as described in Section 4.2. In order to evaluate the effect of each component, we changed one feature at a time and we conducted five experiments. As such we considered five designs and the configurations are listed in Table 7.1.

The first design was identical to the one tested in Ref. [42] and presented in Chapter 4 where the striker consisted of 20 beads, identical to the particles in the chain, glued to a $1.27mm$ thick aluminum plate (Fig. 7.1a). The total mass of the striker was $114gr$. The metamaterial consisted of twenty chains made of twenty $9.53mm$ diameter steel beads. The chains were arranged to form a circle of $101.6m$m in diameter, hereinafter called the larger array. The array was hosted by an ultra-high-molecular-weight polyethylene (UHMW) block (Fig. 7.1e) bonded to a polycarbonate block ($152.4mm \times 152.4mm \times 50.8mm$) which represents the linear medium of the system (Fig. 7.1g). The polycarbonate was chosen because wave's speed and wavelength are small, leading to better wave focusing [74]. Finally, one of the PZT surfaces was free (Fig. 7.1c).

Table 7.1: Configurations of the different cases studied experimentally. Table from Ref. [45].

Design	Striker type	PZT boundary	Array size	Linear medium
1	bead	free	large	polycarbonate
2	plate	free	large	polycarbonate
3	plate	fixed	large	polycarbonate
4	plate	fixed	small	polycarbonate
5	plate	fixed	small	steel

(a) bead striker

(b) plate striker
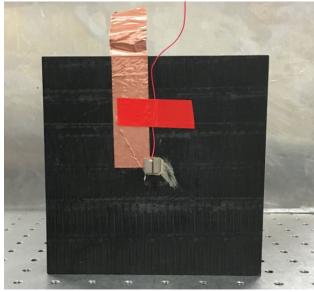
(c) free PZT
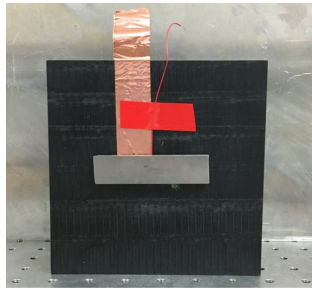
(d) fixed PZT
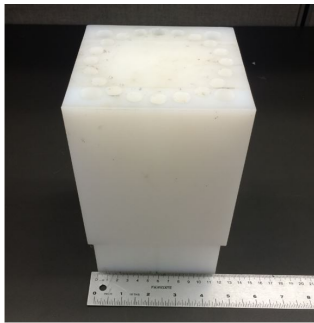
(e) large array
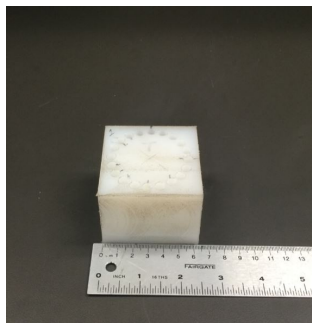
(f) small array
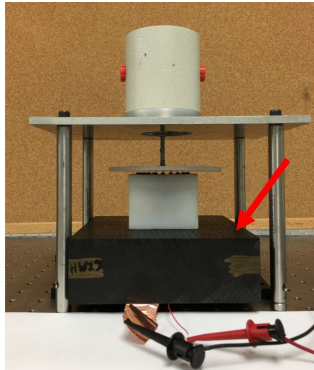
(g) polycarbonate block
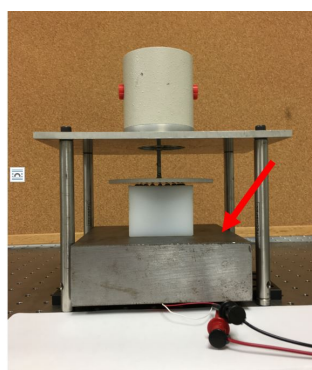
(h) steel block

Figure 7.1: Photos of some of the components forming the harvester. Figure from Ref. [45].

In the second design, the plate and the particles were replaced with a thicker aluminum plate, namely $4mm$ thick. The purpose was two-fold: evaluate the effect of the striker design on the performance of the harvester and simplify the design. The weight of the thick plate was $117.5gr$, purposely close to the total weight of the first striker. This was necessary in order to guarantee close value of the momentum at the impact with each chain. The photo of this new striker is presented in Fig. 7.1b.

In the third design we changed the boundary condition of the PZT: a proof mass of $48gr$. was added to the bottom of the PZT in order to mimic fixed boundary condition. This is shown in Fig. 7.1d and the objective was to validate experimentally the numerical prediction determined in Ref. [47] that the energy output can be boosted by fixing the PZT bottom boundary.

In order to increase the energy density by reducing the volume of the harvester, we assembled a smaller metamaterial, namely a $50.8mm$ diameter metamaterial, hereinafter the smaller array. A photo of the smaller UHMW block hosting the chains of $4.7mm$ diameter particles is presented in Fig. 7.1f. This design served also to validate experimentally the numerical findings in Ref. [46].

Finally the last harvester considered in this study was identical to the fourth design, but the polycarbonate block was replaced with a steel block of same volume. This was also done to increase the energy density of the harvester and prove the numerical findings determined in [47]. The assembly of this fifth design is shown in Fig. 7.1h. Each experiment was conducted following the experiment protocol presented in Section 4.2

7.3 DISCRETE PARTICLE MODEL AND FINITE ELEMENT MODEL: SETUP

The experimental setups were replicated numerically using a DPM and a FEA. The numerical configuration is identical to the one described in Section 6.3. The only difference is that for designs three, four and five. A steel strip was modeled by SOLID185 and attached to the bottom of the PZT in the FEA.

7.4 RESULTS

7.4.1 Experimental results

(a) the bead striker

(b) the plate striker, free PZT

(c) fixed PZT, large array

(d) small array, polycarbonate block

(e) steel block
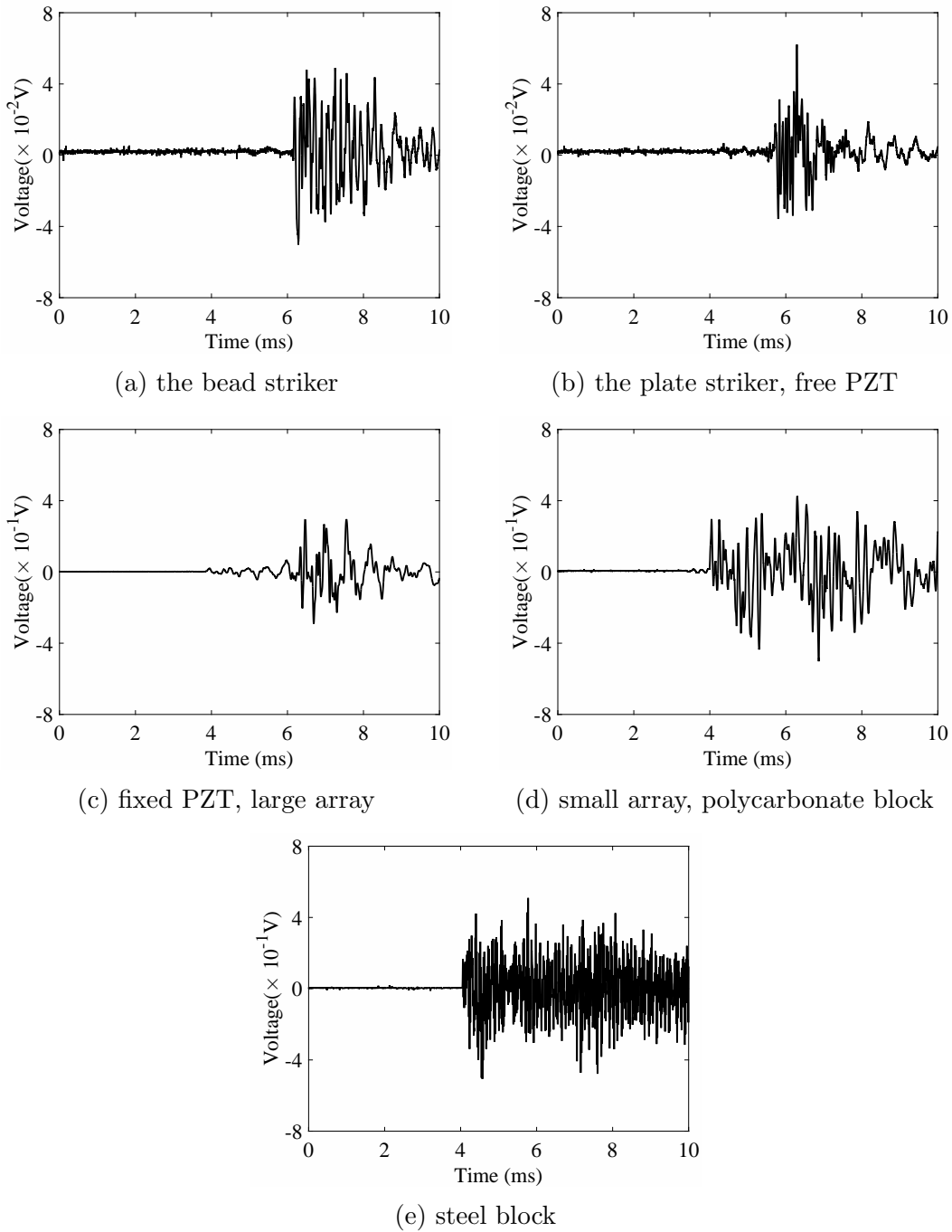
Figure 7.2: Experimental results of time waveforms for five cases. Figure from Ref. [45].

The first configuration we studied was a large array tapped by a bead striker and located above a polycarbonate medium where the PZT was free to vibrate. Figure 7.2a shows one of the 100 time waveforms recorded and stored by the NI-PXI when a $27k\Omega$ load resistor was connected. Note that the trigger was set when a positive edge of the signal fed to the shaker moved the shaker downward and $3ms$ of pre trigger signal is recorded. Figures 7.3a shows the corresponding fast Fourier transform (FFT); a dominant peak at $6kHz$ is visible. The voltage amplitude in Fig. 7.2a is of the same voltage amplitude demonstrate in Ref. [42] of the same experiment.

Similar to Fig. 7.2a, Figs. 7.2b, 7.2c, 7.2d, and 7.2e show the time waveform corresponding to the four other cases considered in this study. To ease the comparison among the five configurations, the vertical and the horizontal scales of the panels were left identical; however the amplitude scale of Figs. 7.2a and 7.2b are one order of magnitude smaller than the other three. The comparison among the five configurations suggests that the setups with the small array provide larger amplitude than other cases.

The corresponding frequency spectra of Fig. 7.2 are presented in Fig. 7.3. As for the time waveforms, the vertical scales of Figs. 7.3c, 7.3d, and 7.3e are one order of magnitude larger than the vertical scales of Fig. 7.3a and Fig. 7.3b. The spectra reveal that the smallest array with steel block contains many resonances. This is the effect of two main factors. First, the steel block is more rigid than the polycarbonate solid and therefore it has higher resonance frequencies. Second, the solitary pulse propagating along the smaller chains has a shorter duration yielding broader bandwidth. Thus, it is capable of exciting multiple high frequency components in the block. Figures 7.2e and 7.3e suggest that the time waveform and the corresponding spectrum associated with the fifth design span beyond the horizontal intervals presented in these figures.

To provide a complete portray of the output from this design, Fig. 7.4 shows the time waveform in the interval $[0 - 20ms]$ and the frequency content in $[0 - 100kHz]$ range. The presence of some resonances around $10kHz$, $45kHz$, and $52kHz$ are visible.

In order to compare the harvesting performance of the five designs, we loaded the PZT with different resistive loads and we computed the averaged power in the time window of the first $2ms$ after the time of arrival for each waveforms using the same method applied
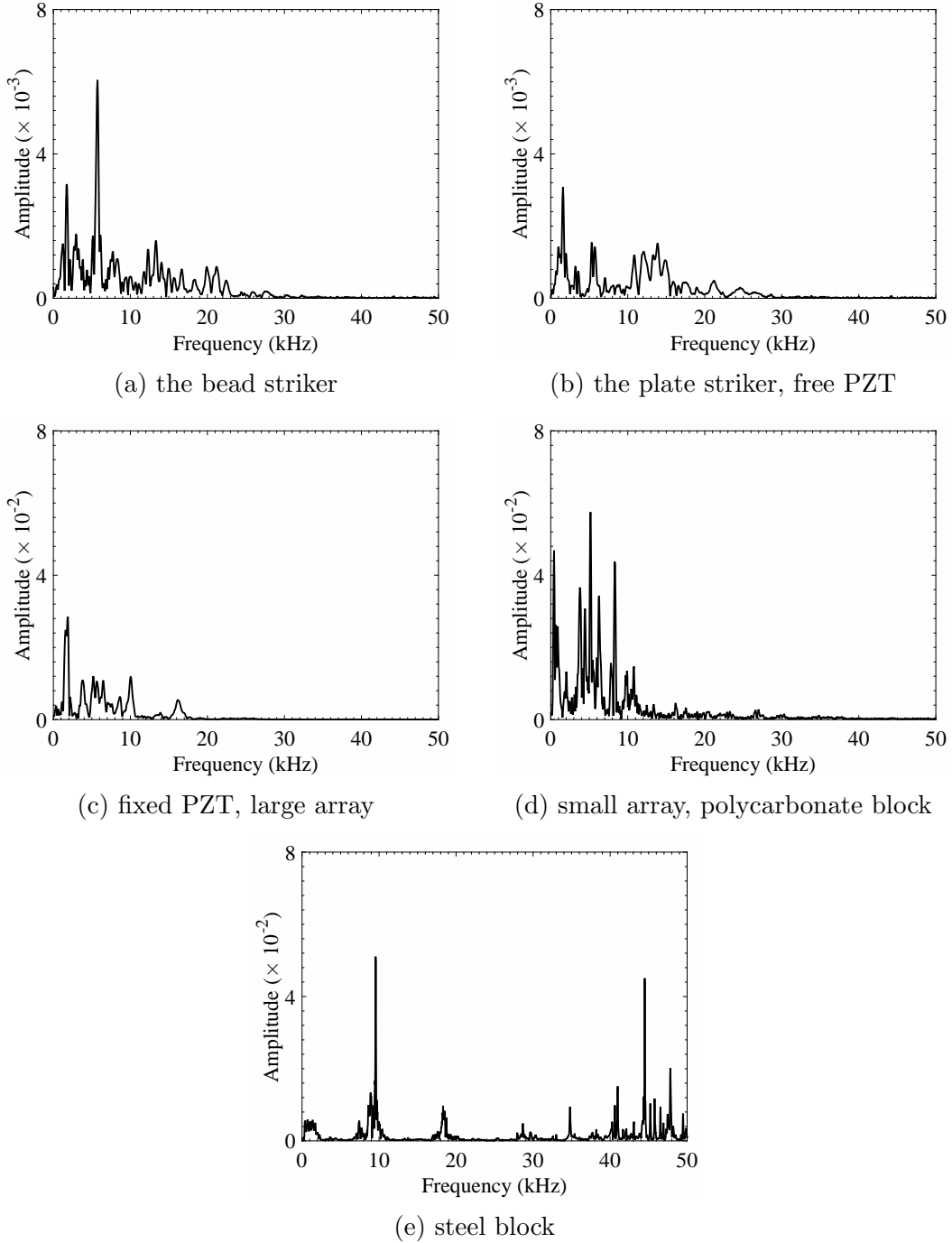
Figure 7.3: FFT spectra of the time waveforms in Fig. 7.3. Figure from Ref. [45].

in Section 4.3. The power output was then divided by the volume of the harvester in order to determine the power density. The results are presented in Fig. 7.5 where the power density is presented as a function of load resistors for all five designs. The plots demonstrate

(a) time waveform zoom out   (b) spectrum zoom out
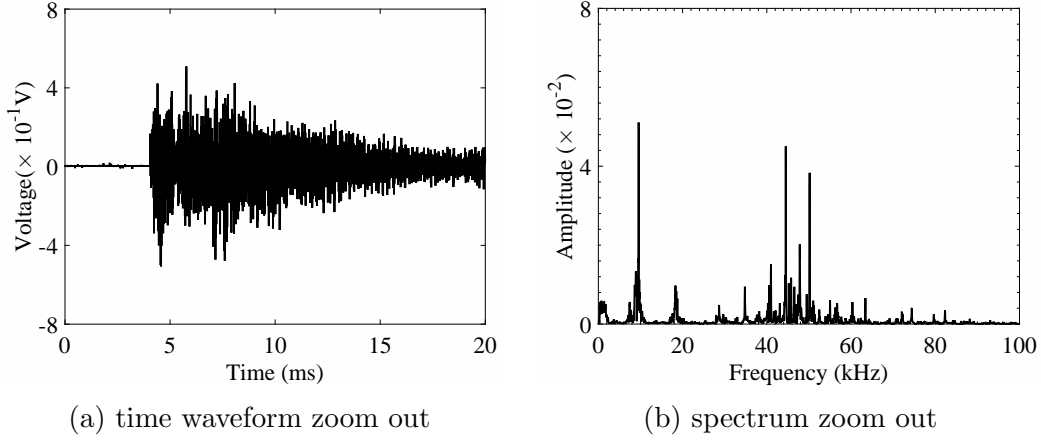
Figure 7.4: The zoom-out plots for the time waveform and the corresponding FFT spectrum for case 5. Figure from Ref. [45].

that the proper design of the harvester can boost the energy density by three orders of magnitudes. Moreover, the load resistor affect the density as well. Indeed, the peaks of different curves appear with different load resistor values. Overall the value of the optimal resistor is inversely proportional to the vibration frequency. According to Eq. 2.12, the power output is maximized when the load resistor is equal to the absolute value of the PZT impedance. Therefore optimal load resistor $R_{opt} = 1/(\omega C_{PZT})$ is inverse proportional to the vibration frequency.
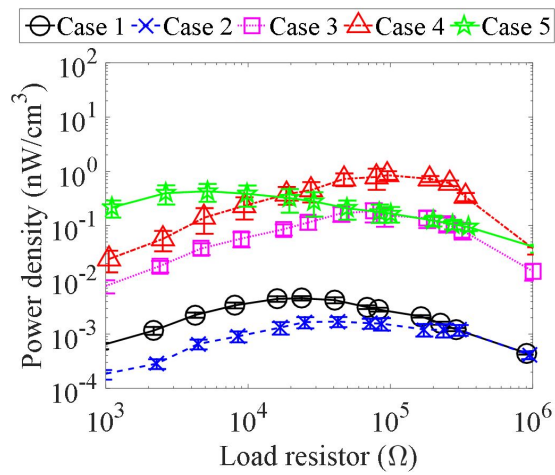
Figure 7.5: Experimental results: power density as functions of different load resistors for five different cases. Figure from Ref. [45].

7.4.2 Numerical results

As is said earlier, the five designs were modeled numerically. The results are presented in Figs. 7.6 and 7.7. Overall, we notice that the models overestimate the amplitudes of the time

(a) the bead striker

(b) the plate striker, free PZT

(c) fixed PZT, large array

(d) small array, polycarbonate block

(e) steel block
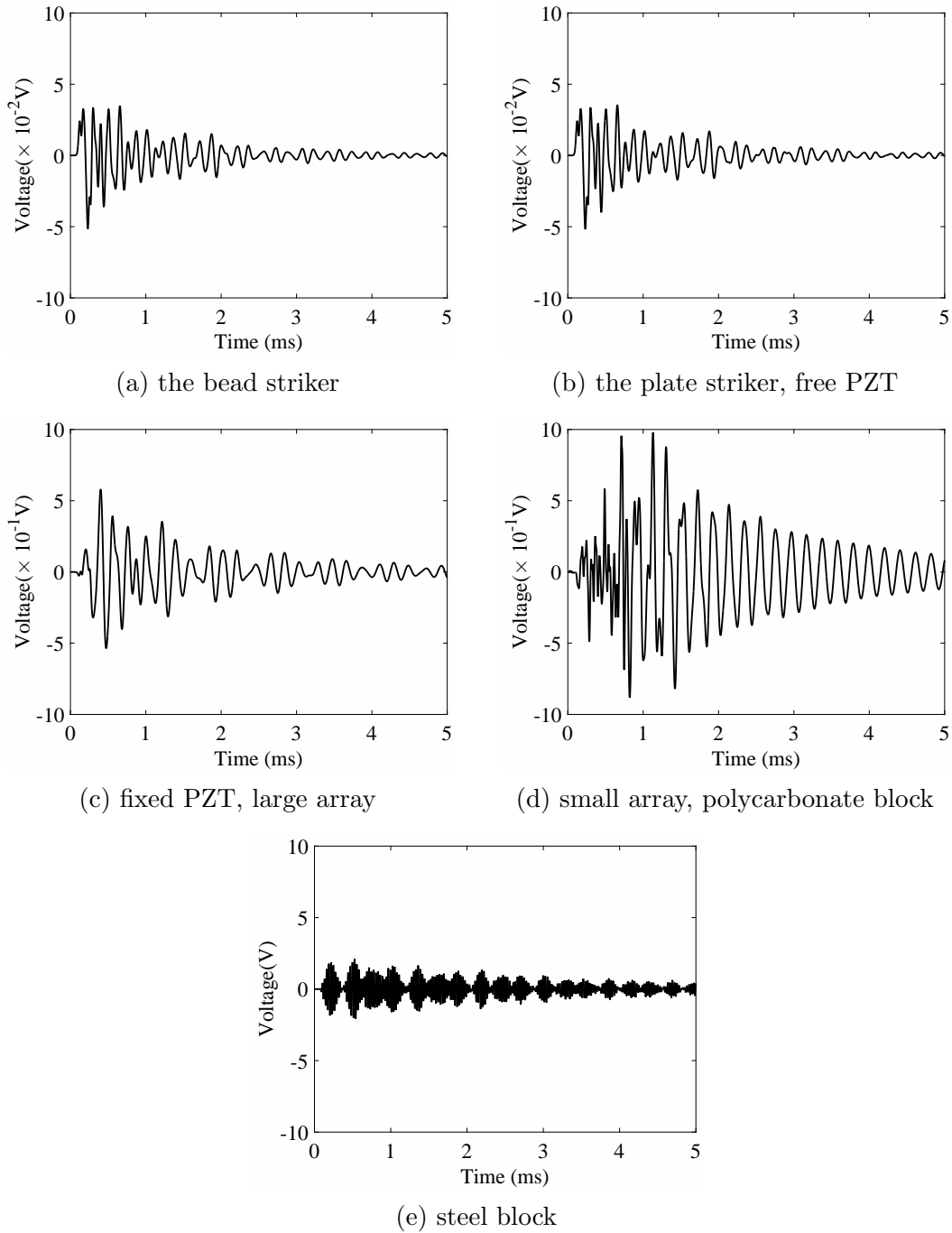
Figure 7.6: Numerical results of time waveforms for five cases. Figure from Ref. [45].

(a) the bead striker

(b) the plate striker, free PZT

(c) fixed PZT, large array

(d) small array, polycarbonate block

(e) steel block
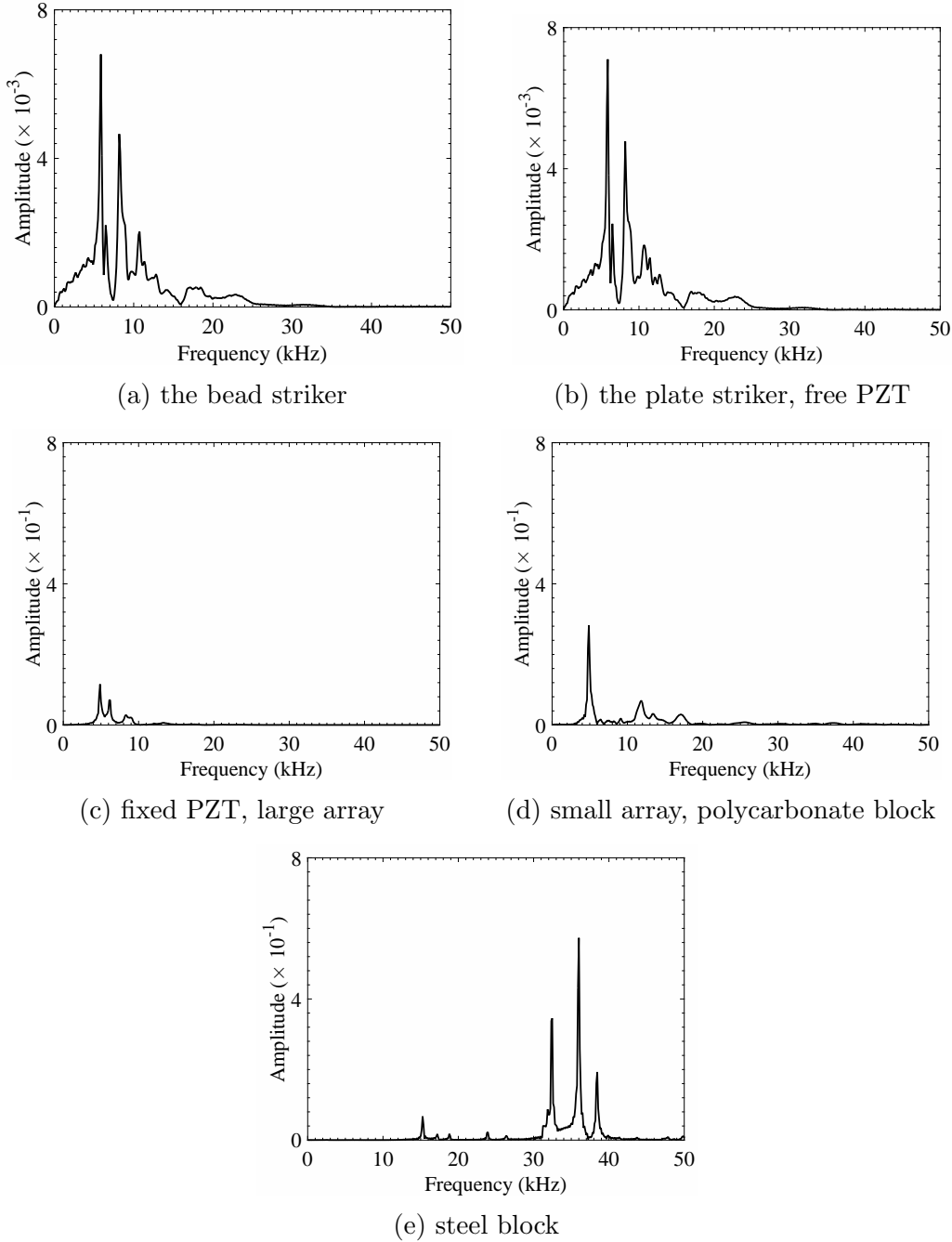
Figure 7.7: FFT spectra for the time waveforms in Fig. 7.6. Figure from Ref. [45].

waveforms while they predict accurately well the frequency contents. The overestimation is likely due to a combination of factors that include the absence of attenuation and dissipation terms in the numerical model, slight inaccuracy related to the finite element model of the PZT, and difference on the speed of the striker. It should also be noted that the syn-

chronization about the solitary wave excitation among the twenty chains is experimentally changing. In fact, while in the numerical model the solitary pulses refract into the linear medium simultaneously, in the experiments the simultaneous excitation of the solitary pulses using a mechanical striker cannot be guaranteed because of tolerances in the manufacturing of the spherical particles and possible misalignments in the chain assembly.

The correspondence between the models and the experimental results can be quantified in Fig. 7.8 where the power density predicted numerically is predicted as a function of the load resistor for the five designs. To ease the comparison, the vertical scale of Fig. 7.8 is identical to the vertical scale of Fig. 7.5. We see that the numerical power density is about one order of magnitude larger than the experimental density but the overall trend and the load resistor at which the density is the largest match very well.
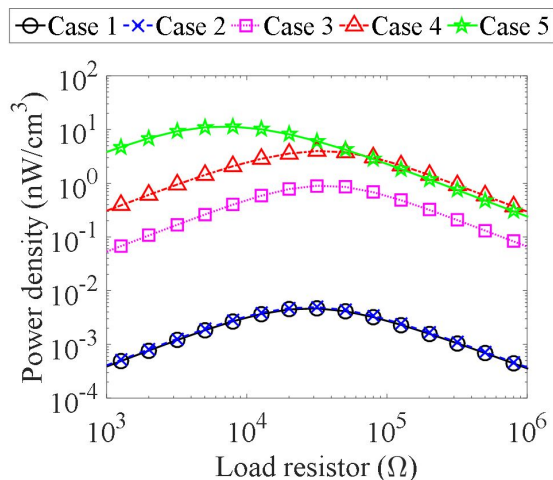
Figure 7.8: Numerical results: power density as functions of different load resistors for five different cases. Figure from Ref. [45].

7.5 DISCUSSION AND CONCLUSIONS

Table 7.2 compares the power density in the best harvester configuration from the experimental parametric study with typical values in the literature [9] and the numerical parametric study in Table 6.8 of Chapter 6. The result indicates that the power density achieved experimentally is significantly lower than the values obtained from the numerical prediction.

Table 7.2: Compare power density between the experiment result and Table 6.8.

Harvesting method	Power density (nW/mm^3)
Solar cells	15,000
Acoustic lens-based harvester (numerical)	918
Piezoelectric	330
Vibration	116
Thermoelectric	40
Acoustic lens-based harvester (experimental)	0.001

The reason is multi-fold. First, the striker velocity in the experiments was estimated to be $0.15 m/s$ which is much slower than the striker velocity of $4 m/s$ in the numerical study. Second, the boundary of the PZT in the experiment was improved by attaching a $48 gr.$ mass but still not reproducing fixed boundary conditions. Third, attenuation of the waves in the chain was not included in the DPM.

In this chapter we improved the design of an energy harvesting system based on mechanical vibrations and on the propagation of nonlinear solitary waves propagating along a metamaterial. The metamaterial consists of an array of one-dimensional chains of spherical particles assembled along a circumference. We investigated the effects of the harvester parameters, namely the geometry of the striker, the size of the metamaterial, the boundary condition of the piezoelectric element, and the material of the linear solid, on the amount of energy density that can be harvested. In order to evaluate the effect of each parameter, five different designs were considered, by changing one parameter at the time. The experimental results were compared with a numerical model based on a discrete particle model and finite element analysis. Both the numerical and the experimental results proved that the performance of the harvester can be greatly enhanced, by several orders of magnitude, by choosing the proper combination of the components forming the harvester.

Future studies shall evaluate experimentally larger speeds of the striker, design the circuit to store the energy in order to power electronics when needed, and consider the most effective solution to embed the proposed harvester in a real structure whose vibration can be exploited.

8.0 CONCLUSIONS AND RECOMMENDATIONS FOR FUTURE WORK

8.1 CONCLUSIONS

In this dissertation we devised an HNSW-based acoustic lens and deployed the acoustic lens in mechanical energy harvesting. In particular, the acoustic lens is composed of a circle array of identical chains of spherical particles and a linear medium. HNSWs are excited in all the chains simultaneously and transform into bulk waves in the linear medium. The bulk waves reach the bottom center of the linear medium and achieve constructive interference. In Chapter 3, We compared the performance of the proposed acoustic lens with another acoustic lens with the line array configuration. Numerical simulation and experimental results show a boost of maximum pressure by utilizing the circle array.

In Chapter 4, we further utilized the acoustic lens in mechanical energy harvesting applications. Specifically, we attached a piezoelectric element to the bottom center of the linear medium where the acoustic energy is focused. And we mimic the structure vibration by tapping the chains in a certain pattern with a shaker. The energy harvesting performance of the energy harvester with four, ten, and twenty chains is compared experimentally. The results suggest that the harvester with more chains have a higher power output given identical mechanical input, *i.e.* the same tapping pattern. Furthermore, we compared the energy harvesting performance of the HNSW-based harvester with a traditional cantilever beam harvester. Experimental results indicate that the HNSW-based harvester is capable of generating the same amount of power output as the traditional cantilever beam harvester. Moreover, we studied in Chapter 5 the functionality of the array of chains by substituting the chains with steel rods. The experimental results show that the harvester with the chains, which supports the propagation of the HNSWs, is capable of generating higher power output.

In order to improve the performance of the proposed energy harvester, an analytical analysis was done to qualitatively predict a boost of power output by fixing the bottom surface of the piezoelectric element. In Chapter 6, we further improved the HNSW-based energy harvesters with parametric studies from both material and geometry perspectives. The parametric studies for harvester improvement were done via numerical simulation by modelling the energy harvester with a DPM and FEA. From a material point of view, heavy materials for the chains and rigid materials for the linear medium can generate high power output. This is due to the fact that heavier strikers carry more kinetic energy and more rigid linear medium has a higher vibration frequency. From a geometry point of view, harvesters with a smaller dimension generates higher power output since the vibration energy is more concentrated in a more confined space.

In Chapter 7, some experiments were done to validate the findings in the harvester parametric studies with numerical simulation. Experimental results confirmed the predictions of higher power output from the configurations with fixed piezoelectric element, smaller harvester dimension, and metal linear medium block.

8.2 RECOMMENDATIONS FOR FUTURE WORK

Though the proposed energy harvester has been improved and the power output is boosted three orders of magnitude comparing to the original design, there are still many key features to be improved. The first and most difficult point is to guarantee the time synchronization of striking time, such that all the HNSWs are excited simultaneously. This improvement can largely enhance the power output and the repeatability of the energy harvester.

Another key feature to be improved is the beam spreading. Current chains are aligned perpendicular to the top surface of the linear medium. This results in the fact that major portion of the acoustic energy is traveling downward instead of towards the focal point due to the beam spreading effect. To avoid this problem, the chains can be aligned with certain inclinations such that the chains are pointing to the focal point at the interface between the chain and the linear medium.

Finally, current voltage level is too low that it cannot be rectified with diodes. Therefore, no harvesting circuits can be deployed to collect the energy to power electronics. A major future work includes increasing the output voltage level and design the most effective interface circuit for energy collection and storage.

APPENDIX A

ABSTRACTS OF OTHER JOURNAL PUBLICATIONS AT THE UNIVERSITY OF PITTSBURGH

This appendix lists some of other works accomplished during my PhD study at the University of Pittsburgh. The topics of these studies span from the structural health monitoring using guided waves to the nondestructive evaluation of structures using HNSWs. For each study, the abstract of the published refereed paper [4, 66, 44, 16] is provided for convenience. The full reference is provided at the end of the abstract.

A.1 REFERENCE-FREE DAMAGE DETECTION BY MEANS OF WAVELET TRANSFORM AND EMPIRICAL MODE DECOMPOSITION APPLIED TO LAMB WAVES

Guided ultrasonic waves are increasingly used in all those structural health monitoring applications that benefit from built-in transduction, moderately large inspection ranges, and high sensitivity to small flaws. This article describes a monitoring system based on the generation and detection of the guided ultrasonic waves from an array of sparse transducers. In a round-robin manner, ultrasonic waves are generated and measured from all possible different pairs of excitation and sensing transducers. The ultrasonic signals are then processed using continuous wavelet transform and empirical mode decomposition to extract few damage-sensitive features that enable the detection and localization of damage. With respect to most of the

95

existing guided ultrasonic wavebased methods, the proposed approach does not require to record data from a pristine structure (baseline data), and damage is inferred by examining the selected features obtained from all the possible combinations of actuatorsensor pairs of the array. In this study, the method is validated using commercial finite element software to model the presence of 10 ultrasonic transducers bonded onto an aluminum plate. The results are promising and ongoing studies are focusing on the experimental validation and the application to other waveguides.

A. Bagheri, **K. Li**, and P. Rizzo. Reference-free damage detection by means of wavelet transform and empirical mode decomposition applied to lamb waves. *Journal of Intelligent Material Systems and Structures*, 24(2):194-208, 2013.

A.2   NONCONTACT MONITORING OF IMMERSED PLATES BY MEANS OF LASER-INDUCED ULTRASOUNDS

This article presents the results of an experimental and numerical study where guided ultrasonic waves were used for the structural health monitoring/nondestructive evaluation of an immersed aluminum plate. Leaky Lamb waves were generated by means of a pulsed laser and detected by an array of immersion transducers. The signals were then processed using continuous wavelet transform to extract few damage-sensitive features that were fed to an unsupervised learning algorithm based on outlier analysis. The experimental setup was simulated numerically using a commercial finite element software to predict the time of arrival of the propagating modes. In order to assess the capability of the monitoring system to detect damage, four defects were devised on the plate prior to the immersion in water. We found that the noncontact probing system and the signal processing enable the detection of cracks and holes.

E. Pistone, **K. Li**, and P. Rizzo. Noncontact monitoring of immersed plates by means of laser-induced ultrasounds. *Structural Health Monitoring*, 12(5-6):549-565, 2013.

A.3 NONRECIPROCAL PROPAGATION OF SOLITARY WAVES IN GRANULAR CHAINS WITH ASYMMETRIC POTENTIAL BARRIERS

In the study presented in this paper, nonreciprocal propagation of highly nonlinear solitary waves (HNSWs) along one-dimensional chains of spherical particles is attained by inserting asymmetric potential barriers inside the chains. The barriers partially reflect the waves propagating along one direction whereas pass the waves along the opposite direction. This nonreciprocal effect is investigated numerically for different number of barriers, and for various barriers' stiffness. The results indicate that more and stiffer barriers provide better unidirectional transmission than soft barriers. In the future, the unidirectional transmission effect observed in this study could be applied for acoustic switching or acoustic rectification.

K. Li and P. Rizzo. Nonreciprocal propagation of solitary waves in granular chains with asymmetric potential barriers. *Journal of Sound and Vibration*, 365:15-21,2016.

A.4 ON THE RELIABILITY OF A SOLITARY WAVE BASED TRANSDUCER TO DETERMINE THE CHARACTERISTICS OF SOME MATERIALS

In the study presented in this article we investigated the feasibility and the reliability of a transducer design for the nondestructive evaluation (NDE) of the stiffness of structural materials. The NDE method is based on the propagation of highly nonlinear solitary waves (HNSWs) along a one-dimensional chain of spherical particles that is in contact with the material to be assessed. The chain is part of a built-in system designed and assembled to excite and detect HNSWs, and to exploit the dynamic interaction between the particles and the material to be inspected. This interaction influences the time-of-flight and the amplitude of the solitary pulses reflected at the transducer/material interface. The results of this study show that certain features of the waves are dependent on the modulus of elasticity of the

material and that the built-in system is reliable. In the future the proposed NDE method may provide a cost-effective tool for the rapid assessment of materials' modulus.

W. Deng, A. Nasrollahi, P. Rizzo, and **K. Li**. On the reliability of a solitary wave based transducer to determine the characteristics of some materials. *Sensors*, 16(1):5, 2015.

APPENDIX B

LIST OF PUBLICATIONS

B.1   REFEREED JOURNAL PUBLICATIONS

1. **K. Li**, P. Rizzo, and X. Ni. Alternative designs of acoustic lenses based on nonlinear solitary waves. *ASME Journal of Applied Mechanics*, 81(7):071011, 2014.

2. **K. Li** and P. Rizzo. Energy harvesting using an array of granules. *ASME Journal of Vibration and Acoustics*, 137(4):041002, 2015.

3. **K. Li** and P. Rizzo. Energy harvesting using arrays of granular chains and solid rods. *Journal of Applied Physics*, 117(21):215101, 2015.

4. **K. Li**, P. Rizzo, and A. Bagheri. A parametric study on the optimization of a metamaterial-based energy harvester. *Smart Materials and Structures*, 24(11):115019, 2015.

5. **K. Li** and P. Rizzo. Nonreciprocal propagation of solitary waves in granular chains with asymmetric potential barriers. *Journal of Sound and Vibration*, 365:15-21,2016.

6. A. Bagheri, **K. Li**, and P. Rizzo. Reference-free damage detection by means of wavelet transform and empirical mode decomposition applied to lamb waves. *Journal of Intelligent Material Systems and Structures*, 24(2):194-208, 2013.

7. E. Pistone, **K. Li**, and P. Rizzo. Noncontact monitoring of immersed plates by means of laser-induced ultrasounds. *Structural Health Monitoring*, 12(5-6):549-565, 2013.

8. W. Deng, A. Nasrollahi, P. Rizzo, and **K. Li**. On the reliability of a solitary wave based transducer to determine the characteristics of some materials. *Sensors*, 16(1):5, 2015.

9. **K. Li** and P. Rizzo. Experimental optimization of an energy harvester based on highly nonlinear solitary waves. *Journal of Intelligent Material Systems and Structures*, Submitted.

10. **K. Li** and P. Rizzo. Geometric optimization of harvesters based on highly nonlinear solitary waves. *ASME Journal of Vibration and Acoustics*, Submitted.

B.2   CONFERENCE PROCEEDINGS

1. E. Pistone, A. Bagheri, **K. Li**, and P. Rizzo. Signal processing for the inspection of immersed structures. *SPIE Smart Structures and Materials+ Nondestructive Evaluation and Health Monitoring*, 86951A, 2013.

2. E. Pistone, A. Bagheri, **K. Li**, and P. Rizzo. Advancement on the inspection of immersed plates by means of guided waves. *Proceedings of 9th International Workshop on Structural Health Monitoring*, Stanford, CA, 2013.

3. L. Cai, P. Rizzo, **K. Li**, and L. Al-Nazer. Coupling mechanism of granular medium and slender beams. *SPIE Smart Structures and Materials+ Nondestructive Evaluation and Health Monitoring*, 90631Z, 2014.

4. P. Rizzo, A. Bagheri, and **K. Li**. Guided ultrasonic waves for the nondestructive evaluation imaging of pipes. *Shale Energy Engineering*, 2014.

5. **K. Li** and P. Rizzo. On the use of nonlinear solitary waves for energy harvesting. *SPIE Smart Structures and Materials+ Nondestructive Evaluation and Health Monitoring*, 943103, 2015.

BIBLIOGRAPHY

[1] A. Abdelkefi, Z. Yan, and M. R. Hajj. Modeling and nonlinear analysis of piezo-electric energy harvesting from transverse galloping. *Smart materials and Structures*, 22(2):025016, 2013.

[2] W. Al-Ashtari, M. Hunstig, T. Hemsel, and W. Sextro. Enhanced energy harvesting using multiple piezoelectric elements: theory and experiments. *Sensors and Actuators A: Physical*, 200:138–146, 2013.

[3] A. Arrieta, P. Hagedorn, A. Erturk, and D. Inman. A piezoelectric bistable plate for nonlinear broadband energy harvesting. *Applied Physics Letters*, 97(10):104102, 2010.

[4] A. Bagheri, K. Li, and P. Rizzo. Reference-free damage detection by means of wavelet transform and empirical mode decomposition applied to lamb waves. *Journal of Intelligent Material Systems and Structures*, 24(2):194–208, 2013.

[5] S. P. Beeby, M. J. Tudor, and N. White. Energy harvesting vibration sources for microsystems applications. *Measurement science and technology*, 17(12):R175, 2006.

[6] L. Cai, P. Rizzo, and L. Al-Nazer. On the coupling mechanism between nonlinear solitary waves and slender beams. *International Journal of Solids and Structures*, 50(25):4173–4183, 2013.

[7] D. Castagnetti. Fractal-inspired multifrequency structures for piezoelectric harvesting of ambient kinetic energy. *Journal of Mechanical Design*, 133(11):111005, 2011.

[8] Y. Cha, H. Kim, and M. Porfiri. Energy harvesting from underwater base excitation of a piezoelectric composite beam. *Smart materials and Structures*, 22(11):115026, 2013.

[9] S. Chalasani and J. M. Conrad. A survey of energy harvesting sources for embedded systems. In *Southeastcon, 2008. IEEE*, pages 442–447. IEEE, 2008.

[10] C.-Y. Chong and S. P. Kumar. Sensor networks: evolution, opportunities, and challenges. *Proceedings of the IEEE*, 91(8):1247–1256, 2003.

[11] S. Couch and I. Bryden. Tidal current energy extraction: Hydrodynamic resource characteristics. *Proceedings of the Institution of Mechanical Engineers, Part M: Journal of Engineering for the Maritime Environment*, 220(4):185–194, 2006.

[12] A. Cuadras, M. Gasulla, and V. Ferrari. Thermal energy harvesting through pyroelectricity. *Sensors and Actuators A: Physical*, 158(1):132–139, 2010.

[13] C. Dagdeviren, B. D. Yang, Y. Su, P. L. Tran, P. Joe, E. Anderson, J. Xia, V. Doraiswamy, B. Dehdashti, X. Feng, et al. Conformal piezoelectric energy harvesting and storage from motions of the heart, lung, and diaphragm. *Proceedings of the National Academy of Sciences*, 111(5):1927–1932, 2014.

[14] C. Daraio and V. Nesterenko. Strongly nonlinear wave dynamics in a chain of polymer coated beads. *Physical Review E*, 73(2):026612, 2006.

[15] C. Daraio, V. Nesterenko, E. Herbold, and S. Jin. Tunability of solitary wave properties in one-dimensional strongly nonlinear phononic crystals. *Physical Review E*, 73(2):026610, 2006.

[16] W. Deng, A. Nasrollahi, P. Rizzo, and K. Li. On the reliability of a solitary wave based transducer to determine the characteristics of some materials. *Sensors*, 16(1):5, 2015.

[17] N. E. Dutoit, B. L. Wardle, and S.-G. Kim. Design considerations for mems-scale piezoelectric mechanical vibration energy harvesters. *Integrated Ferroelectrics*, 71(1):121–160, 2005.

[18] A. Erturk and D. J. Inman. A distributed parameter electromechanical model for cantilevered piezoelectric energy harvesters. *Journal of Vibration and Acoustics*, 130(4):041002, 2008.

[19] A. Erturk and D. J. Inman. Appendix c: Modal analysis of a uniform cantilever with a tip mass. *Piezoelectric Energy Harvesting*, pages 353–366, 2011.

[20] E. Falcon, C. Laroche, S. Fauve, and C. Coste. Collision of a 1-d column of beads with a wall. *The European Physical Journal B-Condensed Matter and Complex Systems*, 5(1):111–131, 1998.

[21] M. Ferrari, V. Ferrari, M. Guizzetti, D. Marioli, and A. Taroni. Piezoelectric multi-frequency energy converter for power harvesting in autonomous microsystems. *Sensors and Actuators A: Physical*, 142(1):329–335, 2008.

[22] V. Giurgiutiu and A. N. Zagrai. Characterization of piezoelectric wafer active sensors. *Journal of Intelligent Material Systems and Structures*, 11(12):959–976, 2000.

[23] A. Hajati and S.-G. Kim. Ultra-wide bandwidth piezoelectric energy harvesting. *Applied Physics Letters*, 99(8):083105, 2011.

[24] M. A. Halim, H. Cho, and J. Y. Park. Design and experiment of a human-limb driven, frequency up-converted electromagnetic energy harvester. *Energy Conversion and Management*, 106:393–404, 2015.

[25] A. Harb. Energy harvesting: State-of-the-art. *Renewable Energy*, 36(10):2641–2654, 2011.

[26] H. Hertz. On the contact of elastic solids. *J. reine angew. Math*, 92(156-171):110, 1881.

[27] Y. Jeon, R. Sood, J.-H. Jeong, and S.-G. Kim. Mems power generator with transverse mode thin film pzt. *Sensors and Actuators A: Physical*, 122(1):16–22, 2005.

[28] S. Job, F. Melo, A. Sokolow, and S. Sen. How hertzian solitary waves interact with boundaries in a 1d granular medium. *Physical review letters*, 94(17):178002, 2005.

[29] S. Job, F. Melo, A. Sokolow, and S. Sen. Solitary wave trains in granular chains: experiments, theory and simulations. *Granular Matter*, 10(1):13–20, 2007.

[30] H. Kim, V. Bedekar, R. A. Islam, W.-H. Lee, D. Leo, and S. Priya. Laser-machined piezoelectric cantilevers for mechanical energy harvesting. *Ultrasonics, Ferroelectrics, and Frequency Control, IEEE Transactions on*, 55(9):1900–1905, 2008.

[31] H. Kim, Y. Tadesse, and S. Priya. Piezoelectric energy harvesting. In *Energy Harvesting Technologies*, pages 3–39. Springer, 2009.

[32] H. W. Kim, A. Batra, S. Priya, K. Uchino, D. Markley, R. E. Newnham, and H. F. Hofmann. Energy harvesting using a piezoelectric cymbal transducer in dynamic environment. *Japanese Journal of Applied Physics*, 43(9R):6178, 2004.

[33] S. Kim, S. Pakzad, D. Culler, J. Demmel, G. Fenves, S. Glaser, and M. Turon. Health monitoring of civil infrastructures using wireless sensor networks. In *Information Processing in Sensor Networks, 2007. IPSN 2007. 6th International Symposium on*, pages 254–263. IEEE, 2007.

[34] S.-H. Kim, J.-H. Ahn, H.-M. Chung, and H.-W. Kang. Analysis of piezoelectric effects on various loading conditions for energy harvesting in a bridge system. *Sensors and Actuators A: Physical*, 167(2):468–483, 2011.

[35] N. Kong, D. S. Ha, A. Erturk, and D. J. Inman. Resistive impedance matching circuit for piezoelectric energy harvesting. *Journal of Intelligent Material Systems and Structures*, 2010.

[36] I. A. Kunin. *Elastic media with microstructure I: one-dimensional models*, volume 26. Springer Science & Business Media, 2012.

[37] J. Kymissis, C. Kendall, J. Paradiso, and N. Gershenfeld. Parasitic power harvesting in shoes. In *Wearable Computers, 1998. Digest of Papers. Second International Symposium on*, pages 132–139. IEEE, 1998.

[38] F. Lanza di Scalea, P. Rizzo, and A. Marzani. Propagation of ultrasonic guided waves in lap-shear adhesive joints: Case of incident a0 lamb wave. *The Journal of the Acoustical Society of America*, 115(1):146–156, 2004.

[39] A. Lazaridi and V. Nesterenko. Observation of a new type of solitary waves in a one-dimensional granular medium. *Journal of Applied Mechanics and Technical Physics*, 26(3):405–408, 1985.

[40] A. J. Lee, Y. Wang, and D. J. Inman. Energy harvesting of piezoelectric stack actuator from a shock event. *Journal of Vibration and Acoustics*, 136(1):011016, 2014.

[41] J. Lee and B. Choi. Development of a piezoelectric energy harvesting system for implementing wireless sensors on the tires. *Energy Conversion and Management*, 78:32–38, 2014.

[42] K. Li and P. Rizzo. Energy harvesting using an array of granules. *ASME Journal of Vibration and Acoustics*, 137(4):041002, 2015.

[43] K. Li and P. Rizzo. Energy harvesting using arrays of granular chains and solid rods. *ASME Journal of Applied Physics*, 117(21):215101, 2015.

[44] K. Li and P. Rizzo. Nonreciprocal propagation of solitary waves in granular chains with asymmetric potential barriers. *Journal of Sound and Vibration*, 365:15–21, 2016.

[45] K. Li and P. Rizzo. Experimental optimization of an energy harvester based on highly nonlinear solitary waves. *Journal of Intelligent Material Systems and Structures*, Submitted.

[46] K. Li and P. Rizzo. Geometric optimization of harvesters based on highly nonlinear solitary waves. *ASME Journal of Vibration and Acoustics*, Submitted.

[47] K. Li, P. Rizzo, and A. Bagheri. A parametric study on the optimization of a metamaterial-based energy harvester. *Smart Materials and Structures*, 24(11):115019, 2015.

[48] K. Li, P. Rizzo, and X. Ni. Alternative designs of acoustic lenses based on nonlinear solitary waves. *Journal of Applied Mechanics*, 81(7):071011, 2014.

[49] S.-C. S. Lin, B. R. Tittmann, and T. J. Huang. Design of acoustic beam aperture modifier using gradient-index phononic crystals. *Journal of applied physics*, 111(12):123510, 2012.

[50] M. Liu and D. Gorman. Formulation of rayleigh damping and its extensions. *Computers & structures*, 57(2):277–285, 1995.

[51] H. Lv, X. Tian, M. Y. Wang, and D. Li. Vibration energy harvesting using a phononic crystal with point defect states. *Applied Physics Letters*, 102(3):034103, 2013.

[52] S. Mallat. *A wavelet tour of signal processing*. Academic press, 1999.

[53] F. S. Manciu and S. Sen. Secondary solitary wave formation in systems with generalized hertz interactions. *Physical Review E*, 66(1):016616, 2002.

[54] M. Manciu, S. Sen, and A. J. Hurd. Crossing of identical solitary waves in a chain of elastic beads. *Physical Review E*, 63(1):016614, 2000.

[55] D. Marioli, E. Sardini, and M. Serpelloni. Electromagnetic generators employing planar inductors for autonomous sensor applications. *Procedia Chemistry*, 1(1):469–472, 2009.

[56] P. D. Mitcheson. Energy harvesting for human wearable and implantable bio-sensors. In *Engineering in Medicine and Biology Society (EMBC), 2010 Annual International Conference of the IEEE*, pages 3432–3436. IEEE, 2010.

[57] V. Nesterenko. Propagation of nonlinear compression pulses in granular media. *Journal of Applied Mechanics and Technical Physics*, 24(5):733–743, 1983.

[58] V. Nesterenko. *Dynamics of heterogeneous materials*. Springer Science & Business Media, 2013.

[59] V. Nesterenko, C. Daraio, E. Herbold, and S. Jin. Anomalous wave reflection at the interface of two strongly nonlinear granular media. *Physical review letters*, 95(15):158702, 2005.

[60] X. Ni, L. Cai, and P. Rizzo. A comparative study on three different transducers for the measurement of nonlinear solitary waves. *Sensors*, 13(1):1231–1246, 2013.

[61] X. Ni and P. Rizzo. Highly nonlinear solitary waves for the inspection of adhesive joints. *Experimental mechanics*, 52(9):1493–1501, 2012.

[62] X. Ni and P. Rizzo. Use of highly nonlinear solitary waves in nondestructive testing. *Materials evaluation*, 70(5):561–569, 2012.

[63] X. Ni, P. Rizzo, and C. Daraio. Actuators for the generation of highly nonlinear solitary waves. *Review of Scientific Instruments*, 82(3):034902, 2011.

[64] X. Ni, P. Rizzo, J. Yang, D. Katri, and C. Daraio. Monitoring the hydration of cement using highly nonlinear solitary waves. *NDT & E International*, 52:76–85, 2012.

[65] M. Peigney and D. Siegert. Piezoelectric energy harvesting from traffic-induced bridge vibrations. *Smart Materials and Structures*, 22(9):095019, 2013.

[66] E. Pistone, K. Li, and P. Rizzo. Noncontact monitoring of immersed plates by means of laser-induced ultrasounds. *Structural Health Monitoring*, 12(5-6):549–565, 2013.

[67] S. R. Platt, S. Farritor, and H. Haider. On low-frequency electric power generation with pzt ceramics. *Mechatronics, IEEE/ASME Transactions on*, 10(2):240–252, 2005.

[68] S. Priya. Advances in energy harvesting using low profile piezoelectric transducers. *Journal of electroceramics*, 19(1):167–184, 2007.

[69] S. Roundy, E. S. Leland, J. Baker, E. Carleton, E. Reilly, E. Lai, B. Otis, J. M. Rabaey, P. K. Wright, and V. Sundararajan. Improving power output for vibration-based energy scavengers. *Pervasive Computing, IEEE*, 4(1):28–36, 2005.

[70] M. Sale, P. Rizzo, and A. Marzani. Semi-analytical formulation for the guided waves-based reconstruction of elastic moduli. *Mechanical Systems and Signal Processing*, 25(6):2241–2256, 2011.

[71] S. Sen, M. Manciu, and J. D. Wright. Solitonlike pulses in perturbed and driven hertzian chains and their possible applications in detecting buried impurities. *Physical Review E*, 57(2):2386, 1998.

[72] Y.-C. Shu. Performance evaluation of vibration-based piezoelectric energy scavengers. In *Energy Harvesting Technologies*, pages 79–105. Springer, 2009.

[73] W. M. Siebert. *Circuits, signals, and systems*, volume 2. MIT press, 1986.

[74] A. Spadoni and C. Daraio. Generation and control of sound bullets with a nonlinear acoustic lens. *Proceedings of the National Academy of Sciences*, 107(16):7230–7234, 2010.

[75] S. Sudevalayam and P. Kulkarni. Energy harvesting sensor nodes: Survey and implications. *Communications Surveys & Tutorials, IEEE*, 13(3):443–461, 2011.

[76] D. Sun, Y. Xu, H. Chen, K. Wu, K. Liu, and Y. Yu. A mean flow acoustic engine capable of wind energy harvesting. *Energy Conversion and Management*, 63:101–105, 2012.

[77] R. Szewczyk, E. Osterweil, J. Polastre, M. Hamilton, A. Mainwaring, and D. Estrin. Habitat monitoring with sensor networks. *Communications of the ACM*, 47(6):34–40, 2004.

[78] L.-Y. Wu, L.-W. Chen, and C.-M. Liu. Acoustic energy harvesting using resonant cavity of a sonic crystal. *Applied Physics Letters*, 95(1):013506, 2009.

[79] J. Yang, C. Silvestro, D. Khatri, L. De Nardo, and C. Daraio. Interaction of highly nonlinear solitary waves with linear elastic media. *Physical Review E*, 83(4):046606, 2011.

[80] J. Yang, C. Silvestro, S. N. Sangiorgio, S. L. Borkowski, E. Ebramzadeh, L. De Nardo, and C. Daraio. Nondestructive evaluation of orthopaedic implant stability in tha using highly nonlinear solitary waves. *Smart Materials and Structures*, 21(1):012002, 2012.

[81] Z. Zhang, H. Xiang, and Z. Shi. Modeling on piezoelectric energy harvesting from pavements under traffic loads. *Journal of Intelligent Material Systems and Structures*, page 1045389X15575081, 2015.

[82] S. Zhao and A. Erturk. Deterministic and band-limited stochastic energy harvesting from uniaxial excitation of a multilayer piezoelectric stack. *Sensors and Actuators A: Physical*, 214:58–65, 2014.

[83] L. Zuo and P.-S. Zhang. Energy harvesting, ride comfort, and road handling of regenerative vehicle suspensions. *Journal of Vibration and Acoustics*, 135(1):011002, 2013.